TUDelft

Delft University of Technology

Measuring and modelling salt and heat transport in low-land drainage canals
Flow and stratification effects of saline seepage

Hilgersom, Koen

Important note
To cite this publication, please use the final published version (if applicable).
Please check the document version above.

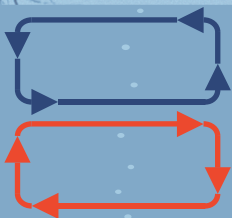# Measuring and modelling salt and heat transport in low-land drainage canals

Flow and stratification effects of saline seepage

Koen Hilgersom

Measuring and modelling salt and heat transport in low-land drainage canals

Flow and stratification effects of saline seepage

Measuring and modelling salt and heat transport in low-land drainage canals

Flow and stratification effects of saline seepage

Proefschrift

door

Koen Peter HILGERSOM

Civiel Ingenieur,
Technische Universiteit, Delft, Nederland,
geboren te Alkmaar, Nederland.

Dit proefschrift is goedgekeurd door de

promotor: prof. dr. ir. N.C. van de Giesen
copromotor: dr. ir. M. Zijlema

Samenstelling promotiecommissie:

Rector Magnificus,	voorzitter
Prof. dr. ir. N.C. van de Giesen,	Technische Universiteit Delft, promotor
Dr. ir. M. Zijlema,	Technische Universiteit Delft, copromotor

Onafhankelijke leden:

Prof. dr. ir. H.H.G. Savenije,	Technische Universiteit Delft
Prof. dr. J.S. Selker,	Oregon State University, Verenigde Staten
Dr. P.G.B. de Louw,	Deltares
Prof. dr. ir. W.S.J. Uijttewaal,	Technische Universiteit Delft
Prof. dr. M.F.P. Bierkens,	Universiteit Utrecht
Prof. dr. ir. M. Bakker,	Technische Universiteit Delft, reservelid

An electronic version of this dissertation is available at
http://repository.tudelft.nl/.

Contents

Summary

This thesis explores a new measuring approach to quantify the seepage flux from boils. Boils are preferential groundwater seeps and are a consequence of the groundwater flow that works its way through the soil matrix by creating vents of higher conductive material. In the Netherlands, boils often occur in deep polders (reclaimed lakes situated 4–7 m below sea level), transporting water directly from the deep aquifer. Because this saline aquifer is connected to the sea, the pressure difference between the sea water level and the polder water level is the main driver of the upward seepage flux. At the surface, boils seep out through canal beds and sometimes on land. This thesis focusses on boils that directly discharge into polder drainage canals. Although boils are usually highly saline compared to the fresh surface water, this research also includes an example of a relatively fresh boil.

The seeping groundwater has a fairly constant temperature throughout the year. Because the surface water temperature fluctuates over the year and over the day, temperature is an ideal tracer to measure the groundwater - surface water interaction. Previous studies applied temperature and salinity samples taken at different depths in the soil to quantify the boil seepage flux. Because the boil vents are usually not strictly vertical and can be disturbed when probing the soil, this research aims to measure the boil seepage flux from a surface water perspective. The intended measurement approach samples the surface water at a very high resolution in three dimensions, compares the temperature profiles with those in a free-surface transport model, and infers the boil flux as the bottom boundary flux of the model.

Over the past decades, fibre-optic distributed temperature sensing (DTS) has developed toward an effective means to obtain spatially distributed temperature samples. When releasing a laser signal through an optical fibre, the returning signal carries temperature information in its wavelengths. Current DTS machines allow measuring temperature down to every 25 cm along a fibre-optic cable. To obtain even higher resolutions, researchers often wrap cables to a coil. However, cable bends and the construction supporting the coil affect the measurement accuracy. Chapter 3 investigates how cable bends influence the temperature measurements in coil-wrapped DTS set-ups in order to account for this in the design of a high-resolution DTS set-up for this research. It is concluded that, with a decreasing bending radius, the cable bends increasingly affect the temperature measurements in multiple ways. The non-linearity in the bend-induced decay of the laser signal complicates compensation for these effects and requires a very careful temperature calibration approach.

To avoid continuously bent cables, the design of the three-dimensional (3-D) high-resolution DTS set-up applied a weaving pattern instead of coils (Chapter 4). This way, cables are only bent at each turnaround, intermitted by straight stretches of 1 m. By selecting the desired vertical spacing of the woven 'layers', one can

customize the vertical resolution of the set-up. To infer the seepage flux from the stream bed, the design of the set-up required very high resolutions near the bottom boundary. The set-up proved to measure very detailed temperature profiles in a water body, and even uncovered unexpected seeps in a laboratory set-up to simulate boil seepage. In the field, the measured temperatures near the stream bed displayed an accumulation of sediment around the boil during the measurement periods. Most interestingly for the current application, the detailed temperature profiles were able to capture double-diffusive phenomena.

Double-diffusion occurs when two adjacent water layers have different temperatures and salinities, and the density gradients for the temperature and salinity are opposed. For example, when cold (denser) and fresh (lighter) water overtops a warm and saline water layer, a system of convective layers develops with a very sharp temperature and salinity interface between the convective layers (i.e., double-diffusive convection). A more curious phenomenon occurs when the warm and saline layer is on top. In this case, a finger-like pattern develops at the sharp interface between the layers (i.e., salt-fingering). These systems are different from normal diffusive interfaces, which tend to fade over time. Therefore, water bodies with salt and temperature gradients demand a careful modelling of the flow processes.

To accurately model the boil-covering water body with large density gradients, a mass and momentum conservative free-surface model was selected. The model was extended with a transport module and modules accounting for temperature and salinity dependent densities, viscosities, and specific heats. Moreover, the model was extended with the option to include atmospheric heat exchange in the calculations. The performance of the model was tested on a solar pond (Chapter 5). Such ponds are double-diffusive convective water bodies with very strong density gradients, which store solar energy as heat in their bottom hypersaline layer. The model well captured the flow of warm water along the sloping edge of the solar pond and demonstrated the onset of small seiches in the pond due to the density gradients. The onset of convective layers was also captured, although their extents were not in complete agreement with measurement data. In general, the results confirmed the model capability to simulate double-diffusive convection.

Due to the boil's circular shape and the availability of 3-D temperature profiles, a 3-D modelling grid would be preferable for the boil seepage simulations. The dense grid needed for the transport simulation, however, yields too large computation times. Therefore, Chapter 6 investigated the potential of a quasi 3-D axisymmetric set-up for these simulations. To this end, the 2-DV model code was extended with few additional terms which hardly increased the computation time and kept the solution procedure mass and momentum conservative. Qualitative case studies demonstrated the model capability to simulate salt-fingers and double-diffusive convection. An analytical benchmark was set up for the axisymmetric expansion of an unconditionally stable layer from a central cold and saline seepage inflow. For the case of laminar flow conditions, the model results were in agreement with the analytical solution. Turbulent convection dispersed heat and salt significantly quicker.

The unexpected seeps in the laboratory set-up for boil seepage simulations complicated the comparison of these measurements with model output, because the exact flow paths were unknown and could not be modelled. Chapter 7 shows a comparison of the measurements with model results for the intended seepage flow. Although double-diffusive convective and unconditionally stable layers develop in both the model and the measurement results, the growth rates, and specifically the locations where the layers grow at a faster rate, are different. Moreover, the unexpected seeps seem to have a higher flow velocity, leading to a larger mixing of heat at the interface between the layers. It is concluded that the model can not be validated based on the laboratory data and additional measurements are recommended.

Although the horizontal stream flow across the boil should be negligible when applying an axisymmetric modelling approach, knowledge of the stream discharge is still relevant. For this reason, this thesis starts with exploring the possibilities to modernize and potentially automate the rising bubble technique for discharge measurement (Chapter 2). The study shows that the complicated dual camera set-up and position calculations for the air bubbles in previous publications can be avoided with modern image processing algorithms. Reflecting sun light sometimes impedes the visibility of the air bubbles on the water surface. We displayed an example of how a statistical tool still uncovers the signatures of air bubbles in digital images that would normally hardly be visible. Such tools could also be applied in pattern recognition algorithms that automatically find the air bubbles on the water surface. Although further research is necessary, the results seem to support the hypothesis that the rising bubble technique can be applied as an automatic discharge measurement technique.

We conclude that the boil seepage inversion from double-diffusive models is currently still very challenging (Chapter 8). The locations and extents of double-diffusive convection cells and salt-fingers are dependent on sub-grid processes. Moreover, these phenomena are very sensitive to local density gradients which will never be modelled 'perfectly'. The importance of model boundary conditions when the layer of seepage water is still thin could also affect the inversion of the seepage flux at the bottom boundary. For all these issues, the local temperature deviations can highly influence the inversion step, yielding a high noise in the outcome. Nevertheless, we see potential in a less complicated inversion of the growth of an unconditionally stable layer above a cold and saline boil after the water body is fully mixed. This approach still requires high-resolution temperature measurements. Further research to this method is recommended.

Samenvatting

Dit proefschrift onderzoekt een nieuwe meetmethode om de kwelwaterafvoer uit wellen te kwantificeren. Wellen zijn lokale bronnen van grondwaterkwel en zijn een gevolg van grondwaterstroming dat zich een weg door de bodem baant middels het creëren van zandpaden met een hoge doorlatendheid. In Nederland komen wellen vaak voor in diepe polders (drooggelegde meren op 4–7 m onder zeeniveau), waarbij ze water direct vanuit de diepe watervoerende laag aanvoeren. Omdat deze zoute watervoerende laag direct verbonden is met de zee, is het drukverschil tussen de zeewaterstand en de polderwaterstand de belangrijkste drijfkracht van de opwaartse kwelflux. Aan het oppervlak stromen wellen vaak uit in de slootbodem en soms op land. Dit proefschrift concentreert zich op wellen die direct in poldersloten uitstromen. Hoewel wellen normaal gesproken zeer zout zijn in vergelijking met het zoete oppervlaktewater, bevat dit onderzoek ook een voorbeeld van een relatief zoete wel.

De grondwaterkwel heeft een vrijwel constante temperatuur door het jaar heen. Omdat de oppervlaktewatertemperatuur over het jaar en over de dag varieert, is temperatuur een ideale tracer om de interactie tussen grondwater en oppervlakte-water te meten. Eerdere studies benutten temperatuur- en zoutmonsters op ver-schillende dieptes in de bodem om de welflux te kwantificeren. Omdat de paden van wellen over het algemeen niet precies verticaal zijn en verstoord kunnen worden wanneer in de bodem wordt gemeten, heeft dit onderzoek tot doel om de welflux vanuit oppervlaktewaterperspectief te meten. De beoogde meetmethode bemon-stert het oppervlaktewater met een zeer hoge resolutie in drie dimensies, vergelijkt de temperatuurprofielen met die in een transportmodel met een vrij oppervlakte, en herleidt de welflux als de randvoorwaarde aan de bodem in het model.

Over de afgelopen decennia heeft ruimtelijk gespreide temperatuurbemeting met glasvezelkabels (DTS) zich ontwikkeld tot een effectieve manier om in de ruimte gespreide temperatuurmonsters te verkrijgen. Wanneer een lasersignaal wordt ver-stuurd door een glasvezelkabel, bevatten de golflengtes van het terugkerende sig-naal temperatuurgegevens. De huidige DTS-apparaten bieden de mogelijkheid om temperatuur tot minimaal elke 25 cm langs de glasvezelkabel te meten. Om nog ho-gere resoluties te verkrijgen, wikkelen onderzoekers de kabels vaak tot een spoel. Echter, gebogen kabels en de ondersteunende constructie gaan vaak ten koste van de meetnauwkeurigheid. Hoofdstuk 3 onderzoekt hoe kabelbochten de tempera-tuurmetingen beïnvloeden in opgewikkelde DTS-opstellingen om hier rekening mee te houden in het ontwerp van een hogeresolutie-DTS-opstelling voor dit onderzoek. We concluderen dat kabelbochten met een kleinere boogstraal de temperatuurme-tingen op verschillende manieren toenemend benadelen. De non-lineariteit in de door bochten veroorzaakte signaaldemping bemoeilijkt de compensatie voor deze effecten en noodzaakt een zeer voorzichtige methode voor temperatuurkalibratie.

Om continu gebogen kabels te voorkomen, werd in het ontwerp van de driedimensionale (3D) DTS-opstelling een weefpatroon in plaats van spoelen toegepast (Hoofdstuk 4). Op deze manier zijn de kabels alleen gebogen bij elke ommekeer met tussenliggende rechte stukken van 1 m. Door de gewenste verticale ruimte tussen de gewoven lagen te kiezen kan men de verticale resolutie van de opstelling voor de eigen toepassing op maat maken. Om de kwelflux vanuit de slootbedding te herleiden, noodzaakte het ontwerp van de opstelling een erg hoge resolutie nabij de bodem. De opstelling toonde aan dat het zeer gedetailleerde temperatuurprofielen in een waterlichaam kan meten en onthulde zelfs onverwachte instromen in een laboratoriumopstelling om wellen te simuleren. In het veld toonden de gemeten temperaturen boven de slootbodem aan dat zich rondom de wellen sediment ophoopte gedurende de meetperiodes. Het meest interessant voor de huidige toepassing is dat de gedetailleerde profielen dubbel-diffuse fenomenen konden vastleggen.

Dubbele diffusiviteit treedt op wanneer twee aangrenzende waterlagen verschillende temperaturen en zoutgehaltes hebben en de dichtheidsgradiënten voor temperatuur en zout tegengesteld zijn. Wanneer bijvoorbeeld koud (zwaarder) en zoet (lichter) water bovenop warm en zout water ligt, ontwikkelt zich een systeem van convectieve lagen met een erg scherp temperatuur- en zoutgrensvlak tussen de convectieve lagen (d.w.z., dubbel-diffuse convectie). Een interessanter fenomeen treedt op wanneer een warme en zoute laag bovenop ligt. In dat geval ontwikkelt zich een vingerpatroon op het scherpe grensvlak tussen de lagen (d.w.z., zoutvingers). Deze systemen verschillen van normale diffusieve grensvlakken die de neiging hebben met verloop van tijd te vervagen. Om die reden vereisen waterlichamen met zout- en temperatuurgradiënten een voorzichtige modellering van de stromingen.

Om nauwkeurig het boven de wel gelegen waterlichaam te modelleren werd een massa- en momentumbehoudend vrije-oppervlaktemodel geselecteerd. Dit model werd uitgebreid met een transportmodule en modules die temperatuur- en zoutafhankelijke dichtheden, viscositeiten, en warmtecapaciteiten berekenen. Bovendien is het model uitgebreid met de optie om warmte-uitwisseling met de atmosfeer mee te nemen. De werking van het model is getest in een zonnevijver (Hoofdstuk 5). Dergelijke vijvers zijn waterlichamen met dubbel-diffuse convectie en zeer sterke dichtheidsgradiënten, die zonne-energie als warmte opslaan in de zeer zoute onderste laag. Het model legde de stroming van warm water langs de schuin oplopende oever goed vast en toonde het optreden van kleine seiches aan in de vijver als gevolg van de dichtheidsgradiënten. Het optreden van convectieve lagen werd ook vastgelegd, hoewel de afmetingen daarvan niet geheel overeenkwamen met de meetdata. Over het algemeen bevestigden de resultaten het vermogen van het model om dubbel-diffuse convectie te simuleren.

Vanwege de ronde vorm van de wel en de beschikbaarheid van 3D temperatuurprofielen geniet een 3D modelgrid de voorkeur voor welsimulaties. Het nauwe grid dat voor de transportmodellering nodig is, levert echter te lange rekentijden op. Om die reden hebben we in Hoofdstuk 6 het potentieel van een quasi-3D axisymmetrisch modelgrid onderzocht voor deze simulaties. Hiervoor werd de 2DV modelcode uitgebreid met enkele extra termen die de rekentijd nauwelijks deden toenemen en

de oplossingsmethode massa- en momentumbehoudend hielden. Met kwalitatieve case studies hebben we aangetoond dat het model zoutvingers en dubbel-diffuse convectie kan modelleren. Een analytisch benchmarkprobleem is opgesteld voor de axisymmetrische groei van een onvoorwaardelijk stabiele laag vanuit een koude en zoute wel. In het geval van laminaire stroming kwamen de modelresultaten over-een met de analytische oplossing. Turbulente convectie verspreidde de warmte en het zout significant sneller.

De onverwachte instromen in de laboratoriumopstelling voor welsimulaties maak-ten de vergelijking van deze metingen met modelresultaten gecompliceerd, omdat de exacte stroompaden onbekend waren en niet konden worden gemodelleerd. Hoofdstuk 7 vergelijkt de metingen met modelresultaten voor de beoogde kwel-stroom. Hoewel vergelijkbare dubbel-diffuse convectie en onvoorwaardelijk sta-biele lagen zich ontwikkelen in zowel het model als de meetresultaten, verschil-len de groeisnelheden en in het bijzonder de locaties waar deze lagen het snelste groeien. Bovendien lijken de onverwachte kwelstromen een hogere stroomsnelheid te hebben, die tot een grotere menging van warmte leiden op het grensvlak tussen de lagen. Dit leidde tot de conclusie dat het model niet gevalideerd kan worden op basis van de laboratoriumdata en dat het raadzaam is extra metingen te doen.

Hoewel de horizontale stroming door de sloot boven de wel verwaarloosbaar wordt geacht wanneer een axisymmetrische modelbenadering wordt toegepast, is kennis van deze stroming wel relevant. Om deze reden begint dit proefschrift met het verkennen van de mogelijkheden om de stijgende-bellen-methode voor het meten van rivierafvoer te moderniseren en mogelijk te automatiseren (Hoofd-stuk 2). De studie toont aan dat de ingewikkelde opstelling met twee camera's en de bijbehorende positieberekeningen uit eerdere publicaties vermeden kan worden met moderne fotobewerkingsalgoritmes. Reflecterend zonlicht verhindert soms de zichtbaarheid van luchtbellen op het wateroppervlak. We presenteren een voor-beeld van de manier waarop statistisch gereedschap de aftekening van luchtbellen, die normaal nauwelijks zichtbaar zijn, blootlegt in een digitale foto. Dergelijk ge-reedschap zou ook kunnen worden toegepast in patroonherkenningsalgoritmes die de luchtbellen automatisch op het wateroppppervlak opsporen. Hoewel verder on-derzoek noodzakelijk is, lijken de resultaten de hypothese te ondersteunen dat de stijgende-bellen-techniek kan worden toegepast als automatische afvoermeetme-thode.

We concluderen dat het herleiden van welfluxen uit dubbel-diffuse modellen op dit moment nog erg uitdagend is (Hoofdstuk 8). De locaties en afmetingen van dubbel-diffuse convectiecellen en zoutvingers zijn afhankelijk van processen op kleinere schaal dan de gridcelafmetingen. Bovendien zijn deze fenomenen erg gevoelig voor lokale dichtheidsgradiënten, die nooit 'perfect' worden gemodelleerd. Het belang van de randvoorwaarden wanneer de onderste laag van kwelwater nog dun is zou ook de herleiding van de welflux aan de bodem kunnen benadelen. In al deze gevallen kunnen lokale temperatuurafwijkingen de herleidingsstap in belangrijke mate beïnvloeden, leidend tot een grote ruis in de resultaten. Van de andere kant zien we potentieel in een minder ingewikkelde herleiding van de welflux uit de groei van een onvoorwaardelijk stabiele laag boven een koude en

zoute wel vanuit een situatie waarin het oppervlaktewater volledig gemengd is.
Deze benadering vereist nog altijd de temperatuurmetingen met hoge resolutie.
Meer onderzoek naar deze methode wordt aanbevolen.

1

Introduction

1

This thesis focuses on the measurement and modelling of local groundwater seepage flows in deltas. This specific form of seepage is called boil seepage, and often yields transport of saline water from the deeper aquifers toward the relatively fresh canals that drain the low-lying land surface. The constant temperature of the seepage water most of the time contrasts the time varying surface water temperature. This research aims to measure the seepage flow by measuring the development of a 3-D temperature profile in the surface water with an innovative distributed temperature sensing (DTS) set-up, and link these temperature profiles to the seepage inflow with a density-driven free-surface model. To reduce calculation times for the dense 3-D grid, the model allows an axisymmetric grid definition around the location of the boil.

The free-surface model (Chapter 6) is able to simulate detailed convection and stratification processes in water systems with salinity and temperature gradients. Therefore, it is also applicable to comparable smaller-scale stratified systems. This thesis presents an application to a solar pond, where thermal energy from solar radiation is stored in a hypersaline water layer in the pond, which is covered by a lighter fresh water layer.

Seepage inflows directly influence the discharge in the draining surface water system as well. The rising bubble technique is amongst the discharge measurement methods that increase their potential of convenient application with the current developments in image processing techniques. This thesis shows how these advanced techniques can facilitate the rising bubble technique with applications in different systems varying from a quiescent flow in a canal to a more turbulent river flow.

This chapter starts with the introduction of saline groundwater seepage as the main topic of this thesis (Section 1.1). Section 1.2 gives an introduction to the field of monitoring groundwater - surface water interaction, and Section 1.3 focuses on the developments of the DTS technique specifically. Since the boil seepage and the stream water have a contrasting salinity and temperature, double-diffusive phenomena might occur. The own and very specific research field that studies these phenomena is briefly introduced in Section 1.4. Finally, Section 1.5 sets out the research questions of this thesis.

1.1 Saline groundwater seepage in deltas

Deltas have always been an interesting area to live: abundant food from agriculture and fisheries, opportunities for economic activities by the ease of access, fresh water availability from upstream, and often a relatively mild climate provide the right circumstances to survive. The deltaic populations put a high demand on fresh water resources. Apart from direct consumption, fresh water is for example also used for agriculture, industry, and energy production (Food & Agriculture Organization of the United Nations, 1997). On the other hand, low-lying deltas are commonly protected by dikes and drained to prevent them from flooding. These activities, together with sea level rise and climate change, make the deltas prone to enhanced saltwater intrusion, as will be explained in the next paragraphs. Consequently, salinization increasingly threatens delta live worldwide, as less fresh water
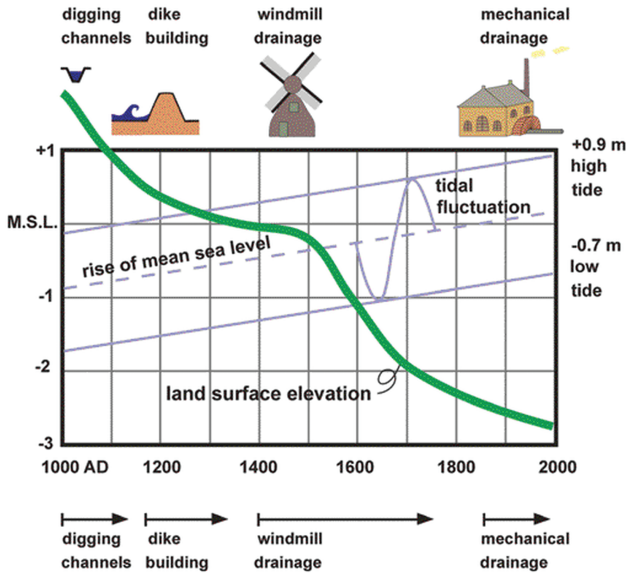
Figure 1.1: Relative sea level rise in the Netherlands: land subsidence versus sea level rise (Van de Ven, 1993).

is available for human consumption and activities, and ecological systems are put under pressure.

In low-lying deltas, the relatively high sea levels often cause induce groundwater seepage fluxes from the deeper saline aquifers, which are directly connected to the sea. The topping fresh aquifers and surface water systems are usually drained mechanically to keep the land in these deltas dry, which enhances the upward seepage fluxes that relief the over-pressure in the saline aquifers. The saline seepage is an important cause of increasing salt concentrations in the surface water systems (ICW, 1976; Pomper and Wesseling, 1978; Van Rees Vellinga et al., 1981; Oude Essink, 1996; De Louw, 2013).

Future sea-level rise will enhance saline groundwater intrusion by increasing the pressure differences between the sea level and inland water levels (Oude Essink et al., 2010; Giambastiani et al., 2007). Additionally, peat oxidation and clay shrinkage cause land subsidence, as a consequence of the controlled low water levels. Fig. 1.1 shows a millennium of relative sea level rise, taking into account sea level rise and land subsidence, for the Rhine river delta in the Netherlands (Van de Ven, 1993). The subsidence and salinization of the Rhine delta is one example out of many, like the Mekong, Ganges, and Po river deltas.

Another interesting example is the low-lying Yellow River delta, where the increasing upstream consumption of the fresh water leaves a low discharge at the river mouth. The low river discharge allows the Bohai Sea water to intrude further inland via the river estuary and the groundwater layers which are in direct connection with the sea (Van der Most, 2009; Dong, 2014). This situation both limits
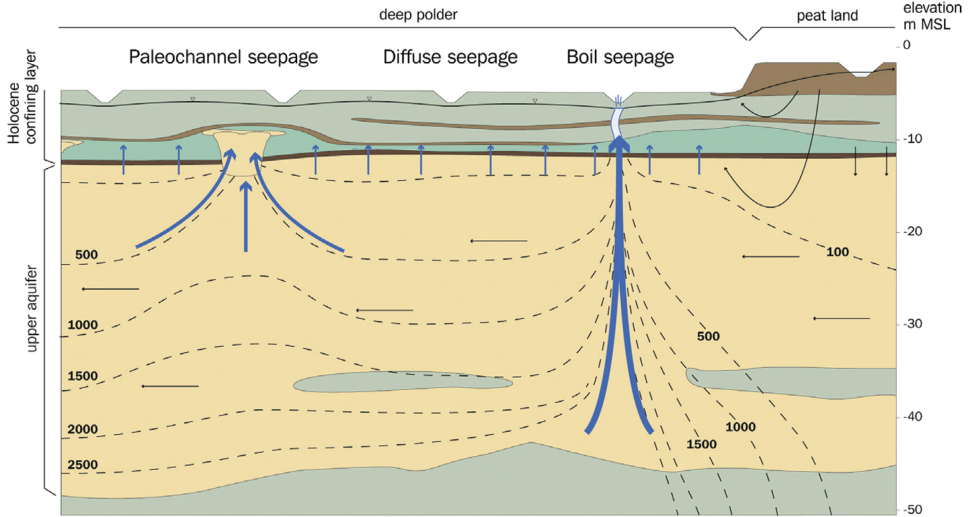
Figure 1.2: Diffuse seepage, paleochannel seepage and boil seepage (De Louw et al., 2010).

the consumption of fresh water for the fast growing population and industry in the delta, and stresses the water quality for the deltaic ecology and agriculture. In the Rhine delta, fresh water from upstream is used to flush the areas subject to salt intrusion (Van de Ven, 1993). The Rhine discharge is still sufficient most of the time to allow this, although some droughts over the past decades have already demonstrated the fragility of this practice (Zwolsman and Van Bokhoven, 2007). For the future, climate change jeopardizes the continuous upstream supply of fresh water even more (Oude Essink et al., 2010).

The way in which upward seepage overcomes the pressure difference between the saline aquifer and the fresh surface water system depends on the geological situation. The soils in low-lying deltas commonly consist of confining peat and clay layers, and diffuse seepage is the usual form of upward groundwater flow: the upward flux is about equally distributed over the surface area and the flow velocities are low. When on some locations these low-permeable confining layers are permeated by higher-conductive material, the seepage flux will be locally enhanced through these preferential flow paths. The need to take into account these preferential flow paths to explain water and chloride balances in such systems for example appears from studies to deep polders in the Netherlands, which are situated 4–7 m below mean sea level (ICW, 1976; Van Rees Vellinga et al., 1981; De Louw et al., 2010). Here, a *polder* is defined as an enclosed area with a controlled water level, where the water system has no direct connection to the water systems in the surrounding areas.

De Louw et al. (2010) describes two types of preferential seepage for several studies in polders in the Netherlands: seepage via paleochannel belts and via localized boils (Fig. 1.2). Paleochannels are former channels that partly cut through the confining layer of clay and peat deposits, and are filled with sand (Berendsen and
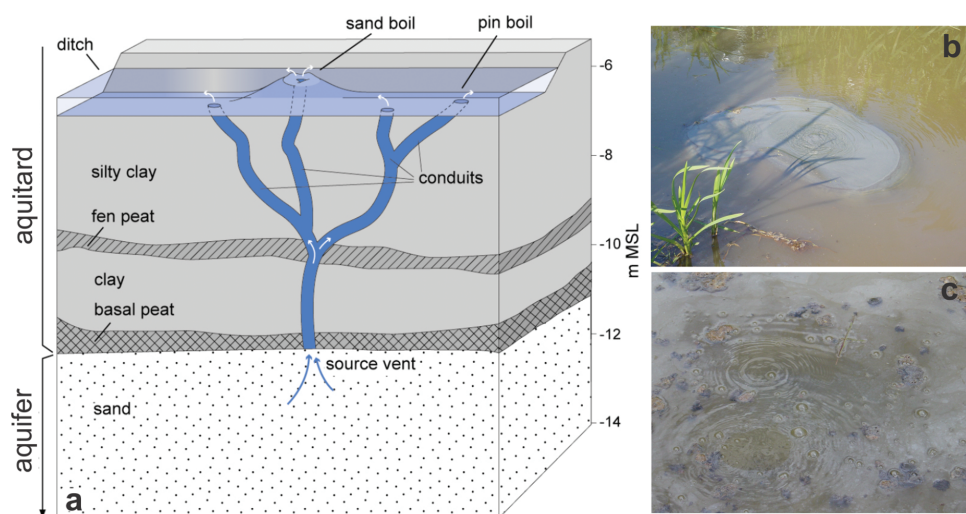
Figure 1.3: **a)** Schematized boil conduits. **b)** A sand volcano. **c)** Boils sometimes transport methane gas from the subsoil (De Louw et al., 2010).

Stouthamer, 2000). This permeable material favours the upward seepage of saline water from the deep aquifer. For the Noordplas Polder, De Louw et al. (2010) found average chloride concentrations of $600\,\mathrm{mg\,l^{-1}}$ for paleochannel seepage, which was approximately 6 times the chloride concentration of the diffuse seepage flux. An average chloride concentration of even $1100\,\mathrm{mg\,l^{-1}}$ was found for the boil seepage fluxes.

Boil seepage is seepage that finds its way up through small vents, which are a direct consequence of the water pressure differences. Because the overpressure of water in the lower aquifer exceeds the pressure exerted by the weight of the overlying stratum, heaving and cracking can occur. This mechanism leads to the development of flow pathways that allow a high-velocity upward flow of water from the lower aquifer. These vents are called boils, and can be compared to the mechanism of piping through levees, where pressure-induced heaving and cracking also induces flow paths underneath the levee. Both piping and boil seepage are often visible by the occurrence of sand boils in ditches, and sometimes also on the land surface (e.g., Kolb, 1976; Sellmeijer and Koenders, 1991; LaFleur, 1999). *Sand boils*, or sand volcanoes, are formed from the material that was blown out by the eroding water flow through the vent (Fig. 1.3). Contrary, *pin boils* have not developed towards large vents, and are often visible from the surface as small cracks in the soil containing liquefacted soil material (De Louw, 2013). Boils can be easily spotted when they collapse ditch banks, or during winter when the warm seepage water locally prevents ice growth. Sand boils are not to be confused with sand blows: sand boils are caused by pressure differences, whereas sand blows are vents caused by earthquake-induced liquefaction (Holzer and Clark, 1993; Li et al., 1996).

1

Multiple studies in polders in The Netherlands confirm that preferential flow paths are a major source of salinization (Oude Essink et al., 2010; De Louw et al., 2010, 2011, 2013; Delsman et al., 2013; Vandenbohede et al., 2014). In particular, saline boil seepage imports high salt loads into the polders. This is a consequence of saltwater upconing, which is the concentrated high-velocity transport of saline groundwater through a small horizontal cross-section. De Louw et al. (2011) quantified that boils discharged 66 % of the salt flux into the Noordplas Polder, despite their contribution to the water balance of only 15 %, implying that the high salt concentrations are a more important factor for the salinization than the seepage discharge itself. De Louw (2013) mentions maximum recorded boil salinities of 5000 mg l^{-1} in the Haarlemmermeer Polder, The Netherlands. An end-member analysis by Delsman et al. (2013) even found an average salinity of 5453 mg l^{-1} in the Lissertocht Catchment, with a maximum of 6590 mg l^{-1} (i.e., 19 % of the sea water salinity). Their main conclusion is that boil seepage water, although it mixes with fresh water on its way to the surface, maintains a high salinity.

The contribution of boils to the salinization of deep polders and their localization make them interesting study objects. First of all, quantification of their seepage discharge and the imported salt load are of interest for studies of current and future salt water intrusion. Second, the very local nature of the boils offers the opportunity to test new ways to measure preferential groundwater - surface water interaction. And third, the inflow of salt water into a fresh surface water body of different temperature causes interesting thermohaline stratification.

1.2 Measuring groundwater– surface water interaction

Hydrologists have always been searching for methods to accurately quantify hydrological fluxes. Some fluxes, like precipitation and river discharge are relatively easy to quantify. Other fluxes, like groundwater flow, are less obvious to quantify. One of the fluxes that has long time been difficult to quantify appropriately, is the interaction between groundwater and surface water. For this reason, it was also difficult to account for this flux in hydrological models (Lee, 1977). Depending on the geological circumstances, a model can lead to erroneous results if groundwater - surface water interaction is unaccounted for. Calibrating a model to this flux raises the risk that the model uses this term to compensate for other fluxes. Rough measurements could already serve as constraint, and obviously model results are usually improved with more accurate measurements. Over the past, several measurement methods have been developed.

1.2.1 Available measurement methods

The most direct and intuitive way of measuring groundwater exfiltration, is by directly measuring its volume with a *seepage meter*. The original design of the seepage meter was an inverted open drum, which is buried few centimetres into the stream bed. The water exfiltrating into the cylinder is vented towards a deflated plastic bag, which is also located under water and used to record the volume of wa-

ter exfiltrating over time (Lee, 1977; Conant, 2004). Disadvantages of this method are the relatively low accuracy of most devices and the need to spatially interpolate the measurements where the seepage phenomena can be very location-specific (Brodie et al., 2009). Further, at low exfiltration rates, a long time integration is necessary to reach a large enough volume for accurate measurements. This is usually overcome by attaching flow meters to the seepage meters in order to measure the flow directly instead of filling a plastic bag (Rosenberry et al., 2013). A special constant head type seepage meter, called Idaho seepage meter, has been developed to measure surface water infiltration (Byrnes and Webster, 1981).

More commonly, the direction and the amount of flow is measured indirectly using multiple *piezometers* (Dages et al., 2008; Cirkel et al., 2010). The seepage quantity can be calculated by applying Darcy's law to the head differences, which requires knowledge about the soil's hydraulic conductivity. Often, seepage flows are derived from geohydrological models based on large sets of piezometer heads. Compared to seepage meters, this method spatially integrates seepage rates over a larger area. However, care should be taken applying hydraulic conductivities in heterogeneous soils. According to Rosenberry et al. (2013), measuring hydraulic gradient as a surrogate for seepage works well in many settings. However, they may be misleading in short term measurements with changing hydraulic properties, and if flow paths are not aligned with the axis of the well screen and sediment bed.

Another common way of measuring groundwater - surface water interaction employs natural or artificial *tracers* in the infiltrating or exfiltrating water. Artificial tracers are added to the water as chemicals or by heating the water (Shafer et al., 2010; Westhoff et al., 2010; Jonsson et al., 2003). Novel artificial tracers are under development, like microbial tracers (Rossi et al., 1998) and synthetic DNA (Foppen et al., 2011). On the other hand, the sources of water are often already naturally distinctive based on their chemical or isotopic composition, or based on their temperature. These natural tracers are often applied in hydrograph separation techniques, although it is advocated not to use tracers for this purpose without coupling them to hydrometric monitoring (Rice and Hornberger, 1998; Renaud et al., 2007). A further important application of tracers is end-member analysis to quantify the contribution of a source to a water body (Hooper et al., 1990; Katz et al., 1998; Delsman et al., 2013). Lastly, tracers are employed for qualitative research, for example to the occurrence of flow paths and to stream bed properties (Conant et al., 2004).

1.2.2 Heat as a tracer

Water temperature has been used as a quantitative hydrological tracer since the early sixties of the previous century (Stallman, 1963; Bredehoeft and Papadopulos, 1965). However, already during the early 1900s, it was recognized that groundwater flow transfers heat (Bouyoucos, 1915; Stonestrom and Constantz, 2003). In 1935, Theis denoted the analogy between Darcy's law and the law of the flow of heat by thermal conduction,

"hydraulic pressure being analogous to temperature, pressure-gradient to thermal gradient, permeability to thermal conductivity, and specific
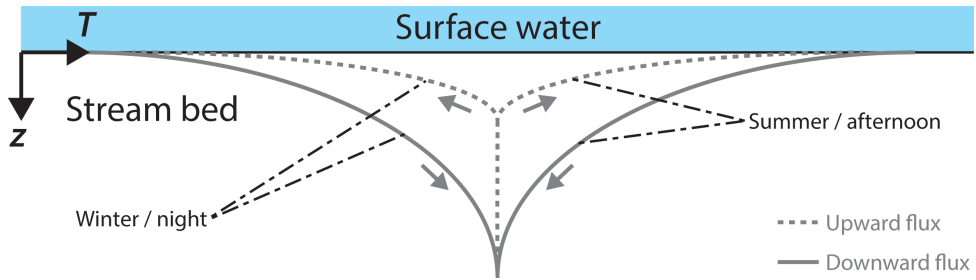
Figure 1.4: Annual / diurnal stream bed temperature (T) profile over depth (z).

yield to specific heat." (Theis, 1935)

Theis used the analogy with Fourier's mathematical theory of heat conduction to apply existing analytical solutions for heat sources and sinks to recharging and discharging wells respectively. Other researchers have applied this same analogy in other studies, for example to describe convective processes in porous media (Elder, 1967a,b).

Decades before Theis, researchers already recognized that temperature was more than only a water quality parameter. In 1905 for example, Slichter applied heat as a groundwater tracer, noting the effect of an increase in infiltration from a pond on the groundwater temperature (Slichter, 1905; Anderson, 2005). However, it was only in 1963, and after the publication of Theis, that Stallman published an equation for analytical studies to groundwater flow based on the simultaneous conduction and convection of heat in groundwater systems (Stallman, 1963). Afterwards, Bredehoeft and Papadopulos (1965) applied this equation to estimate vertical groundwater flow from the soil's thermal profile over depth using a 'type-curve' procedure. These curves have convex or concave shapes, representing downward or upward flow, respectively. The meaning of these shapes is analogous to the simple representation of the temperature profile dependency on flow direction through the stream bed (Fig. 1.4). This figure also shows the temperature profile variation with the diurnal and annual cycle of surface water temperature.

Type-curves represent a signature of the local seepage flow. Like in a endmember analysis, the contrasting temperature acts as a tracer whose signature is imposed at a point source (e.g., an inflow from a drainage canal) or over a stretch (e.g., a gaining river). Which type of inflow occurs, determines which type of measurement is appropriate.

Thermocouple or thermistor-based temperature sensors can be applied for point measurements at a single local inflow (Silliman and Booth, 1993; Land and Paull, 2001; Bianchin et al., 2010; Keery et al., 2007). The low costs and easy applicability make thermistors also attractive to apply in larger numbers to obtain distributed temperature data. The vertical temperature profile in the stream bed, for example, can be measured by placing thermistors on several depths. The disadvantage is that the data should be downloaded from the individual thermistors, which should first be excavated. The TROD presented by Naranjo and Turcotte (2015) overcomes

these issues, allowing instantaneous measurements at six different depths. For the shallow subsurface of sand-bed streams, Angermann et al. (2012) applied active heat pulses to measure hyporheic exchange at the sediment water interface, using a set-up with both temperature sensors and a central heater.

Distributed temperature data of the surface water can be collected by remote sensing (Souto-Maior, 1973). Depending on the scale of the measurements, thermal infra-red cameras can be installed ground-based on few metres above the ground (Pfister et al., 2010), or on helicopters (Loheide and Gorelick, 2006) or unmanned aerial vehicles (UAVs) (Jensen et al., 2012). The advantage of this method is the possibility to obtain quick distributed temperature data over a large area while the spatial distribution can still be relatively high (Loheide and Gorelick, 2006). Disadvantages are the higher costs and the fact that only a water surface image is obtained. The latter disadvantage makes application in this PhD research infeasible, as the dense boil seepage water locally stratifies the surface water (Silliman and Booth, 1993). However, thermal infra-red mapping can help localizing boil locations (De Louw et al., 2010).

A recent development to acquire distributed temperature data is fibre-optic distributed temperature sensing (DTS), which allows relatively inexpensive measurements at custom locations over depth and along streams (Selker et al., 2006a; Tyler et al., 2009). One of the major advantages of fibre-optic DTS is the opportunity to obtain temperature data over large distances. Current DTS equipment allows measurements up to 35 kilometres with, depending on the measured distance, a spatial resolution down to 0.35 metre. To measure at even higher resolutions, researchers often wrap the fibre-optic cable around a cylinder (Section 1.3.3). Westhoff et al. (2007; 2010) applied DTS to locate and quantify groundwater - surface water interaction along a fast flowing head water stream. By obtaining high-resolution depth profiles of the stream and stream bed temperature, Vogt et al. (2010; 2012) studied infiltration rates and the riparian groundwater flow near a losing river section. In deep polders, Hoes et al. (2009) managed to identify boil seepage locations based on their temperature differences. Section 1.3 reviews the developments and measurement principle of DTS in detail.

1.3 Distributed temperature sensing

1.3.1 Historical developments

Today's optical fibres find their origin in Narinder Singh Kapany's finding during the 1950s that bundles of glass fibres, by refractioning, can transport optical signals. In this time, Kapany's research found its largest purpose in medical imaging (Bose, 2010). The next decade, the main purpose of research to fibre-optics shifted towards the development of communication systems. Kao and Hockham (1966) presented theoretical and experimental studies that indicated the potential of optical fibres as a new communication medium. Although communication purposes boosted further research during this decade, the early 1970s brought the first experiments on low-loss optical fibres for a different purpose: sensing (Grattan and Meggitt, 2000). Ever since, advances in fibre-optics for communication have

largely improved the quality of measurements and increased the applications for sensing. In 1985, Dakin et al. (1985) were the first to measure temperature with a semiconductor laser and optical fibres using the temperature dependency of Raman spectra.

The large spendings of the oil and gas industry on research and development made them among the first industries to apply the fibre-optic cable as a temperature sensor on a larger scale, with a large increase of applications in the 1990s. The distributed temperature sensing of boreholes served as an efficient replacement for temperature measurements with a moving probe. In this industry, temperature profiles of oil and gas wells are predominantly used to locate inflow locations and the flow rate distribution of fluid entering the well by temperature deviations from the geothermal gradient (Hurtig et al., 1994; Smolen and van der Spek, 2003).

In the 2000s, environmental scientists started to recognize the similarities of their temperature sensing studies with the applications of DTS in the petroleum industry. Ever since, DTS has been applied in a variety of studies. Examples of hydrological applications include the measurement of temperature profiles in stratified water bodies (Tyler et al., 2009; Suárez et al., 2010a; Arnon et al., 2014a), soil moisture estimation (Steele-Dunne et al., 2010; Ciocca et al., 2012), groundwater flow measurement (Read et al., 2013; Bakker et al., 2015), and the identification and measurement of seepage fluxes in stream beds (Lowry et al., 2007; Hoes et al., 2009; Vogt et al., 2010; Krause and Blume, 2013; Sebok et al., 2015).

Over the past decades, the improvements in DTS devices, fibre-optic cables, installment options, and calibration methods have increased the accuracy and applicability of DTS. As an example, double-ended calibration interrogates the fibre temperatures from both cable ends to decrease inaccuracies caused by differential attenuation (this term is explained in Section 1.3.2), although it requires twice the amount of input channels and sensor length capacity, and doubles the minimum measurement rate (Tyler et al., 2009). Alternatively, a duplexed system, where two co-located fibres are connected at the far end, still allows an improved calibration by matching cable sections and requires only one input channel per fibre, although this is on the cost of a lower accuracy in the fibre that is not directly interrogated. Manual calibration of single-ended and double-ended set-ups usually provides a better measurement accuracy compared to the standard DTS machine calibration procedures (Hausner et al., 2011; Van de Giesen et al., 2012). Recently, manufacturers started to develop DTS machines with two lasers, where the wavelength of the Stokes return signal of one laser closely matches the wavelength of the anti-Stokes return signal of the other laser (Lee, 2007; Suh and Lee, 2008; Suh et al., 2008; Tyler et al., 2009). This way, differential attenuation effects can be largely eliminated from the measurements.

1.3.2 Measurement technique

Several measurement principles exist for fibre-optic distributed temperature sensing. Fibre Bragg grating employs a closely spaced set of scratches at the surface of the fibre to filter certain wavelengths. The filtered wavelengths are dependent on the spacing of the gratings, and as such on the local expansion of the cable (Selker
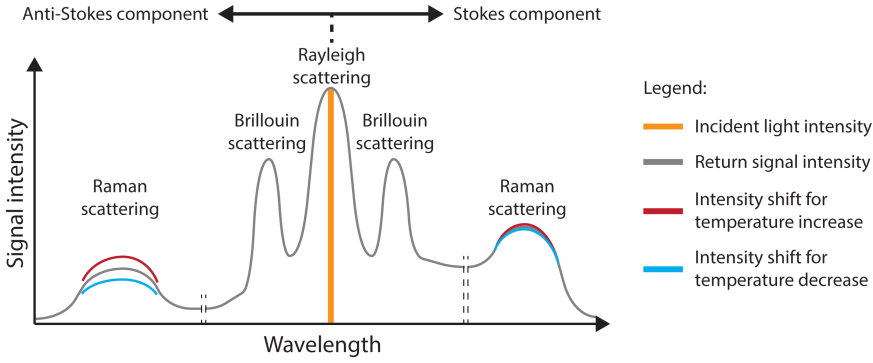
Figure 1.5: Rayleigh, Brillouin and Raman scattering bands of the returning laser signal. The Raman anti-Stokes intensities are highly temperature sensitive.

et al., 2006a). Besides a temperature sensor, Fibre Bragg grating is therefore also applied as a strain sensor.

Raman DTS, which is employed in this research, is among the measurement principles that employ the collapses of photons with discontinuities in the glass structure of the fibre. These collapses cause part of the photons to exchange energy with electrons, resulting in wavelength shifts. A photon's energy emission yields a wavelength increase, whereas an energy gain yields a wavelength decrease. The scattered light therefore consists of light modes with the original wavelength (elastic Rayleigh scattering) and light modes with shifted wavelengths (non-elastic Brillouin and Raman scattering), as shown in Fig. 1.5.

Raman and Brillouin scattered light are clearly discernible by their distinct wavelength bands, both at higher wavelengths (Stokes component) and lower wavelengths (anti-Stokes component). The anti-Stokes wavelength band of the Brillouin scattered light shifts with a changing density of the glass fibre. Brillouin scattered light can therefore be used as a temperature and strain sensor.

For Raman scattered light, the light intensity of the anti-Stokes component is exponentially dependent on temperature and linearly dependent on the light intensity. Raman DTS cancels out the dependency on light intensity by taking the ratio of the Stokes and anti-Stokes scattered light intensities. The exponential relationship with temperature is then employed to calculate the temperature at a distance z:

$$T(z) = \frac{\gamma}{\ln\left(\frac{P_S(z)}{P_{aS}(z)}\right) + C - \Delta\alpha z} \tag{1.1}$$

where P_S (-) and P_{aS} (-) are the Stokes and anti-Stokes signal intensities, γ (K) represents the shift in energy between a photon at the incident wavelength and the scattered signal wavelength, C (-) is a calibration parameter that encompasses properties of the incident laser and the DTS instrument, and $\Delta\alpha$ (m^{-1}) represents the differential attenuation between the Stokes and anti-Stokes light intensities along the cable (Hausner et al., 2011; Van de Giesen et al., 2012). The signal intensities can therefore be determined for each location z based on the total time

1

t needed for the light signal to arrive at the location where it scatters and return to the DTS machine:

$$z = \frac{v_l \cdot t}{2} \tag{1.2}$$

where v_l (m s^{-1}) is the speed of light in the glass fibre, which is related to the speed of light in vacuum c_l (m s^{-1}) by its refractive index n (-): $v_l = c_l/n$ (Smolen and van der Spek, 2003).

Manual calibration often outperforms the accuracy of the DTS machine's automatic calibration procedure. Hausner et al. (2011) and Van de Giesen et al. (2012) presented manual calibration procedures to calibrate single-ended and double-ended set-ups, respectively, by manually calibrating the parameters $\Delta\alpha$, γ, and C in Eq. 1.1. Double-ended and duplexed cable set-ups allow the discrete calibration of the distance-dependant differential attenuation $\Delta\alpha(z)$ for multiple cable sections (Van de Giesen et al., 2012), and is therefore preferred whenever non-uniform differential attenuation is suspected (e.g., in case the cable installation is likely to cause microbends in the fibre, or when a cable is wrapped to a coil).

1.3.3 Enhanced-resolution DTS

Geoscientific applications of DTS often require a high resolution in space and time. When the required spatial resolution exceeds the maximum resolution provided by the instrument, researchers often use a set-up of coiled fibre-optic cables to enhance the resolution (Vogt et al., 2010; Suárez et al., 2011; Vercauteren et al., 2011). New developments in cable technology even include cables with internally coiled fibres (e.g., the BRUsens 70 °C high-resolution cable, Brugg Cables, Brugg Switzerland).

Figure 1.6: Graphical representation of used terms (machine resolution, coil resolution, and the stuffing factor defined as length L over pitch p).

Tyler et al. (2009) defined *spatial resolution* as the cable distance required to measure 90 % of a sharp temperature jump. The spatial resolution is different from the spatial *sampling interval* by the fact that the Nyquist theorem requires at least twice the interval to reconstruct a continuous signal. This thesis uses the terms *machine resolution* and *coil resolution*. The machine resolution is equal to the definition by Tyler et al. (2009) of the spatial resolution along a linear section of fibre-optic cable. The coil resolution is the effective spatial resolution of the temperature measurements equal to the machine resolution divided by the coil's stuffing factor. The *stuffing factor* is calculated from the length L of a cable within one turn divided by its pitch p (Fig. 1.6).
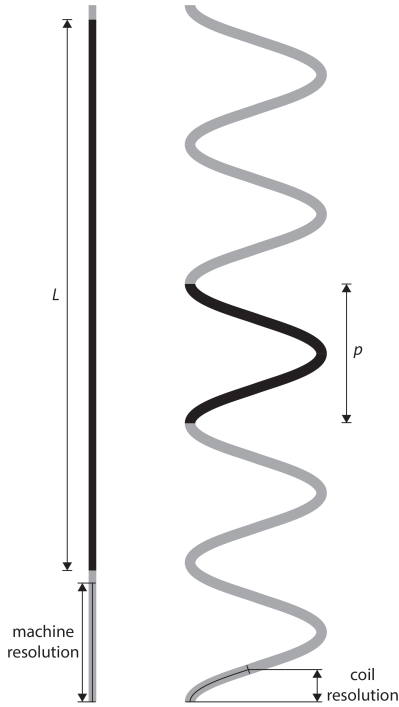
Hilgersom et al. (2016d) have shown that one should be careful using set-ups with a bent fibre, especially when the machine calibration procedure is applied (Chapter 3). The Stokes and anti-Stokes components of the returning laser signal experience different attenuations when entering a fibre bend. Since the temperature measurement method is based on the ratio of the Stokes and anti-Stokes components, fibre bends directly influence the temperature measurements themselves. The calibration approach presented by Van de Giesen et al. (2012) applying a piecewise linear fit to the differential attenuation could to a large extent compensate for these attenuation effects.

Another issue of coil-wrapped DTS is the auxiliary structure around which the fibre-optic cable is usually wrapped, which is often a PVC (polyvinyl chloride) tube (Hilgersom et al., 2016d). Solar radiation heats up the cable and the auxiliary construction with a high heat capacity. Due to the large amounts of heat stored in the auxiliary construction, the effects of solar radiation can remain up to several hours, influencing the temperature measurements indirectly. Previous modelling studies have shown the effect of solar radiation on fibre-optic DTS measurements (Sayde et al., 2015; Hilgersom et al., 2015).

This thesis aims to develop a DTS set-up that minimizes the negative effects of fibre bends and solar radiation, and provides high spatial resolution in three dimensions (Chapter 4). Such DTS set-ups could for example support the measurement of detailed processes in surface water bodies (Hilgersom et al., 2016c).

1.4 Thermohaline gradients in water bodies

The purpose of this research is to quantify the salt water flux into deltas with a numerical transport model and measurement of densely spaced temperature samples in the surface water. Since flow velocities in the drainage canals of polder systems are low most of the time, a well-mixed assumption for the whole cross-section as in Westhoff et al. (2010) is not valid. For this reason, the numerical model needs to account for depth variations in salt concentrations and temperature. Water bodies with thermohaline (i.e., temperature and salinity) gradients form a special field of research. Extensive research has been performed to the effects of double-diffusion in these systems. This section provides a short historical review.

W. Stanley Jevons is the first person known to describe the interesting effects of varying molecular diffusivities, when he did the following laboratory study (Jevons, 1857). In an attempt to model cirrus clouds, he prepared a system of warm water with dissolved sugar overlying cool water without sugar. Jevons found the onset of narrow, long convection cells. Inspired by these results, Rayleigh (1883) described the frequency of internal waves in fluid systems of variable density. Later, Rayleigh (1916) found the conditions on which convective cells occur under density variations, when he equated the dissipating forces (i.e., diffusivity of momentum and mass) to the impelling forces (buoyancy). Nonetheless, it was only in the second half of the twentieth century that oceanographers recognized differences in molecular diffusivities of heat and solutes as a driving force for convection. This recognition appeared the last missing link to explain Jevons' results and a boost for further research to double-diffusivity, mainly in the field of oceanography.

1

a) Salt-fingers

b) Double-diffusive convection

Legend: ■ Cold and fresh   ▨ Warm and saline   ⟳ Convective flow
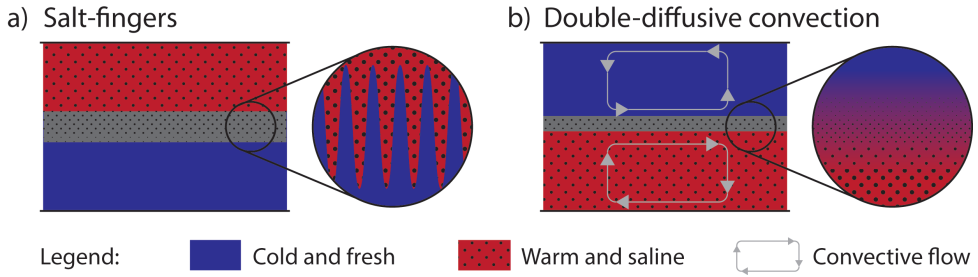
Figure 1.7: Schematization of double-diffusion in layered water systems with warm and saline water overtopping (a) and underlying (b) a cold and fresh water layer.

In 1956, Stommel et al. published their findings on the perpetual salt fountain. They showed that a continuous flow could be maintained through a long vertical tube in a stratified system with warm, salty water on top of cold water of a lower salinity. Unlike salt, heat is conducted through the wall of the tube. Consequently, the rising water with lower salinity heats up and, therefore, becomes relatively light. This system can be maintained when the top layer remains heated.

Stern, the person often credited for discovering double-diffusion, presented an analytical approach to predict the length of the salt fingers, which showed comparable results with experiments by Stommel and Faller (Stern, 1960). Turner (1965; 1967) analysed the effects of turbulent transport of salt and heat for the cases of double-diffusive convection and salt-fingering (Fig. 1.7). For double-diffusive convection, ratios of the salt and heat transport rates appeared systematically dependent on the density ratio, whereas for salt-fingering the ratios of the transport rates was found constant and independent of the density ratio. The "4/3 power law" derived for the salt flux over a salt-fingering interface is still applied to estimate the total salt transport in such systems and to validate numerical salt-finger simulations (Yoshida and Nagashima, 2003), although internal wave-shear and strain make the law inapplicable for the oceanic scale (Kunze, 2003). Both for salt fingering and double-diffusive convection, diffusion increases the density gradients between two layers, maintaining its stratification (Ruddick and Gargett, 2003).

In lakes and oceans, the amount of distinct thermohaline layers usually exceeds two. Tait and Howe (1968) discovered a so-called thermohaline staircase from temperature and salinity measurements near the Mediterranean water intrusion in the North-East Atlantic. Turner (1968) predicted the layer thicknesses of a laboratory scale staircase for double-diffusive convection, and Stern and Turner (1969) extended this work to the case of salt-fingering.

The relative strength of double-diffusive activity is often expressed by the density ratio $R_\rho = -N_T^2/N_S^2$ with the local temperature stability $N_T^2 = -g \cdot \alpha_V \cdot \partial T/\partial z$ and the local salinity stability $N_S^2 = g \cdot \beta_V \cdot \partial S/\partial z$ (Turner, 1973). Here, g is the gravitational acceleration (m s^{-2}), α_V is the thermal volumetric expansion coefficient (K^{-1}), β_V is the solutal volumetric expansion coefficient (-), and the z-axis is defined in downward direction. R_ρ is used as a metric for local stability as it describes the ratio of the stabilizing and the destabilizing gradient (i.e., the temperature and

salinity gradients) (Berthold and Börner, 2008).

Due to the ambiguity of R_ρ (i.e., two different regimes of thermohaline gradients could yield the same density ratio), Ruddick (1983) proposed the Turner angle Tu:

$$Tu = \arctan\left(\frac{N_T^2 - N_S^2}{N_T^2 + N_S^2}\right) \cdot \frac{180°}{\pi} \tag{1.3}$$

where the four quadrant arctangent function preserves the sign of the density gradients. This way, the Turner angle is a unique metric for all potential thermohaline gradients in a water body. A stable system occurs for $|Tu| < 45°$, whereas $|Tu| > 90°$ yields a gravitationally unstable system. Double-diffusive convection occurs for $-90° < Tu < -45°$, and salt-fingering for $45° < Tu < 90°$.

The global stability, expressed by the Brunt-Väisälä frequency $N^2 = N_T^2 + N_S^2$, is defined as the frequency by which a displaced particle in a stratified fluid oscillates around its original level based on the density gradient (Berthold and Börner, 2008). A positive N^2 indicates that the water column is stable and double-diffusion might occur after exceeding a critical threshold. A negative N^2 yields an unstable water column. For the application in deep water columns, the temperature gradient is usually amended with the adiabatic temperature gradient (Schmid et al., 2004).

Although the major advances in the field of double-diffusion have been made in oceanic sciences, examples of applications on smaller scales are abundant: deep lakes (Schmid et al., 2003; Arnon et al., 2014a), boreholes (Berthold and Börner, 2008), and solar ponds (Cathcart and Wheaton, 1987; Suárez et al., 2010b). A solar pond is a shallow pond that adsorbs heat from solar radiation in its bottom hypersaline layer, where it is stored due to a system of double-diffusive convection (Suárez et al., 2011).

For boil seepage in polder drainage canals, the local thermohaline structure depends on the state of the surface water body and on the inflow properties. The almost constant groundwater temperature is usually warmer than the surface water during winter and colder during summer. Similarly, diurnal fluctuations in the surface water temperature can influence the temperature gradient (Fig. 1.4). In almost all cases, the inflowing seepage water has a higher salinity than the fresh surface water. However, examples of boils which are fresher than the surface water are known (Hilgersom et al., 2016c).

1.5 Research questions

The presented state of the art forms the basis of this research. Previous studies that quantified boil seepage often took a *groundwater perspective*. For example, De Louw et al. (2013) applied an idealized upconing model for saline boil seepage water, and De Louw et al. (2010) measured lateral variations of vertical soil temperature profiles in and around boil locations to quantify the boil seepage flux. End-member analyses (e.g., Delsman et al., 2013) take a more general perspective, which allows a quantification of the boil seepage contribution on a more general (polder catchment) scale. Due to the unstable nature of individual boils and their non-straight vertical paths, this research chooses a *surface water perspective*

1

to quantify boil seepage. This change of scope is based on the ideas that DTS allows high-resolution measurements of the surface water, which are less invasive, and advances in numerical techniques and computation power allow detailed simulations of salt and heat transport. The aim is to ultimately infer the seepage flux from the model based on the measured temperature profile.

Based on this reasoning, our main research question is defined as follows:

How can we measure and model the boil seepage flux from a surface water perspective?

This question can be subdivided into the following questions:

1. How can we build a measurement set-up that efficiently measures detailed water temperature profiles above a boil?
   This sub-question is introduced to explore the ability of DTS to acquire high-resolution temperature profiles. Chapter 3 discusses the advantages and disadvantages of current enhanced-resolution DTS techniques. Chapter 4 presents a new approach for an enhanced-resolution DTS set-up for high-resolution measurements in three dimensions.

2. How can we develop a numerical model that simulates detailed density-driven flow and transport without a computationally expensive 3-D mesh?
   With this sub-question, we aim to find an efficient modelling approach that accurately simulates the 3-D salt and heat transport in double-diffusive systems. Chapter 5 presents the application of a 2-DV free-surface model to an exhaustively measured laboratory-scale solar pond, in order to test the model's capability to simulate double-diffusive convection. Chapter 6 presents a framework to extend the model to a quasi 3-D axisymmetric model, and tests it qualitatively and quantitatively for seepage inflows of contrasting salinity and temperature.

3. To what extent do the detailed measurements and numerical simulations provide similar results for environments of thermohaline stratification?
   Before using the model as an inversion tool, we need to test it for forward modelling results. Chapter 7 compares 3-D temperature measurements above a laboratory boil with model simulations of these temperature profiles.

4. How can modernizations of the rising bubble technique for discharge measurement be further extended to allow application in polder drainage canals where boils occur?
   The axisymmetric modelling approach assumes a negligible stream flow across the boil seep, but the validity of this assumption needs to be tested in the field. Hilgersom (2010) has shown the potential of digital image processing techniques to improve the rising bubble technique for the case of an abandoned lock. Chapter 2 explores how these improvements facilitate the measurement technique in a variety of streams. In Chapter 8, we conclude whether the technique is applicable to determine the flow in drainage canals to support the boil flux measurements.

2

How image processing facilitates the rising bubble technique for discharge measurement

In this chapter, we revisit the integrating rising bubble technique as a means of obtaining discharge measurements. Since Sargent (1981, 1982a), the technique has not been applied widely, mainly as a result of practical difficulties. We propose that modern image processing techniques can greatly improve the rising bubble technique. We applied the technique in both a laboratory set-up and a field study, after determining the bubble rising velocity for our nozzles for each specific case study. During our measurements, we captured digital photographs of the bubble envelope at the water surface, each picture being a single measurement of the discharge. The photographs were corrected for lens distortion and reprojected so that accurate distances on water surface level could be obtained. This easy digital procedure resulted in accurate discharge measurements, even when turbulence was involved and the averages of multiple image analyses yielded good results. The study shows that the rising bubble technique can be a preferable discharge gauging technique in some situations. Recent developments in image processing facilitate the method substantially.

2.1 Introduction

A large variety of discharge gauging techniques is applied in the field of hydrological measurements. Each of them performs best under specific stream properties, such as the geometry of the cross-section and turbulence. The *integrating float method*, one of these techniques, best resembles the frequently applied method using a float at the water surface. With the latter method, hydrologists measure stream flow by releasing a float at the water surface and calculating the velocity from its displacement over time. This method is easy and quick but is considered relatively inaccurate, for an uncertain correction factor is applied to estimate the depth-averaged velocity from the measured surface velocity.

To overcome this, the integrating float method has been developed (Herschy, 1978, 1995), where a float is released at the bottom of a river or canal. The float is assumed to rise with a constant velocity, so the depth-integrated horizontal velocity can be determined from the float's displacement as it surfaces. Air bubbles are a type of float that can be applied in a simple manner. This chapter discusses the merit of modern computational and photogrammetric techniques for applying the integrating float method and specifically the *rising bubble technique* to measure river discharge (Sargent, 1981; Shaw, 1994).

Already in the 19th century, D'Auria described a method in which a sinker was released at water surface level to determine the depth-integrated velocity by the total horizontal displacement of the sinker as it reaches the river bed (Sargent, 1981). At the start of the twentieth century, Hajos (1904) described the reverse procedure: floats are released at the stream bed and their displacement can be found when reaching the surface. Amongst others, Liu and Morris (1970) improved this method and investigated the influence of turbulence on the method.

Viol and Semenov (1964) were the first to apply this integrating float method using air bubbles as floats, assuming these air bubbles have a constant rising velocity. Their work formed the basis for research by Sargent (1981, 1982a,b), who applied two photo cameras with autowinders to obtain a time series of photographs of surfacing air bubbles. The horizontal displacements of the air bubbles with respect to their release points on the river bed could then be calculated from the two pictures taken from different angles using a standard photogrammetric technique. Repeating the procedure provided an easy means to register how stream discharge evolves over time (Sargent, 1981, 1982a). Sargent's work meant a large advance with respect to applicability and accuracy of the method. However, since Sargent's publications, the method has only been applied by a few authors (Toop et al., 1997; Yannopoulos et al., 2008), suggesting that previous technologies made the method less practical and more expensive compared to other gauging methods. A discussion of Sargent's work came to the same conclusion (Sargent and Davis, 1981). We believe that modern technologies can significantly improve the rising bubble technique.

To address the potential of the rising bubble technique as a modern and usable method, we introduce the application of image processing techniques. With this novel approach, we obtain quantitative data from photographs that were taken during tests in a laboratory flume, and case studies in the channelized river Reitdiep

(The Netherlands) and the river Sûre (Grand Duchy of Luxembourg). We demonstrate that the use of a single photo or video camera is sufficient to perform accurate measurements and that automation of the process provides the opportunity to perform continuous measurements with this gauging technique. Measurement results from the case study show that the method performs accurately in the specific situations.

Rather than a manual on measuring with the rising bubble technique, the aim of this publication is to show how the addition of digital image processing techniques supports the method.

2.2 Study site

We tested the rising bubble technique both in a laboratory flume and in the field. The field study consisted of measurements in two distinct situations: a lock with a rectangular cross-section and and a natural stream with a more variable cross-section.

2.2.1 Lock measurements

The first field study was performed in the Provinciale Sluis (53°20′14″ N, 6°17′50″ E), a lock near the village of Zoutkamp (province of Groningen, the Netherlands), on 9 October 2009. This 9-metre-wide lock is constructed on the point where the channelized river Reitdiep enters the Lauwersmeer (Fig. 2.1). At the time that this lake was still part of the Wadden Sea, the lock allowed ships to transfer between the tidally influenced sea level and the controlled water level of the Reitdiep. Since the Lauwersmeer was dammed in 1969, the lock is no longer required. Nevertheless, its rectangular cross-section makes the lock suitable to accurately perform automatic discharge measurements. For this reason, the lock is equipped with an acoustic discharge measurement device (ADM). Both the availability of data from the ADM and the lock's geometry make this site suitable for first testing the rising bubble technique. Besides, the bridge above the lock makes it possible for us to take photographs from above the water surface.

The Lauwersmeer discharges into the Wadden Sea during low tide at sea by means of the R. J. Cleveringsluizen. Opening these sluices strongly enhances the discharge of the Reitdiep near Zoutkamp. To apply the rising bubble technique at varying stream discharges, the R. J. Cleveringsluizen were opened during part of our field measurements.

2.2.2 Natural stream measurements

We studied the technique's performance for a natural stream in the Sûre River (Grand Duchy of Luxembourg) on 10 May 2011. The study site is located between the villages of Boulaide and Bigonville, upstream from the lake Lac de la Haute-Sûre (location: 49°51′58″ N, 5°48′22″ E). Locally, the river is 12.5 m wide and has a natural bed that is shallow on the right half and deeper on the left (facing downstream).

Figure 2.1: Map of the Lauwersmeer; the dark grey lines represent the surrounding embankment.

2.3 Materials and methods

2.3.1 Method

The principle of the integrating float method is that the time T needed for a float to surface with v_z equals the time needed for the float to displace over distance L with a depth-averaged horizontal velocity $\overline{v_x}$ (see Fig. 2.2):

$$T = \frac{D}{v_z} = \frac{L}{\overline{v_x}},$$

(2.1)

where D denotes the vertical distance between streambed and water surface. From Eq. (2.1), we find for the specific discharge q (i.e., the depth-integrated horizontal velocity):

$$q = \int_0^D v_x dz = \overline{v_x} \cdot D = v_z \cdot L,$$

(2.2)

as is described by Sargent (1982a). Eq. (2.2) shows that the specific discharge can be calculated from the constant v_z and the displacement of the float while surfacing (L). The latter parameter varies over the width of the stream (y-direction), and several floats are needed to determine $L(y)$. Integrating the measured displacements

Longitudinal cross-section
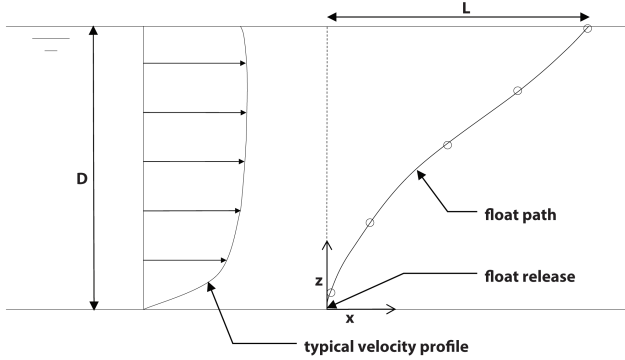
Figure 2.2: Float path occurring with a typical velocity profile over depth.

Top view
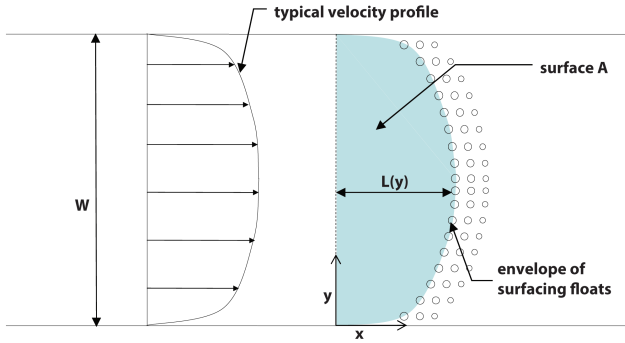
Figure 2.3: Surface A between the float release line and the envelope of surfacing floats.

leads to the total discharge Q:

$$Q = \int_0^W q\,dy = v_z \cdot \int_0^W L(y)\,dy = v_z \cdot A, \qquad (2.3)$$

A being the surface of the bubble envelope (see Fig. 2.3).

2.3.2 Application

For the rising bubble technique, air bubbles are the specific floats. Air bubbles are easier to release from the bottom of the stream compared to other, rigid floats. Furthermore, they make the performance of a series of measurements less complicated.

Air bubbles usually appear at the surface as air bubble clusters. In those cases, the surfacing locations of the bubbles are best indicated by the center of the visible rings on these spots. After surfacing, air bubbles remain visible while continuing with the flow. This leaves traces of air bubbles on the water surface, like are shown

Figure 2.4: Side view of the measurements in the laboratory flume; $L1$ represents the horizontal displacement of bubbles originating from the nozzle located near the flume's wall, $L2$ of the ones from the nozzle located in the middle.

in Fig. 2.3. Of interest for this method are the air bubbles, or the centers of air bubble clusters, that are the closest to the release points.

We first tested the method in a laboratory flume. We used two nozzles to release the air bubbles, one nozzle being located near the wall of the flume and one in the middle (see Fig. 2.4). They were connected to compressed air by small tubes and a pressure regulator controlled the air pressure to just above the water pressure at the bottom of the flume. The nozzles were short steel pipes (diameter: 22 mm) with a 1 mm-wide hole punched into the wall and a click connector on one side of the pipe for the entering air tube. The steel pipes were thickened around the hole to a thickness of 5.6 mm to produce more consistently sized air bubbles (this effect of thicker walls was found in a laboratory test).

We assumed that the horizontal flow profile is symmetrical. We registered the displacements of the air bubbles both by a digital photo camera (Nikon D60; lens: Nikkor AF-S 18–55 mm f/3.5–5.6 G ED DX – this combination was used in all the case studies) and measuring tape, the latter being a reference for the accuracy of the displacements according to the processed photographs. Later, we will describe how the photographs were processed. We compared the discharges found from the photos with data from an Endress+Hauser Prosonic Flow 91W acoustic flow meter that was mounted to the entering pipe of the flume.

In our field study in the lock near Zoutkamp, we chose to lay a steel pipe (diameter: 22 mm) across the stream. The reason for this is that the lock had a flat
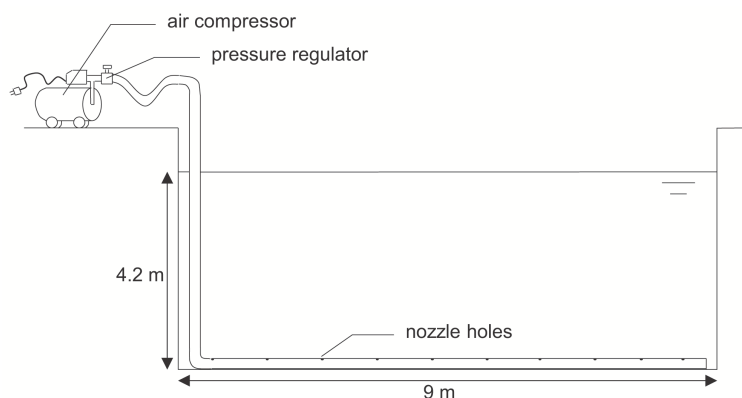
Figure 2.5: Situation sketch for the measurements in the lock near Zoutkamp.

floor and the flow might unequally displace separate nozzles (which would not be noticed from the top of the water surface). The pipe had holes with a diameter of 1 mm every 75 cm to release small air bubbles. In this case, the pipe was not thickened around the nozzle hole, as was done in the other situations.

One end of the pipe was connected to an air compressor via a corner piece and a standing pipe. We chose this construction, since the standing pipe held the horizontal pipe in upright position (i.e., the holes remained facing upward). We adjusted the air pressure in the pipe to just above the water pressure at the bottom of the stream. Fig. 2.5 shows a schematic overview of the measurement set-up. On locations where no electrical power is available, a cylinder of compressed air can replace the air compressor.

We registered the displacement of the air bubbles with a digital camera from a bridge that is more than 4 metres above the water surface. We made sure we captured the location of the pipe, the bubble envelope, and four reference points that were needed for the image processing all in one image. From the processed images, we could find the discharges over time and compare them with reference measurements from the acoustic discharge measurement device located in the lock (Elster Instromet, FLOW-2000 model 5; the device uses the travel times of acoustic signals between two pairs of transducers to calculate the longitudinal and transversal velocity in the stream at one representative depth). In addition, we took a reference measurement with a propeller current meter (Valeport, Model BFM002) at three depths for three verticals in the cross-section.

In the Sûre River, the use of a steel pipe was made impossible by the varying depth of the river bed. We chose to place five nozzles on the bed of the same type as applied in the laboratory flume. They were connected to a cylinder of compressed air by small tubes (no electricity was available at this site), two of the nozzles being located on the shallow side of the cross-section (ca. 30 cm deep) and the other three in the deeper part (ca. 60 cm deep). Three pressure regulators controlled the air pressure to just above the water pressure at bed level. An attached tile

prevented the nozzles from floating and kept the hole facing upwards.

We used a step ladder on one bank of the river to take photos from a sufficient level above the water surface. Four traffic cones with measured relative distances, two on each bank, marked our reference points. Ideally, the bases of these traffic cones would have been on water surface level. In this case, we placed two of the traffic cones a bit higher due to the local shape of the banks. Estimating the locations of these cones as if they were on water surface level might have introduced an additional small error for this case study. Again, the pictures were taken so that all the reference points and the complete bubble envelope were captured. A measurement with a propeller current meter (SEBA-Mini Current Meter M1, propeller serial no. 250257; the measurements were performed in six verticals and at three depths) constituted our reference measurement.

2.3.3 Image processing

The novelty of this research consists for a large part of applying digital image processing to the integrating float method. The following will describe the subsequent steps to obtain area A from a digital photograph. We performed the processing using the Image Processing Toolbox of Matlab®, because the toolbox provides part of the tools we need and the Matlab scripting makes the process easy to repeat.

The photograph must fully capture the bubble profile and the reference points, and surfacing bubbles must be visible (both in terms of size on the picture and light circumstances). The reference points are used to transform the image to a 2-D projection. They should be on the water surface level and have known relative distances.

A photo camera lens usually deforms photographs due to a varying shape and an imperfect centering, meaning that photos cannot be used straightaway. This is called optical aberration and affects the photograph by radial and tangential distortion (Brown, 1966). Tangential distortion, caused by imperfect centering of lenses, is negligible in contemporary cameras (Tsai, 1987; Nowakowski and Skarbek, 2007). Therefore, we will correct our images for radial distortion (i.e., the displacement of pixels into radial direction from the center of distortion).

Radial distortion appears mainly in the form of barrel or pincushion distortion (De Villiers et al., 2008; Neale et al., 2011). In the former, the image looks bulged, and in the latter it looks squeezed. In most cases however, camera lenses appropriate for this method will cause barrel distortion.

The radial symmetric nature of barrel distortion makes it easy to correct a picture for this distortion, as is often done in the practices of architectural photography and 3-D computer vision, where camera lenses bend for example the straight lines of buildings (Devernay and Faugeras, 1995, 2001; Stein, 1997; Swaminathan and Nayar, 2000), and in photogrammetry. The latter is the practice of determining the geometric properties of objects in pictures and is the major concern of this research. A simple algorithm for correcting for barrel distortion (i.e., for squeezing the "bulged" photo back) is based on the following equation (Brown, 1971; Fryer and Brown, 1986):

$$r_u = r_d + k_1 \cdot r_d^3 + k_2 \cdot r_d^5 + k_3 \cdot r_d^7 + ..., \tag{2.4}$$
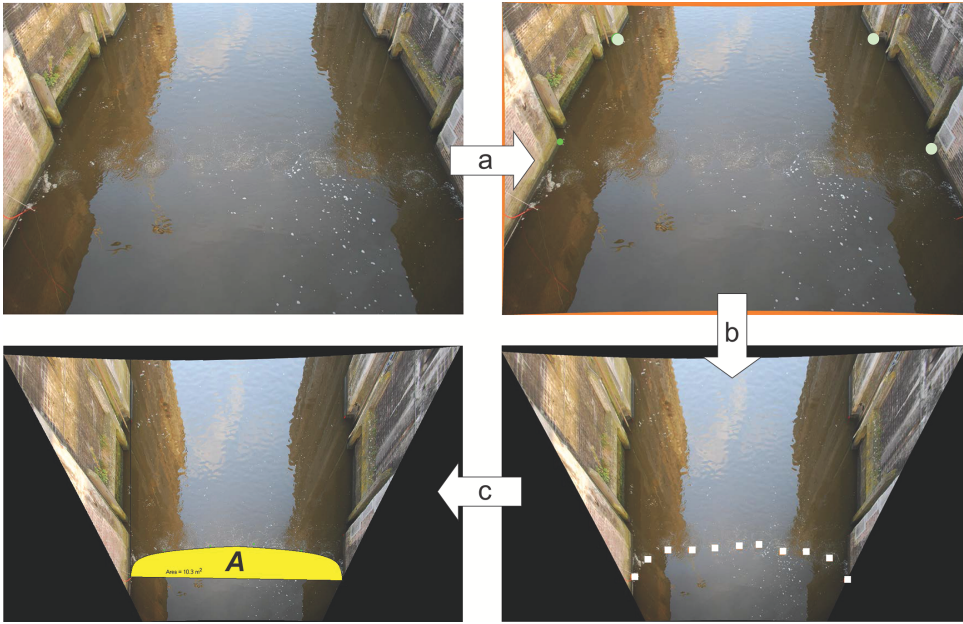
Figure 2.6: Steps performed to process the image and obtain surface area A; step **(a)** represents the correction for lens distortion, step **(b)** represents the 2-D reprojection of the image based on the four reference points on a horizontal plane (the light green circles), and step **(c)** finds the area in between the nozzle line and the bubble envelope (the white squares).

where r_u and r_d are the radii for each pixel relative to the center of distortion (normalized to the maximum radius at the corners) for the undistorted and the distorted picture, respectively. Since we may assume that barrel or pincushion distortion constitutes most of the lens' radial distortion, the third order term is predominant in Eq. (2.4) (Brown, 1971), and allows us to rewrite the equation:

$$r_u = r_d + k_1 \cdot r_d^3. \tag{2.5}$$

The constant k_1 is lens-specific and is often provided by manufacturers or specialized websites, but one can also calibrate it oneself.

The procedure maps input pixels from their original locations (denoted by integer coordinates) to new coordinates that are unlikely to have integer coordinates. The subsequent resampling of output pixels leads to minor information losses (De Villiers et al., 2008). Step a in Fig. 2.6 represents the correction for lens distortion.

Afterwards, we morph the images to a horizontal (2-D) plane at the water surface level, using the four selected reference points. Theory about this technique follows from literature about Digital Image Warping, a subfield of Digital Image Processing (Wolberg et al., 1990). There are several software packages that support the projective warping of images. We use Matlab's Image Processing Toolbox to set up a transformation array on which we map our photograph.

A projective transformation of a quadrilateral to a quadrilateral requires four

reference points which should in our case be located on the level of the water surface, since that is the plane from which we want to obtain distances. The four reference points are not required to be the corners of a rectangle. The result of the transformation shows large distortion of objects outside this plane as shown by step b (Fig. 2.6). Within the plane, on the other hand, a 2-D image of the water surface correctly represents the distances.

Like in step a, the resampling of output pixels in step b causes minor information losses, resulting in a possible deterioration of the visibility of surfacing air bubbles as the photograph passes through steps a and b. Since step c determines the bubble envelope based on the locations of the bubbles, we choose to mark the points of interest (i.e., the locations of the air bubbles and the nozzle line) in the unprocessed photograph, and recalculate their positions as the photograph passes through the first two steps.

Step c in Fig. 2.6 interpolates the area between the nozzle line and the bubble envelope. Since Matlab used the known relative distances of the reference points when recalculating the locations of the release pipe and the air bubbles at the water surface, these locations are properly georeferenced. From this it is an easy step to calculate the area enclosed between the nozzle line on the river bed and the bubble envelope at the water surface and, subsequently, the discharge according to Eq. (2.3).

When the stream cross-section is rectangular and the flow direction is approximately perpendicular to the cross-section, as is the case in the lock near Zoutkamp and in the flume, it is sound to assume a logarithmic shape of the transversal profile of flow velocities. Therefore, we interpolate the surfacing bubbles in the lock and the flume with a logarithm, whereas for the natural river a linear interpolation is applied.

2.3.4 Rising velocity

The rising bubble technique assumes a constant rising velocity v_z of the air bubble that is released at the bottom of the stream. However, this assumption does not represent reality in every case. Several authors (e.g., Sargent, 1982b; Toop et al., 1997; Yannopoulos et al., 2008) have shown that applying this assumption depends on the air pressure, the size of the nozzle from which the air bubble is released, and water properties like turbulence, temperature and contamination. More detailed research on the motion of gas bubbles in a liquid has been performed by, amongst others, Aybers and Tapucu (1969a,b) and Lehrer (1980). These publications teach us that, for a certain range of air bubble diameters, the rising velocity does not change much with varying diameters. This means that proper air bubbles for the rising bubble technique should have sizes within this range of approximately 2 to 4 mm, depending on the circumstances. Bubbles with these sizes have commonly an ellipsoidal shape (e.g., Wesselingh, 1987).

Before our discharge measurements, we conducted laboratory tests to investigate the rising velocity for several nozzle sizes and air pressures. The tests were conducted inside a transparent, 2-metre-high column (diameter: 30 cm) and compared the bubbles resulting from varying nozzle diameters, water levels and air

pressures. From the results, we determined the nozzle design for our study.

Since water properties appeared to influence the rising velocity, we used a similar but smaller column in the field to measure this velocity for the specific situation. The column was filled to a level of 1.5 m to have enough distance to do accurate velocity measurements, based on the time that tracked air bubbles needed to pass through a distance of 1 m. Since the size of the nozzles was determined so that depth effects to the rising velocity appeared minimal, we assumed the measured velocity to hold for other water depths as well. In the case of the flume measurements, we measured the rising velocity of the air bubbles both in the flume and the 1.5-metre column.

As an alternative, one could use an underwater camera to measure the rising velocity of the air bubbles in-stream. This method would prevent that convective flows and changing water temperatures in the column affect the rising velocity of the air bubbles, but was not applied in the field studies described in this chapter.

2.4 Results and discussion

2.4.1 Rising velocity

From our laboratory measurements of the rising velocity, we concluded that a nozzle opening of 1 mm in diameter together with an air pressure just above the water pressure around the nozzle produced air bubbles that are most likely within the range of 2 to 4 mm. Within this range, air bubbles are commonly ellipsoidal and remain almost constant in vertical velocity while surfacing (e.g., Wesselingh, 1987). However, since the main focus of our research is the applicability of image processing techniques, further research is required to design a nozzle that produces air bubbles with consistent rising velocities.

We also found that a field determination of the rising velocity is currently still necessary to get a good estimate. For our discharge measurements in the laboratory flume, we observed both in the flume itself and in the column that v_z was 0.23 m s^{-1}, whereas for our field studies in the lock and in the river Sûre v_z was 0.35 m s^{-1} and 0.32 m s^{-1}, respectively. These differences can be attributed to different air pressures, water temperatures and contamination, as well as a minor change in nozzle design (a thickening of the wall of the steel pipe). We recommend further research on these influencing factors to better predict the rising velocity, given the governing circumstances. In the following, we use the rising velocities that we determined on site.

2.4.2 Flume measurements

We first applied the method in a laboratory flume. Table 2.1 shows that the rising bubble technique gave accurate results in the laboratory situation, measuring on average 47.1 l s^{-1} by photo integration as compared to 46.6 l s^{-1} measured by an acoustic flow meter in the entering pipe of the flume. Variations in the discharges measured, as illustrated by the variations in the distances $L1$ and $L2$ (see Fig. 2.4) as well as the average percentage deviation of five rising bubble technique measurements relative to their average value, can be attributed to the turbulent nature

Table 2.1: Discharges measured with the photogrammetric technique in a laboratory flume with a constant discharge; the absolute deviations are relative to the average discharge measured with the rising bubble technique; as a reference, hand measurements of the distances $L1$ and $L2$ (see Fig. 2.4) measured on average 25 cm and 27 cm, respectively.

Measurement	$L1$ (cm)	$L2$ (cm)	Q (ls^{-1})	Deviation
1	24.6	26.9	48.1	2.08 %
2	23.8	29.7	47.4	0.59 %
3	23.8	28.0	45.6	3.23 %
4	27.2	25.1	48.5	2.93 %
5	24.3	26.3	46.0	2.38 %
Average	24.7	27.2	47.1	2.24 %

of the flow inside the flume. However, as the number of samples was increased by analysing more photographs, the rising bubble technique provided consistent results.

2.4.3 Lock measurements

Data from the field study was obtained during a field study on 9 October 2009. During low tide in the Wadden Sea, the R. J. Cleveringsluizen were opened to vary the discharge in the Provinciale Sluis. This strongly influenced the bubble envelope at the water surface (see Fig. 2.7). Fig. 2.8 compares the results we obtained from the rising bubble technique with the time series from the acoustic discharge measurement device. We performed one propeller current meter measurement as a reference. Since this method requires measurement of velocities at several locations across the cross-section, this is the most labor intensive of the three methods and was, therefore, performed only once. The transient flow makes the moment of performing the propeller current measurements rather unfortunate.

From our observations, the measurement error of the rising bubble technique compared to the acoustic discharge measurements appears on average about 13 % at low discharges, whereas at higher discharges the measurement error reduces to 3 % (see Table 2.2). We argue that the relative error at lower discharges is larger, since the relative error in determining the distance that a bubble travels (r_L) is large when this distance L is low compared to the measurement error ΔL ($r_L = \Delta L/L$).

2.4.4 Natural stream measurements

Table 2.3 shows the results for the natural river Sûre on 10 May 2011. The photos were taken on average every 10 s. The low percentage errors show that the analysis of multiple photographs can lead to consistent results, even in this environment and with this limited amount of five nozzles.

In photo 5, two of the surfacing bubble clusters were poorly visible, which may account for the relatively large deviation from the average of over 4 %. The poor visibility of surfacing air bubbles is both due to shading effects on the water surface (e.g., compare the visibility of the left and right surfacing location marked in
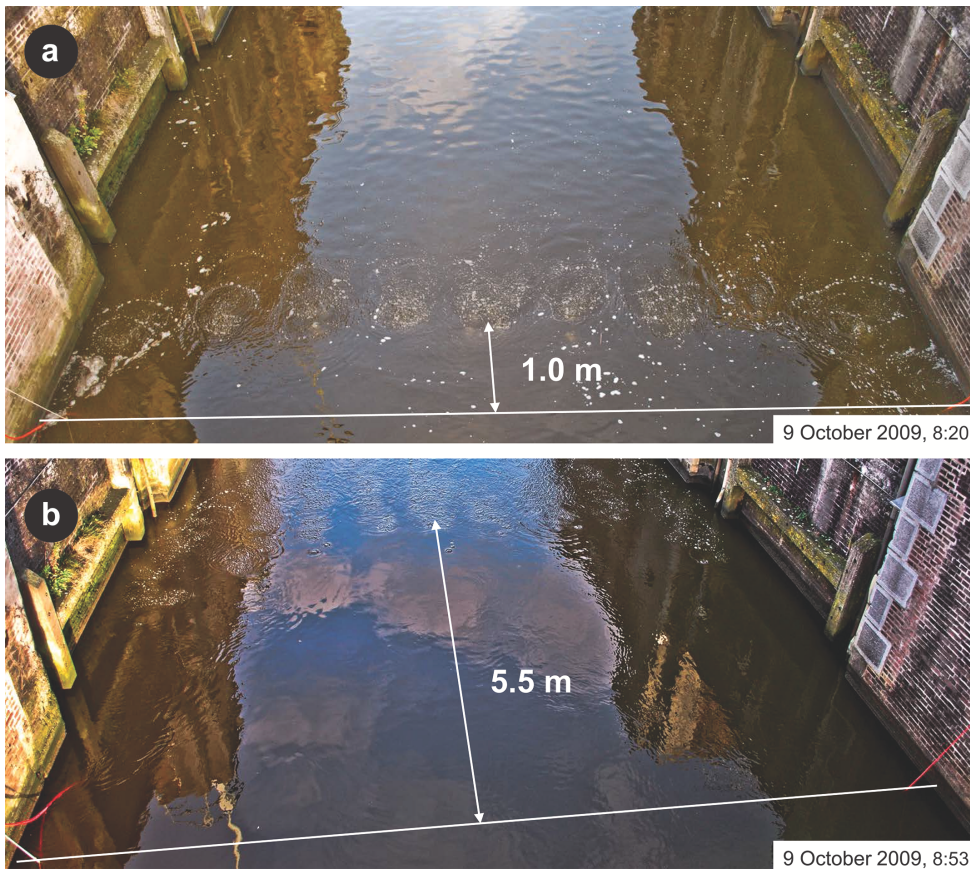
Figure 2.7: The bubble envelope during low ($3.3\,\mathrm{m}^3\,\mathrm{s}^{-1}$) and high ($16\,\mathrm{m}^3\,\mathrm{s}^{-1}$) discharge, respectively.

Fig. 2.9a) and the low resolution of a zoomed surfacing bubble. The latter cause indicates that, for our type of photo camera, this river size is the maximum that the method can handle. However, a change in the set-up (e.g., by hanging the camera in the middle above the stream) can double the maximum river width for which this method works. A higher-resolution camera can also expand this range.

The discharge found with the propeller current meter was $693\,\mathrm{l\,s}^{-1}$, yielding a deviation of approximately 4 % with respect to the rising bubble technique, which can be caused by both the limitations of the propeller current meter and the rising bubble technique. The irregular river bed can cause an inaccurate calculation of the cross-sectional area by which the propeller current meter measurements are multiplied. For the rising bubble technique, a measurement error in the rising velocity will introduce a systematic error. An error in the rising velocity affects the calculated discharge linearly.

These first results show that the method appears valuable for discharge measurements in certain natural rivers. Further research should go more into detail on

2
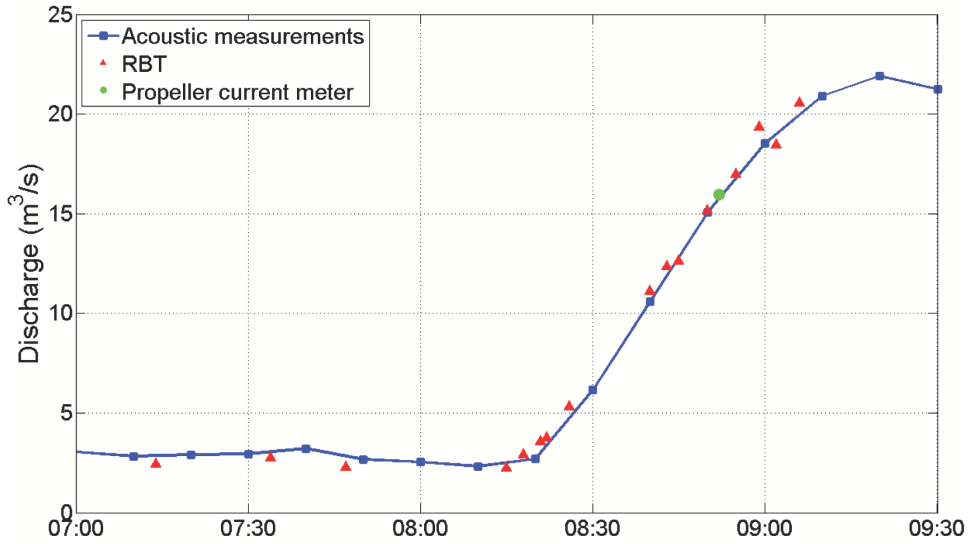
Figure 2.8: Time-series of rising bubble technique (RBT) measurements plotted against acoustic discharge measurements (9 October 2009).

the application under circumstances where turbulence and shallow water depths potentially influence the measurement accuracy.

2.4.5 Measurement errors

Sargent (1982b) gave an elaborate description of the measurement errors involved with the rising bubble technique and Liu and Morris (1970) analysed errors introduced by turbulence. For this reason, we will restrict ourselves to the measurement errors involved with digital image processing.

When transforming a photograph, errors are introduced by (a) information loss due to interpolating pixels, (b) inaccurate marking of the points of interest, and (c) the inaccurate marking of the reference points based on which the image is transformed.

Error source a is caused by the resampling of pixels during the correction for lens distortion and the reprojection to a 2-D image, becoming significant with a large angle between the camera view and the top view to which the image is reprojected. However, we decided to already mark the points of interest before these processes, excluding the need to interpolate pixels before marking the bubbles, since these markings have double instead of integer precision.

Photographing from a high incidence angle and effects of sun and shade influence the visibility of air bubbles on the water surface and the possibility to mark them accurately. The following expands further on this error source b.

Reflecting sunlight may complicate determining the locations where the bubbles surface, as we showed in Fig. 2.9a. It is recommendable to select a proper location with respect to sunlight to take photographs. If this is not possible and the sunlight

Table 2.2: Absolute percentage deviations for the discharges (Q) measured with the rising bubble technique (RBT) compared with the acoustic discharge measuring device (ADM) in Zoutkamp (9 October 2009); cross-sectionally averaged velocities $\bar{v}$ lower then $0.2\,\mathrm{m\,s^{-1}}$ are considered low.

Time	$\overline{v_{\mathrm{RBT}}}$ ($\mathrm{m\,s^{-1}}$)	Q_{RBT} ($\mathrm{m^3\,s^{-1}}$)	Q_{ADM} ($\mathrm{m^3\,s^{-1}}$)	Deviation
7:14	0.07	2.4	2.9	14.9%
7:34	0.07	2.8	3.1	9.7%
7:47	0.06	2.3	2.8	19.8%
8:15	0.06	2.2	2.5	11.0%
8:18	0.08	2.9	2.6	10.8%
8:21	0.10	3.6	3.0	17.3%
8:22	0.10	3.8	3.4	11.3%
8:26	0.14	5.3	4.8	11.6%
8:40	0.30	11.1	10.6	4.7%
8:43	0.33	12.3	11.9	3.5%
8:45	0.34	12.6	12.8	1.7%
8:50	0.41	15.1	15.1	0.6%
8:55	0.46	17.0	16.8	1.2%
8:59	0.52	19.3	18.2	6.4%
9:02	0.50	18.5	19.0	2.9%
9:06	0.56	20.5	20.0	2.9%
		Average:	- Low flow velocity:	13.3%
			- High flow velocity:	3.0%

heavily influences the visibility of the points of interest, a decrease in accuracy can be prevented by including a step in the image analysis as shown in Fig. 2.10, where the bubbles are easily observable irrespective of their locations in sun or shade. This step applies a filter to the image that calculates the standard deviation of the colour value of each pixel together with that of its surrounding pixels. Large transitions are represented by a high standard deviation. This way, the resulting picture displays surfacing bubbles with light grey pixels and the transition to the shade with just a line of another colour (in this case blue).

When photographing under a high incidence angle, it becomes difficult to properly mark a location, as a small shift of a mark on the picture means a relatively large shift in the location on the water surface. We expect that this error source b is negligible in our results from the lock, since our photographs were captured from almost straight above the area between nozzle line and bubble envelope. The photographs of the river Sûre were taken from a larger angle, causing a larger source of random errors due to the possibly inaccurate marking of surfacing bubbles, nozzle line and reference points. The consistent results for the different photos suggest that even in the Sûre River case this error source was relatively small, although they are based on a limited amount of measurements. Apparently, taking photographs from moderate incidence angles is already sufficient to mitigate significant effects from this error source.

Error source c can play a role with an unsuitable configuration of the reference

Table 2.3: Discharges measured in the river Sûre (10 May 2011); the absolute deviations are relative to the average discharge measured with the rising bubble technique.

Photo	Q (ls^{-1})	Deviation
1	665	0.00 %
2	666	0.15 %
3	676	1.65 %
4	689	3.61 %
5	638	4.06 %
6	653	1.80 %
7	668	0.45 %
Average	665	1.68 %

points, with an inaccurate measurement of the distances between the reference points, or with a poor distinction of the reference points in the image.

In the case studies, the reference points formed quadrilaterals that approximated a rectangular shape with a ratio of sides not larger than three times unity. The reference points were easy to distinct, although an estimation had to be made in the Sûre case for two traffic cones that were a few centimetres above the water level.

In the lock, the relative distances between the reference points were measured with about 4 cm accuracy, yielding a relative error across the enclosed area ($53.6\,\text{m}^2$) that is fairly negligible. For the range of scales suiting this method, we can assume a relative error in distance measurement that remains within the same order of magnitude. For example, for our flume measurements, we could determine the relative distances with an absolute error of two millimetres which is equally negligible to the $0.72\,\text{m}^2$ enclosed by the reference points.

2.4.6 Comparison with other techniques

The main focus of this chapter is showing the value of image processing for the rising bubble technique. We show this for applications under various conditions in both a lock and a natural river. Our results can lead to an estimation of the applicability of the method in various streams, like we have listed in Table 2.4. Note that this table focuses on the *applicability* of the technique and does not focus on whether the method can be *preferable* in this situation (currently, we regard the method not preferable in rivers of more than 30 m in width and in rivers with a depth less than 25 cm).

Aspects like the availability of money and time and the demanded accuracy determine whether a method is preferable. With respect to time consumption, it is quicker to use a Doppler current meter than to install nozzles and measure with the rising bubble technique. However, Doppler current meters are a lot more expensive compared to the equipment needed for the rising bubble technique. Both can be considered as relatively accurate discharge gauging techniques (of course depending on the circumstances).
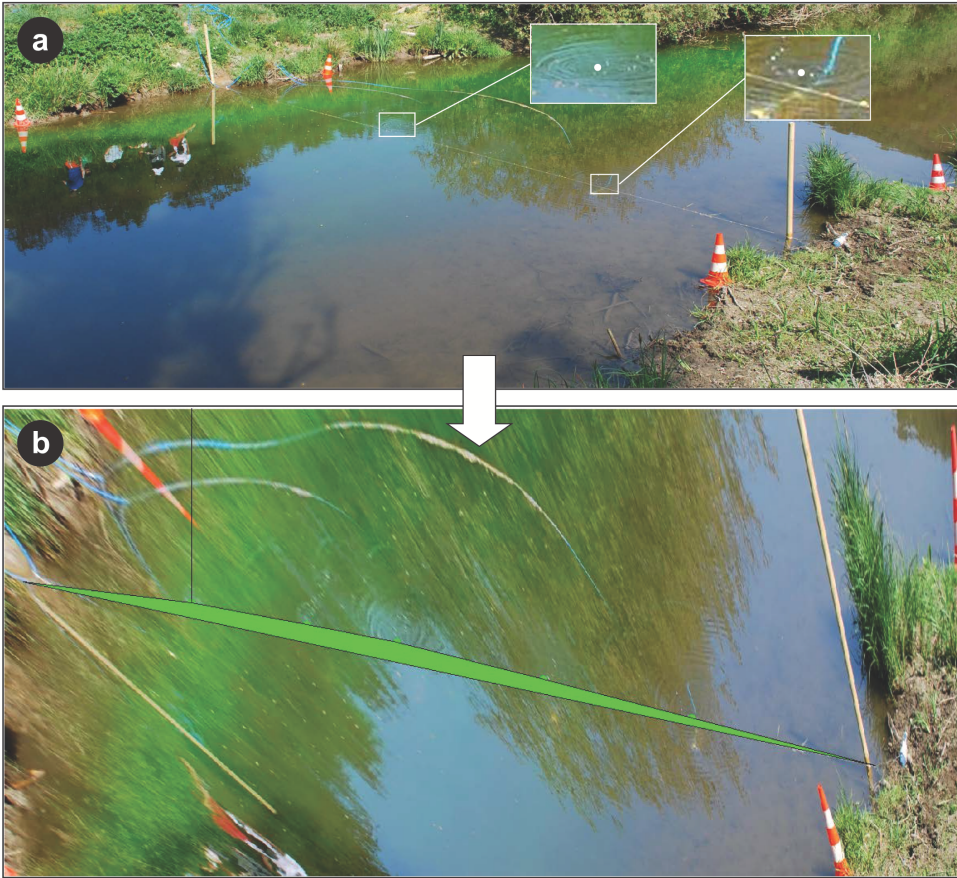
Figure 2.9: Application in the river Sûre; **(a)** shows two examples of marked bubbles, **(b)** shows the final result of the image processing from which the green area A can be obtained.

If we compare the rising bubble technique with a current meter measurement, they compare in terms of initial expense. Of these, the former is more accurate by design (the air bubble integrates the horizontal velocity over the depth and all the verticals across the stream are measured instantaneously). Generally, the rising bubble technique is quicker than measurements with a current meter, certainly when the equipment and reference points are left on site, or when only the air nozzles have to be re-installed. The reason for this is that a propeller or electromagnetic sensor has to be adjusted to the right relative depths in every vertical, which is very time consuming, whereas the rising bubble technique does not even require measurements of river depth.

Figure 2.10: Standard deviations for each pixel's neighbouring area: high-intensity values indicate a large standard deviation of the pixel intensity relative to the neighbouring pixels. The pixel intensities are calculated by converting their colour values to greyscale values.

2.5 Conclusions

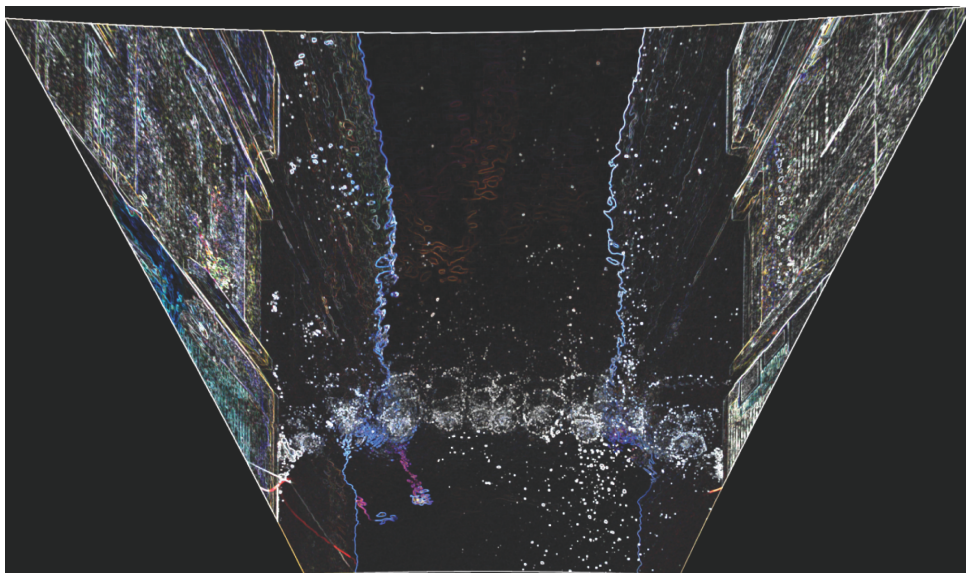Although the integrating float method dates back to the 19th century, its full potential has never been recognized. In the past, the method was improved by Viol and Semenov (1964), who were the first to describe it using air bubbles as floats, and Sargent (1981, 1982a), who researched the practicalities of this technique. However, practical difficulties still impose a threshold for applying the technique. We show that part of these difficulties can currently be removed by applying image processing techniques.

Our results in the lock case study over time correlate well with our reference measurements. The good agreement between both methods appears particularly at higher discharges, as is also expected for this method. For lower discharges, the results deviate from the reference measurements by about 13 %. Further research should clarify how the technique performs under these circumstances. Experiments in a laboratory flume show that this method is very accurate under controlled circumstances. Moreover, the first results from the application of the method in a natural river look promising and show the method's value in a natural environment.

Although the rising bubble technique already appears competitive with other discharge gauging methods, we think that further improvements in the nozzles and research to their effect on the shape of air bubbles, together with other factors like water temperature, depth and contamination, may constitute a significant improvement of the technique. The main motive to search improvement in this part of the method is the linear relation of the rising velocity with the calculated discharge and

Table 2.4: Applicability of the Rising Bubble Technique for various situations (situations in *italics* were actually applied).

Situation	Applicability
Low-order streams (depth: <25 cm)	Inaccurate method, since the low depth causes the horizontal displacement at the surface to be small
Small rivers (width: 2–15 m, depth: >25 cm)	Accurate method (when turbulence is not too high for the bubble plume to be discernable); pictures can be taken from one bank with a normal resolution
Rivers (width: 15–30 m)	Accurate method when pictures are taken with a higher resolution than that of a commercial camera or from above the stream (from a bridge, or if the river is wadeable using equipment in the river)
Rivers (width: >30 m)	Accurate method when taking pictures at several points along the cross-section for which additional reference points are needed; since nozzle installation gets more complicated, application in these situations is of interest with a permanent installation (in the case of a fixed set-up, reference points are only needed during its calibration)
Canals / structures (artificial cross-section)	Accurate method (subject to the same considerations of depth and width as in the above)

2

the uncertainty introduced by the field measurement, which is often not an ideal situation.

We conclude that the method is applicable in relatively deep streams with an average to high flow velocity. At very high velocities, eddies caused by turbulence may affect the bubble paths too much to measure accurately. Apparently, this was not the case for the flow velocities we observed. Our results from the laboratory flume show that the analysis of a series of photographs largely mitigates the negative influence of turbulence. We believe that this is a strength of this method, since modern image processing techniques facilitate the efficient processing of multiple photographs.

Examples of situations in which this technique can be applied are canals and moderate streams. For larger rivers, professionals are required to install the equipment. This is only profitable in cases where discharges are frequently or continuously measured.

The application in the field is simple: once the nozzles are installed, only pictures need to be taken of the water surface, each being a single measurement. This way, one can also capture the development of the discharge over time (as shown in Fig. 2.8).

2.6 Recommendations

In this study, we show that the rising bubble technique can compete with other discharge gauging methods in terms of costs, time consumption and accuracy.

Moreover, we still see opportunities to improve the technique. This section categorizes them in two groups: improvements concerning the production of air bubbles that rise with a constant velocity and the image processing techniques.

First, more research to the proper types of air bubbles offer a large opportunity to improve the technique. The rising velocity follows from the difference between the buoyant force of the bubble and the drag force imposed on the bubble. Since the size of an air bubble increases as it rises to the surface, both forces vary as well. Interestingly, within a certain range of bubble sizes, the remainder of the forces is nearly constant, and the rising velocity hardly changes. From Lehrer (1980), Wesselingh (1987), and Janssen and Warmoeskerken (1997), we find that this range is dependent on the contamination of the water, but the limits are roughly 2 and 4 mm. When we are able to produce air bubbles that initially have sizes in the lower end of this range, the velocity will remain nearly constant as they expand while surfacing. To this end, we think that more research to the type of nozzle and the type of gas can improve the method.

Since we found that the bubbles' rising velocity during our field study differed significantly from our lab experiments, more information is needed on the influence of factors that possibly play a role here, like water temperature and contamination. More research into these influences will help to improve the accuracy of the method. When the influence appears unpredictable, we argue that a field measurement of the rising velocity for the governing circumstances will still lead to proper measurement results.

Second, the novel direction that we choose with respect to image processing offers opportunities for further improvement. The statistical procedure applied in Fig. 2.10 can also help automate the complete process of obtaining a discharge from a photograph. As the figure shows, patterns are easily recognizable and current pattern recognition techniques allow us to find these patterns automatically. Using pattern recognition techniques to completely automate the process requires further research.

Following from these recommendations, the rising bubble technique has the potential to become a good alternative for discharge measurement techniques in moderate rivers and canals.

3

Practical considerations for enhanced-resolution coil-wrapped distributed temperature sensing

Fibre-optic distributed temperature sensing (DTS) is widely applied in Earth sciences. Many applications require a spatial resolution higher than that provided by the DTS instrument. Measurements at these higher resolutions can be achieved with a fibre-optic cable helically wrapped on a cylinder. The effect of the probe construction, such as its material, shape, and diameter, on the performance has been poorly understood. In this chapter, we study a data set obtained from a laboratory experiment using different cable and construction diameters. This study shows that the shape, diameter, and cable attachment method can have a significant influence on DTS temperature measurements. We present a qualitative approximation of errors introduced through the choice of coil diameter and cable attachment method. Our results provide insight into factors that influence DTS measurements, and we present a number of solutions to minimize these errors. These practical considerations allow designers of future DTS measurement set-ups to improve their environmental temperature measurements.

3.1 Introduction

I n recent years, distributed temperature sensing (DTS) has been widely used for high-resolution temperature measurements in environmental sciences. While DTS instruments continue to provide ever-increasing spatial and temporal resolution, there are many cases in which the spatial resolution is yet insufficient to address measurement requirements. Fortunately, a fibre optic cable can easily be wrapped to a coil. This makes DTS a very suitable technique to obtain dense temperature data along the axis perpendicular to the wrapping.

Numerous studies have applied DTS for temperature measurements with high spatial and temporal resolutions in hydrological and atmospheric systems, such as soils (e.g., Steele-Dunne et al., 2010; Jansen et al., 2011; Ciocca et al., 2012), streams (e.g., Selker et al., 2006a; Vogt et al., 2010; Westhoff et al., 2007, 2011), lakes (e.g., Vercauteren et al., 2011; Van Emmerik et al., 2013), and in the air (e.g., Thomas et al., 2012; Euser et al., 2014; De Jong et al., 2015).

In some cases, very high spatial resolutions are required to give insight into hydrologic or atmospheric systems. Various authors (e.g., Selker et al., 2006a; Vogt et al., 2010; Suárez et al., 2011; Vercauteren et al., 2011) have increased the vertical spatial resolution of DTS measurements by wrapping fibre-optic cable around a solid PVC tube, a technique sometimes called high-resolution DTS (HR-DTS), yielding spatial resolutions between 4 and 11 mm. The downside of this approach is that stress on the fibre or the characteristics of the supporting materials such as PVC (polyvinyl chloride) tubes (in this thesis: *auxiliary constructions*) might also influence the temperature measurements.

It has generally been assumed that the characteristics of the measurement set-up, such as DTS cable diameter, coil diameter, auxiliary construction material, and coil preparation, do not influence the temperature measurements (e.g., Vercauteren et al., 2011; Van Emmerik et al., 2013). However, recent papers discuss several errors in DTS temperature measurements caused by practical considerations of the measurement set-up. Arnon et al. (2014b) described a signal loss and consequent error in their temperature measurements along a helically wound cable. This loss was mostly visible in the first 100 m of cable and dissipated later on. They hypothesized that the curvature attenuates some of the most extreme modes of light. Further along the cable, the effect on the temperature disappeared.

Others have signalized the effect of heat conduction between a DTS cable and bedding material in streams (O'Donnell Meininger and Selker, 2015), and inaccuracies in air and water temperatures due to solar radiation (Neilson et al., 2010; De Jong et al., 2015). Hilgersom et al. (2016d) studies how solar radiation on auxiliary constructions deteriorates the measurement accuracy in a similar fashion. This important effect will be ignored in the remainder of this chapter.

This chapter demonstrates the relationship between coil diameter, signal loss and temperature measurement error for specific fibre-optic cables. With this, we aim to better relate the signal loss shown by Arnon et al. (2014b) to coil diameter and fibre type, specifically, bend tolerance.

Using DTS air temperature data sets obtained during a laboratory study, the influence of coil diameter and coil preparation is evaluated. The aim is to provide

practical insights into the effects of coil preparation, diameter, and auxiliary construction, and propose some potential improvements to mitigate negative effects, which allows users of DTS to improve their measurement set-ups.

3.2 Methods and materials

One of the practical issues in applying coil-wrapped DTS is selecting the appropriate size of the coil. In general, with a sufficiently large diameter (over 0.1 m), the optical behaviour of the optical fibre is not influenced by bending, and performance is equal to that found in a straight cable. In some installations, there is no restricting upper limit for the diameter of the coil, so use of such large diameter is feasible. For example, the environment of the installation offers sufficient space and the temperature barely varies in lateral direction from the HR-DTS pole, such as in a lake (Vercauteren et al., 2011) or on an open field (Euser et al., 2014). In these cases, the required coil resolution and the machine resolution determine the diameter of the coil, and there is usually no need to apply a coil with a very small diameter.

However, often there is a spatial limitation in lateral direction, for example, in the case of a narrow borehole (Vogt et al., 2012), or in case of strong lateral temperature variations at the 0.1 m scale. In these cases, the size of the coil diameter is restricted to often less than 0.05 m, in which case bend-related differential attenuation of the Stokes and anti-Stokes backscatter is to be expected. The minimum coil diameter is determined by (1) the required coil resolution, and (2) the maximum allowable signal loss by the bent fibre. The required coil resolution is dependent on the coil width and the machine resolution. In this chapter, we focus on the effects of narrow cable bends on signal loss, which might cause temperature defects.

First, the signal decay is increasing with decreasing bending radius. This *attenuation* follows from the larger fraction of the laser signal that exceeds the angle of acceptance for which light is mainly reflected from the fibre wall (Fig. 3.1, light modes b and c). A low number of remaining light modes leaves larger relative errors in the Stokes over anti-Stokes ratio, reducing the signal strength and consequently the accuracy of the temperature measurements.

Second, the altered *differential attenuation* directly affects the temperature measurements. Arnon et al. (2014b) found that a laser signal entering a coil at first experiences relatively large rates of differential attenuation in the first 100 m of fibre, then asymptotically returning to constant rates of attenuation as the signal passed this distance. In their set-up, the coil was of 20 mm in diameter. This outcome was hypothesized to be due to the preferential loss of the most extreme modes of light in the anti-Stokes (shorter wavelength) compared to Stokes frequency.

The refractive index of light in a glass fibre is dependent on wavelength according to the Sellmeier equation. Therefore, a laser signal with a lower wavelength (anti-Stokes) has a larger angle of acceptance for internal reflection. The Stokes-scattered light modes returning through the glass fibre usually outnumber the anti-Stokes modes. Consequently, a high number of Stokes modes travel through the fibre before entering a bend. At the same time, the Stokes modes reflect from
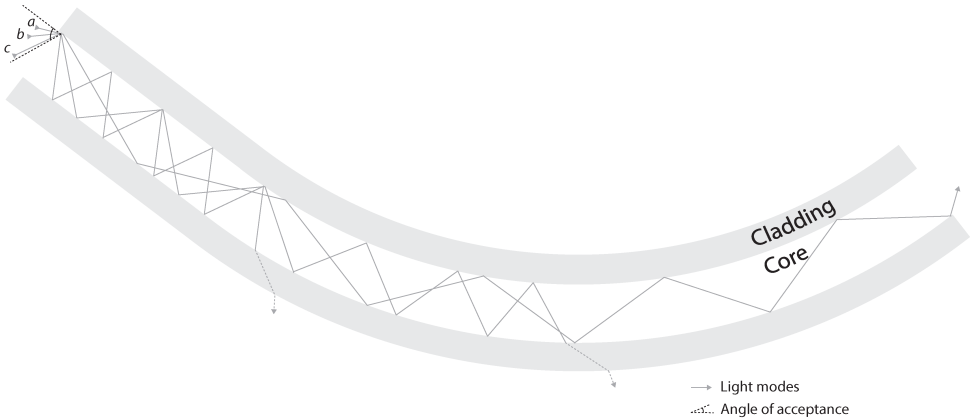
Figure 3.1: Three modes of backscattered light in a bent fibre. Mode a has a non-critical angle of incidence, and remains in the core of the fibre. Mode b falls below the angle of acceptance at a certain point in the bend. Mode c falls below the angle of acceptance as soon as it reaches the bend. Modes with a lower angle of incidence than mode c are lost as soon as they enter the cable. Each angle is more acute for the higher frequency anti-Stokes backscatter, leading to a greater loss of these photons than the Stokes photons, resulting in a spatially distributed differential attenuation spanning 100 m of fibre.

the fibre wall with a relatively small angle due to the smaller acceptance angle for internal reflection. Due to the added angular change of the fibre at the entrance of a cable bend, a relatively high number of Stokes light modes exceeds the critical angle and leave the waveguide (Fig. 3.1). In other words, the Stokes pulse loses more of its extreme modes as it passes through a bend, despite the same angular change of the guiding fibre for both Stokes and anti-Stokes modes.

The altered differential attenuation of the Stokes and anti-Stokes signals was observed by Arnon et al. (2014b), and is one of the reasons why Hausner et al. (2011) and Van de Giesen et al. (2012) promoted manual calibration of the differential attenuation for separate sections of the cable. Unfortunately, since the loss in this case is asymmetrical with the direction of light travel (as may be understood by thinking about the first 100 m of cable, where the light entering the coil will experience significant differential attenuation, but the light leaving the coil will have settled down to a constant rate of attenuation), the double-ended procedures presented in the literature are not applicable to these unique defects. However, in absence of better calibration methods, double-ended calibration is often preferred.

Important developments in fibre-optic technology over the past 10 years include significant advancements in producing fibres that are "bend tolerant" or even "bend insensitive". These terms refer to the design of the index of refraction transitions specifically to obtain low decay when a signal passes through a bend of such a fibre. Similar to most multimode fibres applied for Raman DTS, bend-tolerant fibres normally have a core diameter of 50 µm. However, by radially varying the fibre's refractive-index, more signal is reflected back into the core instead of lost through its surrounding cladding. One example of bend-tolerant fibres is the Corning ClearCurve™ (Briggs et al., 2012). Attenuation in this fibre is reported to be

Table 3.1: Fibre-optic cables used in this study.

Cable	Manufacturer	Part number	Specifications	Diameter
A	AFL	SR0015161001	Tight-buffered, aramid yarn	1.6 mm
B	AFL	SA0015301601	Tight-buffered, aramid yarn	3 mm
C	Kaiphone	JE-2-E2000/APC-2-E2000/APC-G1-P-60-W-1500M	Loose tube, gel-filled, armouring (steel flexible tube and braiding)	6 mm

less than $2.3\,dB\,km^{-1}$ for an 850 nm light signal and less than $0.6\,dB\,km^{-1}$ for a 1300 nm signal (Corning ClearCurve Multimode Optical Fiber Product Information, 2015). This type of fibre was unavailable in our study. Fundamentally the same losses are expected with tight-bends even when using bend-tolerant fibres, but delayed to occurring at smaller radii (e.g., Arnon et al. (2014b), who employed bend-tolerant fibre). Thus our findings should translate to all fibres, though the specific bending thresholds at which the effects are observed should be expected to differ per fibre.

The cable design encasing the fibre element can also affect the passage of light. Most notably, use of a tight-buffered jacket over a loose tube cable increases the amount of strain conveyed from the cable to the fibre in comparison to loose-tube constructions. Several types of armouring may also produce micro-bends in coiled fibres.

In a laboratory experiment, we compare a tight-buffered cable of 1.6 mm diameter (AFL, Duncan (SC), USA) with two thicker cables for signal loss and differential attenuation (Table 3.1). The signal loss is studied as a function of coil diameter and distance from the start of the coil. Our study employs the time-averaged Stokes and anti-Stokes signals along the three different cables that are wound around PVC tubes of 125, 75, 50, 32, 25, and 16 mm diameter. The tough metal casing of the thickest cable made it impossible to properly wrap it to a coil of 25 mm diameter or smaller. We therefore omitted the 25 and 16 mm coils for the thickest cable. The data were taken during a 65 h measurement period in a tank of water with a uniform and almost constant temperature. The DTS instrument was a Silixa Ultima-S (Silixa Ltd., Hertfordshire, UK).

3.3 Results and discussion

The Stokes and anti-Stokes data from the three cables in the laboratory set-up were averaged over the 65 h period to reduce the effect of noise (Fig. 3.2), and signal loss per metre for the different coils and cables was computed (Fig. 3.3). In Fig. 3.2, bending-induced losses are characterized by a relatively large signal loss at the entrance of the coil.
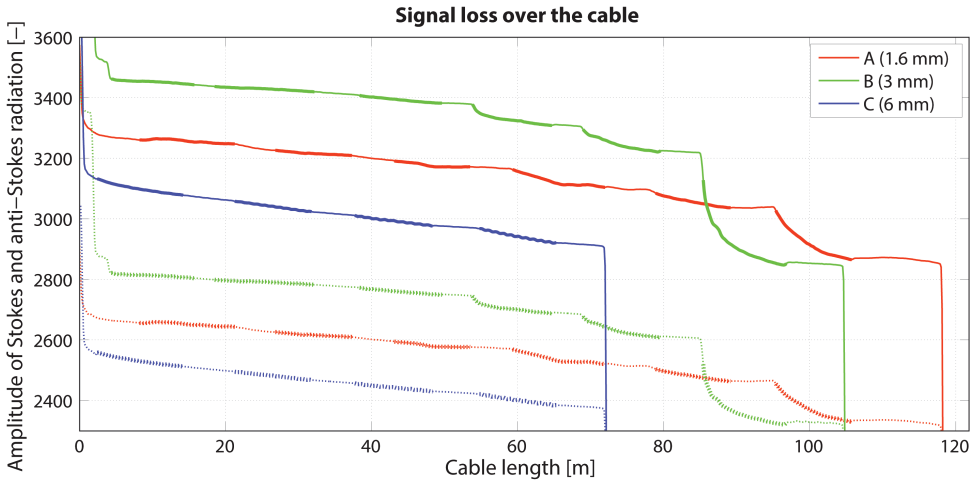
Figure 3.2: Amplitude of Stokes (solid lines) and anti-Stokes (dashed lines) radiation along the cables A (1.6 mm; red), B (3 mm; green), and C (6 mm; blue) when passing subsequent coils, marked by the thick sections of the graph. The coil diameters, from left to right, are 125, 75, 50, 32, 25, and 16 mm.

3.3.1 Coil-induced attenuation

The top right pane of Fig. 3.3 generally confirms the higher signal *attenuation* for smaller coils. For the 1.6 and the 3 mm cables, the signal loss increases when a cable is wound around a smaller tube. Only for the 6 mm cable, the 125 mm diameter coil seems to experience a larger loss compared to smaller coils. A possible explanation is that micro-bends, as a consequence of improper winding, dominate the signal loss in this case.

3.3.2 Coil-induced differential attenuation

The bottom right pane of Fig. 3.3 shows the relation between the *differential attenuation* of the Stokes and anti-Stokes signals and the coil diameter. Although the data are not consistent in all cases, Stokes losses appear higher when compared to anti-Stokes losses for coils with narrower bends.

To complement the discussion on coil-induced differential attenuation in Arnon et al. (2014b), we consider the added Stokes emissions in more detail. Stokes photons arise from Raman scattering. As they move on, further scattering generates secondary Stokes emissions, part of which is in modes with a near-critical angle of incidence. The consequent decay of Stokes signal explains the observed exponential pattern according to Beer's law: Stokes photons are significantly more susceptible to loss when returning to the DTS instrument from further along the coil.

3.3.3 Decreasing attenuation along the coil

To investigate the effect of the slowly dissipating signal decay described by Arnon et al. (2014b), Fig. 3.4 separates the signal losses of Fig. 3.3 into three bins that
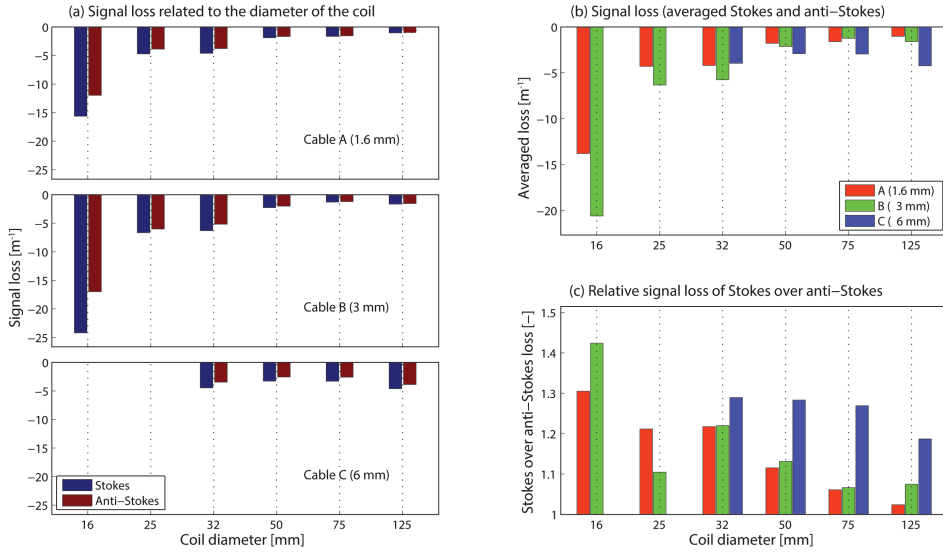
Figure 3.3: **(a)** Stokes and anti-Stokes signal loss (m^{-1}) for coil diameters of 16, 25, 32, 50, 75, and 125 mm, and for the cables A, B, and C (from top to bottom). **(b)** Combination of the bar plots in the left pane using the average of the Stokes and anti-Stokes signals. Loss decreasing with increasing diameter is indicative of bend-related light loss, which is generally associated with differential loss as a function of light frequency. **(c)** Ratio of Stokes over anti-Stokes losses as a function of coil diameter.

represent three sections of equal length. In most cases, the first section after the signal enters the coil shows the largest decay. The second section already shows less decay in most cases and the same holds for the third section.

Arnon et al. (2014b) demonstrated increased signal decay along the first 100 m of a coiled sensor, which employed bend insensitive fibre with a 26 mm wrapping diameter. Fig. 3.4 shows that the largest variation in signal decay can be found in the first few metres of the coil. However, for smaller diameter coils, further signal decay follows a Beer's law exponential pattern with a decay-coefficient of about 30 m.

The wider coils show a higher variability in signal decay (Fig. 3.4), which can be explained by the fact that the decay is more affected by micro-bends than bending radii. After about 10 m of cable, the tighter coils still experience an increased decay as compared to the largest radius coils. Recently introduced fibres, such as the bend-insensitive Corning ClearCurve™ fibre, are claimed to experience less influence from bends in the cable. However, the demonstrated effects play a role in all fibre-optic cables.

It should be noted that the sections in our measurement are just slightly more than 3 m long, but this offers useful insight into the physics that play a role in the first part of a cable coil. The presented losses cannot be considered representative for coils that extend over long distances. Our aim here is to show that selection of coil diameters below 32 mm, for the fibres and cable construction employed here,
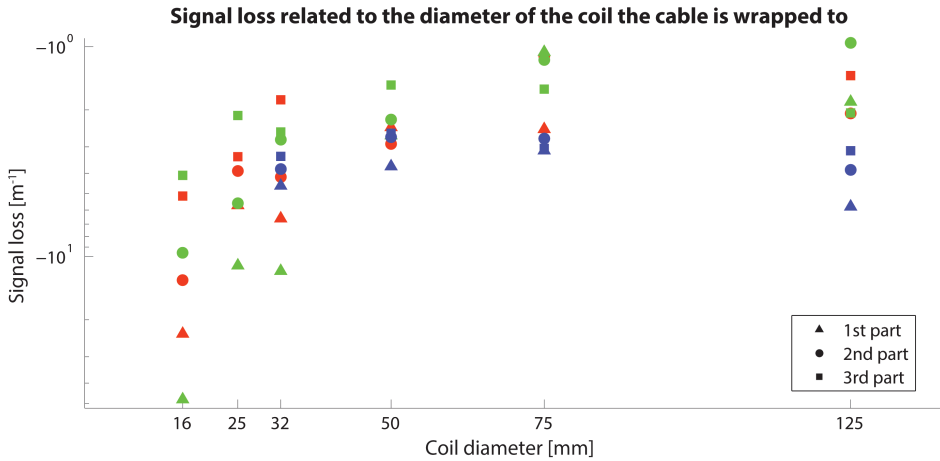
Figure 3.4: Signal loss (m^{-1}) over three subsequent sections of each coil presented for coil diameters of 16, 25, 32, 50, 75, and 125 mm, and for the cables A (blue), B (green), and C (red). The first, second, and third part each represent a third of the total coil length.

leads to significant losses at the start of the coil. This effect imposes a lower limit to the coil diameter one can apply. Care should be taken when choosing both the coil diameter and the number of separate coils applied to one cable.

3.4 Outlook

We have shown that coil-wrapped DTS measurements involve light attenuation in the bent fibre. Following up on this issue, this section discusses considerations for the design of the auxiliary construction, as well as the coil diameter.

3.4.1 Influence of coil diameters

The coil diameter influences measurements in three ways. First, a smaller coil diameter exacerbates signal decay (Fig. 3.2). Smaller coil diameters significantly decrease the potential measurement distance for a given cable.

Second, the decay is largest at the entrance of the coil and decreases further along the coil (Fig. 3.4). These results confirm the work of Arnon et al. (2014b). At the entrance of the coil, the light signal loses its most extreme modes that cannot be reflected back into the bent fibre due to their angle of incidence.

Third, coil diameter directly affects differential attenuation, and consequently temperature measurements themselves (Fig. 3.3). To this end, we recommend careful calibration of separate cable sections to achieve highly accurate temperature measurements and not using narrow coils when it can be avoided.

3.4.2 Influence of coil preparation

Significant practical issues arise when building a coil-wrapped DTS set-up. When a spaced cable winding is chosen, we recommend not fixing the cable into place with
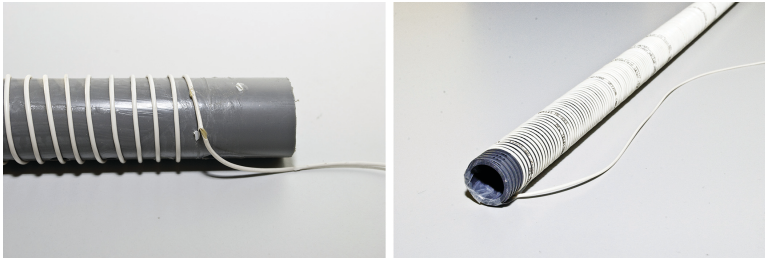
Figure 3.5: A damaged cable that was glued to a PVC conduit (left) and a cable wound through a furrow in the PVC conduit (right).

PVC glue or similar. These glues may be stronger than the cable's jacket, leading to tearing of the jacket, and facilitate the transmission of strain to the fibre, which can cause time-varying light losses as the system heats, cools, or is deformed by environmental forcing (Fig. 3.5a). Allowing the cable to move independently with any deformations in the supporting cylinder is preferred.

When the cable is not fixed to the support tube, a constant vertical position can be maintained by winding the cable about the tube with no space between wraps (as employed by Selker et al., 2006a), or by laying the cable into a pre-formed groove that has been machined into the support tube (Fig. 3.5b). Cutting helical grooves into plastic cylinders is easily done with a gear-head lathe, and allows the builder to vary in pitch (i.e., fibre length per unit cylinder length), while keeping the cable securely in place. Another option to fix a cable to the auxiliary construction is shrink-wrapping the coil with white plastic, which can also provide shade for the cable and lower the effect of direct exposure to solar radiation. Shrink-wrapping has been successfully applied by Suárez et al. (2011). This approach has been found successful, but may again lock the cable to particular locations on the pole, and thus encourage transfer of strain to the fibre if the pole is bent or exposed to asymmetrical solar heating.

There are other solutions for high-resolution DTS that do not require the user to wind a fibre-optic cable around an auxiliary construction. For example, Arnon et al. (2014b) employed commercially prepared BRUsens temperature $70\,°C$ high-resolution cable with a fibre stuffing of a factor 11 (fibre length per cable length). Amongst other potential set-ups to reach a high resolution, one could for example think of cable traverses at multiple levels (Sebok et al., 2013), or layered nets of cables, with the traverses or layers spaced at the demanded resolution. Such a set-up has the advantage that it also provides temperature data in the other spatial dimensions.

3.5 Conclusions

This chapter demonstrates and suggests solutions for two practical issues involving coil-wrapped DTS: (1) influence of coil diameter and (2) attachment method of the cable to the construction.

Laboratory measurements display the effect of coil-wrapped cables on both signal decay and differential attenuation. Differential attenuation affects temperature measurement and requires consideration during calibration of the wound cable sections. It was observed that especially at the start of the coil, the signal loss increased significantly for smaller coil diameters. Increasing the coil diameter reduces adverse effects of a bent cable, although it requires more space and averages out laterally varying temperature signals.

This chapter contributes to a better understanding of the effect of auxiliary constructions on coil-wrapped DTS measurements, allowing improved designs for future measurement set-ups. The proposed solutions and ideas can mitigate the adverse effects of coil-wrapped set-ups on high-resolution DTS.

3

4

Three-dimensional dense distributed temperature sensing for measuring layered thermohaline systems

Distributed temperature sensing has proven a useful technique for geoscientists to obtain spatially distributed temperature data. When studies require high-resolution temperature data in three spatial dimensions, current practices to enhance the spatial resolution do not suffice. For example, double-diffusive phenomena induce sharp and small-scale temperature patterns in water bodies subject to thermohaline gradients. This chapter presents a novel approach for a 3-D dense distributed temperature sensing set-up, the design of which can be customized to the required spatial resolution in each dimension. Temperature is measured along fibre-optic cables that can be arranged as needed. In this case, we built a dense cage of very thin (1.6 mm) cables to ensure that interference with flow patterns was minimal. Application in water bodies with double-diffusion-induced sharp temperature gradients shows that the set-up is well able to capture small-scale temperature patterns and even detects small unsuspected seeps and potential salt-fingers. However, the potential effect of the set-up on the flow patterns requires further study.

4.1 Introduction

With the advance of distributed temperature sensing (DTS) in environmental sciences, several studies have applied this technique to monitor vertical high-resolution temperature gradients in a surface water body (Vercauteren et al., 2011; Suárez et al., 2011; Hausner et al., 2012; Van Emmerik et al., 2013). Wrapping the fibre-optic cable to a coil has proven a useful strategy when only detailed data of the temperature profile in one dimension is of interest. However, when small-scale gradients in multiple dimensions are relevant, this method is less practical, because:

1. Sampling points anywhere on the coil, which usually has a diameter of several centimetres, are integrated to a single point in the horizontal.

2. The fibre-optic cables are often wound around a tube. Locating several tubes closely together significantly disturbs flows in the water column.

The aim of this study is to accurately measure horizontally and vertically varying temperature profiles with DTS. A new DTS set-up is designed to measure small-scale 3-D temperature profiles in a surface water body, which overcomes the mentioned disadvantages of wrapped coils. We apply this set-up, here called *Dense DTS*, in small-scale thermohaline systems. The set-up is largely able to capture the spatial temperature variability caused by double-diffusive processes.

4.1.1 Distributed temperature sensing

Temperature has long been recognized as a suitable tracer for measuring water flows (Slichter, 1905). For example, contrasting temperatures can help characterizing groundwater contributions to a surface water body (Stonestrom and Constantz, 2003; Anderson, 2005). Since the previous decade, distributed temperature sensing (DTS) has made its way into environmental sciences. This technique allows to measure numerous temperature samples along a fibre-optic cable, offering an efficient and accurate alternative for traditional temperature sensors (Selker et al., 2006b; Tyler et al., 2009).

Currently, the Silixa Ultima (Silixa Ltd., London, UK) DTS instrument provides the highest sampling resolution, sampling each 13 cm along the fibre-optic cable. Several studies that required a higher spatial resolution wound the fibre-optic cable to a coil (Ciocca et al., 2012; Euser et al., 2014). Many of these studies used PVC tubes as a support for these coils (Selker et al., 2006a; Suárez et al., 2010a, 2011; Vogt et al., 2010, 2012; Vercauteren et al., 2011). Hilgersom et al. (2016d) show that wrapping cables to narrow coils and the use of PVC support tubes can have adverse effects on the measurements. Cables with an internal stuffing of the fibre exist (Arnon et al., 2014a), but do not reach the desired spatial resolution in many applications where detailed measurements are required.

4.1.2 Boils and thermohaline stratification

Larger-scale and stable thermohaline systems allow for accurate monitoring by probing the water body with a single temperature or salinity sensor. In oceans, deep lakes, and boreholes, for example, determining the temperature profile with

a frequency of months to years can suffice to analyse how the layers in the system evolve (Schmid et al., 2004). When using multiple point sensors or a distributed sensor, more frequent monitoring is possible (Arnon et al., 2014a).

Thermohaline stratification is also observed at smaller scales. For example, boil seepage with salinities up to $5\,g\,l^{-1}$ are dominant salinization source in the Dutch deep polders (De Louw et al., 2010, 2013). Boils have a fairly constant temperature throughout the year that is colder than the surface water during summer and warmer during winter. The outflow of saline boil water with a constant temperature induces a stratified system with the relatively fresh water in the ditch on top. Double-diffusive convection occurs when the surface water is colder but less dense than the boil seepage.

In this chapter, boils are used to investigate the opportunities of Dense DTS for studying layered thermohaline systems where small-scale double-diffusive processes play a role. When coupling the temperature data to a hydrodynamic model, Dense DTS potentially allows to monitor seepage inflows with a contrasting temperature, whereas conventional methods require the placing of heat probes in the stream bed (Naranjo and Turcotte, 2015; Stonestrom and Constantz, 2003). This chapter focuses on the ability of Dense DTS to observe the development of, and temperature patterns in these layered systems.

4.2 Materials and methods

4.2.1 Three-dimensional DTS set-up

In order to accurately measure horizontally and vertically varying temperature profiles, we defined the following criteria for our DTS set-up:

1. The set-up should be able to accurately monitor horizontally varying temperature patterns;

2. The influence of the set-up on the local water flow should be as small as possible.

Our specific application for sharp thermohaline interfaces imposed an additional criterion:

3. The set-up should be able to monitor with a high vertical resolution around the sharp interface, which is located in the bottom third of the set-up for the present case studies.

It appeared that a set-up with horizontally distributed standing PVC conduits undesirably influences the water flow and does not provide enough opportunity to measure with a very fine vertical resolution. Besides, cables wrapped around small diameter PVC tubes can negatively influence the measurements (Hilgersom et al., 2016d). We therefore chose for a set-up in which horizontal nets of fibre-optic cable are spanned across a cage. In this way, closely spanned layers can provide sufficient temperature data near the sharp interface and the only material influencing the flow is the thin fibre-optic cable that occupies a maximum of 2 % of the set-up volume for the closely spaced cable nets.
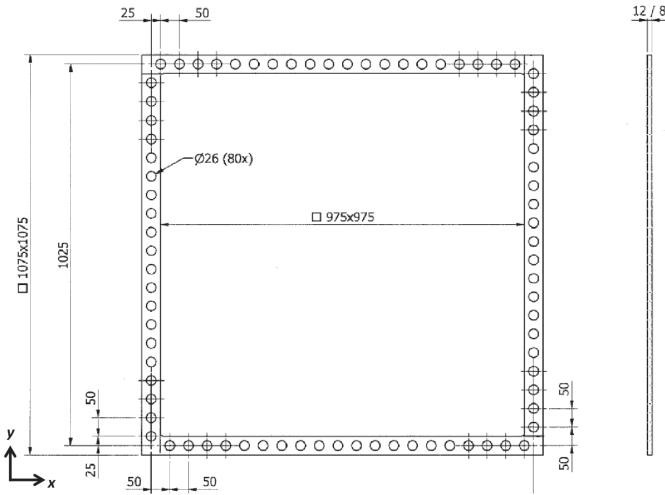
Figure 4.1: Size (in millimetres) of the PVC rings with the locations of the mounting holes for the PVC conduits.

The cage, with outer dimensions of 1 m x 1 m x 1 m, consists of 80 vertical bars with a helical groove to embed the fibre-optic cable at each turnaround. The bars are 25 mm PVC conduits, which are kept in place by three PVC squares, the bottom and top ones being 12 mm thick and the middle one being 8 mm thick (Fig. 4.1). At each turnaround, the cable is fixed in the groove with white duct tape, which inhibits shifting of the cable. The white colour is chosen to prevent undesired heating of the set-up due to solar irradiation (Hilgersom et al., 2016d).

In our set-up, we used two tight-buffered, bend tolerant 1.6 mm multimode cables (AFL, Cable A in Table 3.1) with lengths of 1143 and 1243 m. The only strain protection in the cables consisted of aramid fibres. Based on lab experiments (unpublished), we concluded that the signal attenuation was still low enough for accurate measurements at a bend diameter as small as 25 mm. The employed Ultima-S DTS device (Silixa Ltd., London, UK) has a sampling interval of 13 cm and a spatial resolution of about 25–30 cm. This resolution is necessary to measure horizontally varying temperature patterns with the described set-up. The two cables connect to the DTS device at both ends, and each of the four channels successively uses a 30 s integration time per time interval. For these settings, the manufacturer reports a temperature resolution of approximately 0.05 °C. To display a complete temperature profile for a certain point in time, the more than 34,000 data samples within the cage are linearly interpolated over time.

Hausner et al. (2011) and Van de Giesen et al. (2012) showed that manual calibration of the temperature measurements using the raw Stokes and anti-Stokes data usually outperforms the standard machine calibration. Besides, the bends in our set-up might cause spatially varying differential attenuation (Hilgersom et al., 2016d). We therefore applied the manual double-ended calibration presented in

Van de Giesen et al. (2012). Another advantage of manual calibration is that we are required to make in-depth interpretation of the data and spot possible flaws introduced by the many cable bends in the set-up.

Van de Giesen et al. (2012) described the manual calibration procedure for the differential attenuation, the energy shift between a photon at the incident wavelength and a scattered photon (γ), and the time-varying calibration parameter $C(t)$. We chose to calibrate differential attenuation and values for γ per cable and values for $C(t)$ per individual measurement direction. These parameters are used to calculate the temperature at each individual point along the cable from the locally measured Stokes and anti-Stokes signal.

The locations of these sampling points within the 3-D grid of the set-up are determined by placing the set-up in an outside environment of approximately 2 °C, and filling three PVC tubes at each corner of the set-up with hot water. Based on the local temperature peaks, the centre of each turnaround at the PVC tubes can be determined with an estimated accuracy of ~0.03 m. Applying this procedure to data collected in both directions along the cable further increases the accuracy. The position of the cables at the corner points is consequently known in the xyz-grid used for locating all the sampling points within the cage. The other turnaround positions follow from division of the cable distance in-between the corner locations over the amount of spans for each layer. The grid locations of the sampling points are then calculated for each span individually.

The tight-buffered cables employed here tended to expand and shrink significantly with changing environmental temperatures. We therefore extended the calibration procedure with an additional length correction to better determine the location dependent calibration parameters, and to determine the varying locations of the temperature samples during the measurements. During the calibration procedure, the cable length was determined for each point in time by applying a linear expansion coefficient to the cable-averaged machine calibrated temperatures.

The linear expansion coefficient is cable-specific, and was derived from differences in average cable length between the measurement periods. The cable lengths were determined first by matching temperature samples recorded from both ends of each cable. Based on the cable lengths and average temperatures during three case studies (Section 4.2.3) and during the determination of the sampling point locations (approximately 2 °C), the linear expansion coefficient of the cable was found to be $2.6 \cdot 10^{-5}$ K^{-1}, with a standard deviation of 3.5 %. This is in accordance with the linear expansion coefficients of other glass fibre reinforced polymers.

4.2.2 Thermohaline stratification

To determine whether the thermohaline systems in our case studies are stable, unstable, or promote double-diffusive layering, the Turner angles, Tu, of these systems are calculated (Eq. 1.3; Ruddick, 1983). To this end, we need to determine the thermal expansion coefficient, α, and solutal expansion coefficient, β. These coefficients are dependent on temperature and salinity itself, and are calculated for the average salinity and temperature on the interface. We employ coefficients derived from a linear regression to the density derivatives to temperature and salin-
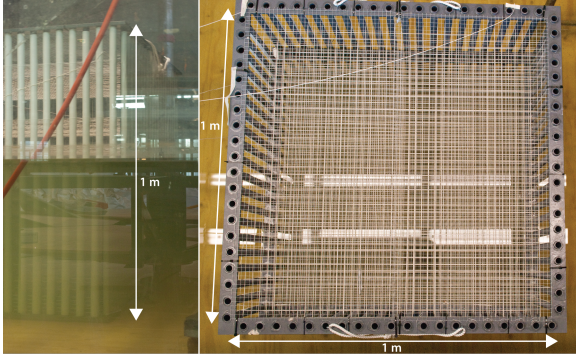
Figure 4.2: DTS set-up deployed in a laboratory test set-up.

4

ity, where the density is calculated from an approximation to the Unesco formula (Unesco, 1981) by Wright (1997):

$$\alpha\,(T,S) = -2.285097 \cdot 10^{-5} + 1.324876 \cdot 10^{-5} \cdot T - $$
$$9.288537 \cdot 10^{-8} \cdot T^2 + 1.563353 \cdot 10^{-6} \cdot S, \tag{4.1}$$

$$\beta\,(T,S) = 7.998742 \cdot 10^{-4} - 2.774404 \cdot 10^{-6} \cdot T + $$
$$3.188185 \cdot 10^{-8} \cdot T^2 - 4.151510 \cdot 10^{-7} \cdot S. \tag{4.2}$$

4.2.3 Case studies

This chapter presents results from laboratory measurements (Case 1), and field measurements in the surface water covering boils in the Noordplas Polder (Case 2) and Kortenhoef (Case 3), all in the Netherlands. The complete data sets and additional graphical representations are published in Hilgersom et al. (2016b).

Case 1: laboratory measurements

The laboratory set-up consisted of a 2.5 m x 2.5 m container, containing water up to a level of 0.5 m with a salinity ranging from 0.7 to 1.4 g l^{-1} (Fig. 4.2). In this study, we slowly built up a more saline layer from below. The water, with a salinity ranging from 2.6 to 2.9 g l^{-1}, entered the container through a circular hole with a diameter of 0.5 m located in the centre of the bottom. The hole was covered with an anti-rooting membrane to equally distribute the inflowing water over the hole. The water level was maintained by placing vertical pipes, which were pinched over the full depth, in the four corners of the container. Siphons lead the water in the pipes outside the container into buckets, which were filled to their top edge located at the water level, and in total were overflowing with the same discharge as the inflow.

The actual purpose of this set-up was to simulate saline boil seepage inflow, but it also provides the opportunity to study a layered thermohaline system. The

Table 4.1: Water temperatures (T) and salinities (S) of the surface water and the inflow, and inflow discharges (Q), for the six runs. Bold temperatures indicate the highest values (surface water vs. inflow). The last two columns indicate the physical stability of the layered system based on Turner angle Tu: unconditionally stable (STA) or double-diffusive convection (DDC).

Run	Duration	Surface water			Inflow		Stability	
	(h)	T (°C)	S (g l^{-1})	Q (m³ h^{-1})	T (°C)	S (g l^{-1})	Nature	Tu (°)
1.	2.4	22.3	0.7	0.11	**25.9**	2.6	DDC	-82.2
2.	2.2	22.6	0.9	0.10	**25.8**	2.4	DDC	-89.3
3.	4.8	22.8	1.0	0.11	**27.2**	2.5	DDC	-85.8
4.	3.4	**22.8**	1.2	0.11	21.8	2.6	STA	-30.0
5.	1.9	22.7	1.35	0.12	**25.1**	2.9	DDC	-85.7
6.	3.6	**22.8**	1.4	0.13	21.5	2.7	STA	-23.1

inflow salinities and temperatures were monitored with a CTD-diver (Schlumberger Water Services, Delft, the Netherlands) underneath the anti-rooting membrane. As a reference, the temperatures near the bottom and near the water surface were monitored with two TD-divers (Schlumberger Water Services, Delft, the Netherlands).

Table 4.1 divides the laboratory measurements into six runs, all performed between 19 August and 21 August 2013. Salinities were calculated from measured electrical conductivities normalized to a reference temperature of 25 °C according to the equation presented by Schemel (2001). The inflowing water had a higher salinity, and a temperature that was either higher or lower than the surface water temperature. The surface water was mixed before each run in order to prevent initial variations in temperature and salinity. Based on the Turner angles, we expected that stable layering developed when cold water flowed in from the bottom, and double-diffusive convection when warm water flowed in. The conduits in the laboratory set-up delayed the inflow of water with the desired properties, causing time varying inflow discharges (Q), salinities (S), and temperatures (T). Therefore, the presented inflow properties are averages.

Case 2: field measurements Noordplas Polder

During earlier studies, saline boils were observed in the Noordplas Polder (De Louw et al., 2013; Vandenbohede et al., 2014; Hut et al., 2016). The inflow of highly saline water through the bottom of a relatively fresh water body is expected to cause a stratified system with fresh water above saline water. Also during winter, the warmer saline water has a higher density than the colder fresh water in the ditch, causing double-diffusive convection ($-69° < Tu < -45°$ for the measured salt gradient between groundwater and surface water).

The DTS set-up was placed at the bottom of the ditch above a boil in the Noordplas Polder from 28 September until 11 October 2013. In this thesis, we focus on the part of the measurement period between 9 October and 11 October, when outside temperatures dropped from several degrees Celsius above toward several degrees Celsius below the boil temperature. To check the occurrence of stratification, the salinities and temperatures near the bottom and near the water surface

were monitored with two CTD-divers.

We increased the water level to about 14 cm in order to stimulate the development of a layered system by building a small weir downstream. This weir was placed far enough not to influence the development of a saline layer around the boil, but close enough to decrease circulating currents as a consequence of a large wind fetch over the ditch. The discharge over the weir was measured several times during the field campaign by recording the time required to fill a bucket, and varied between 0.3 and 0.7 l s^{-1}. These discharges yielded a negligible flow velocity of maximum 5 mm s^{-1} through the ditch of about 1 m wide. This was confirmed by acoustic flow measurements with an OTT ADC (OTT Hydromet, Loveland, CO, USA), which reported similar values with a maximum of 15 mm s^{-1}. The emergent flow velocity from boils in the Noordplas can reach values up to 10 mm s^{-1} (De Louw et al., 2010).

Case 3: field measurements Kortenhoef

At the measurement site in Kortenhoef, boils discharging fresh water occur. This preferentially exfiltrating groundwater was thought to have infiltrated in a nearby ice-pushed ridge. The surface water in this system is slightly more saline (measured salinities between 0.22 and 0.29 g l^{-1}) due to seepage inflows of shallower groundwater. In this case, the thermohaline system is expected to produce salt fingers when the temperature in the surface water is more than 0.5 °C higher than the boil seepage temperature (45° < Tu < 90°), and else to be unstable.

Between 17 and 24 March 2014, the DTS set-up monitored the surface water temperature above a fresh water boil with a salinity of 0.17 g l^{-1}. The water level was controlled manually by a downstream gate, and was on average 22 cm; due to a sloping bed, 18 cm on the right side and 27 cm on the left side of the set-up viewing downstream. OTT ADC measurements reported a maximum flow velocity of 0.03 m s^{-1} at the water surface. However, most of the time the flow velocities reduced to indistinguishable from 0 m s^{-1}. As in Case 2, CTD divers monitored temperatures and salinities near the bottom and water surface.

4.3 Results and discussion

4.3.1 Case 1: laboratory measurements

This subsection presents results from two laboratory simulations with different temperature and salinity contrasts (Table 4.1). Fig. 4.3 presents an example of a 3-D temperature profile obtained by our measurement set-up. The DTS set-up measured with a decreasing vertical resolution toward the top. As a consequence, the temperatures near the air-water interface appear noisy after linear interpolation over space. However, here we are only interested in detailed measurements in the lower part of the water column.

To allow a more detailed analysis, we show results of Runs 2 and 6 (Fig. 4.4 and 4.5, respectively) as horizontal slices at six different levels, and at different moments. This way, one can see the interface evolve. In both simulations, the higher slices uniformly show the initial temperatures 45 min after the measurements
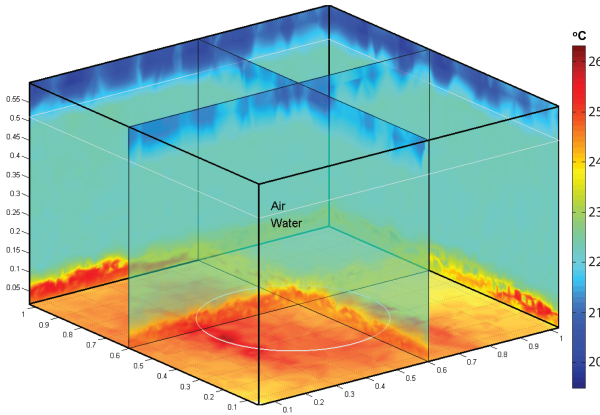
Figure 4.3: 3-D representation of a measured temperature profile in the laboratory set-up.

had started (Fig. 4.4a and 4.5a). At this time, the lower slices already show locations where the seepage water disturbed the interface.

Although the seepage water was expected to rise vertically through the covered circular hole, the disturbed interfaces in both cases show a square pattern around the inflow location (Fig. 4.4 and 4.5). Apparently, the anti-rooting membrane was less permeable than expected, causing the water to seep sideways. The square pattern of warm upward flowing water matches the location of the wooden strips used to nail the membrane to the floor. This can be considered a defect of the laboratory set-up. However, at the same time, it demonstrates the DTS set-up capability to locate such temperature patterns with centimetre accuracy.

For Run 2, we observed that on the locations where water was seeping sideways from the inflow, it consequently flowed upward over the bottom 4 cm (Fig. 4.4). Based on the Turner angle (Table 4.1), it was expected that local convection cells were formed as the most effective physical mechanism to counteract the temperature and salt gradient between the inflowing water and the surface water (i.e., double-diffusive convection). Although the occurrence of convection cells cannot be concluded from the data, we observed the tendency of diffusing heat in lateral and upward direction from the light blue colors surrounding the yellow patterns in Fig. 4.4.

At the latest stage of Run 2 (Fig. 4.4c and 4.6a), a clear interface was developing at about 50 mm, with the warmer water more spread over the bottom layer. This was the moment that the water body started to clearly develop toward a dual-layered system that was not much disturbed by the inflow properties. At about 50 mm, one can see that the interface was still not completely homogeneous. This could have been the remainder of the disturbance caused by the inflow. Alternatively, the inhomogeneities in the interface, which exceeded the temperature resolution of the measurements ($\sim$0.05 °C), could have been caused by the cables themselves. Their influence was expected to be small, since their relative volume over the complete set-up is only 0.4 %, and in the bottom 10 cm it is 2 %, but the

Figure 4.4: Horizontal temperature slices for a hot inflow in the laboratory set-up (Run 2), at 15, 20, 25, 30, 40, and 50 mm above the bed. The displayed situations are at **a)** 0h45, **b)** 1h30, and **c)** 2h15 after the start of the measurements.
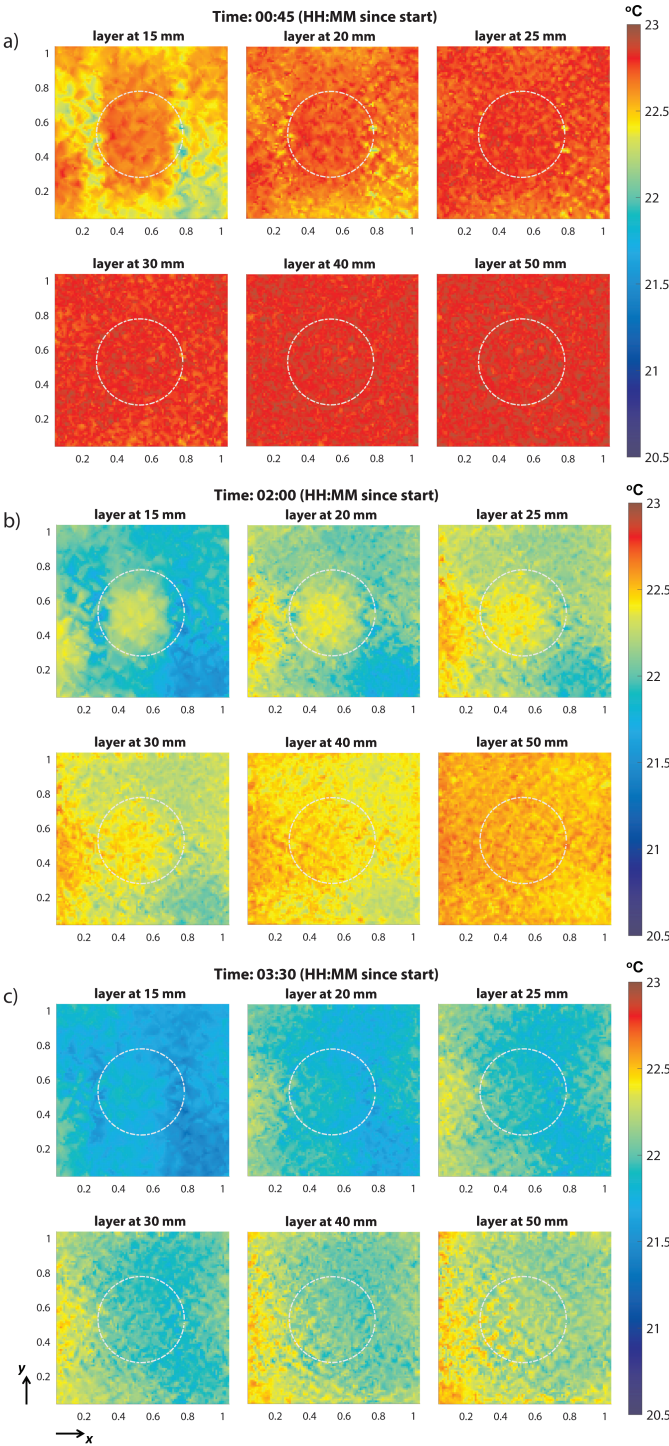
Figure 4.5: Horizontal temperature slices for a cold inflow in the laboratory set-up (Run 6), at 15, 20, 25, 30, 40, and 50 mm above the bed. The displayed situations are at **a)** 0h45, **b)** 2h00, and **c)** 3h30 after the start of the measurements.

a)

Laboratory, Run 2
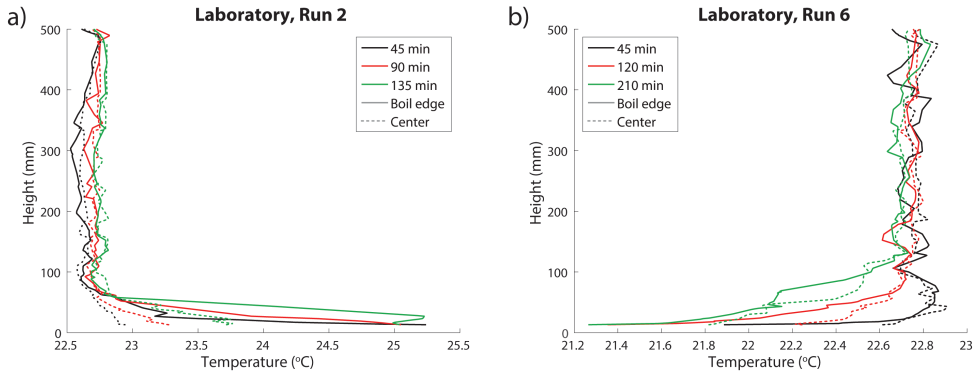
b)

Laboratory, Run 6

Figure 4.6: Vertical temperature profiles for two case studies in the laboratory. The locations are selected to mark the differences between the temperature profiles above the boil centre and the boil edge.

cable nets could have induced small-scale convection cells by the physical tendency to diffuse the temperature interface.

For Run 6, the inflowing colder and fresher water promoted the development of a stable interface. The lack of a buoyancy-inducing gradient yielded molecular diffusion as the main physical driver to counteract the salt-temperature interface. Again, we observed the initial inflow disturbances, extending to about 30 mm (Fig. 4.5a and 4.5b). After more than 2 h, the cold lower layer started to become more homogeneous over the horizontal cross-section (Fig. 4.5c). At the interface, though, again some inhomogeneities were visible that could have been caused by the cable nets themselves. The effect of the cable nets is difficult to quantify, and we recommend further study on how it affects the flow patterns. Fig. 4.6b displays a delayed rise of the interface above the boil compared to the interface at the boil edge throughout the measurement period.

4.3.2 Case 2: field measurements Noordplas Polder

The measurement campaign in the Noordplas Polder comprised a transition from a warmer period to a colder period. This, together with the diurnal temperature fluctuation, allowed us to compare a warm surface water situation (Fig. 4.7a) with a situation where the surface water was turning cold (Fig. 4.7b and 4.7c).

During the warm period, the cold and saline seepage water built up a stable interface above the boil ($|Tu| < 45°$). A diffusive layer, between 40 and 60 mm, formed an interface between the seepage and surface water layer (Fig. 4.8a). The hot top left corner of Fig. 4.7a marked a local sediment deposit up to a level of 50 mm, which was formed over the previous days and was under direct forcing of solar radiation. Due to high upward velocities, boils often transport sand from the aquifer to the surface, as illustrated by the sand volcano in Fig. 1.3b. The lower rim of the DTS set-up apparently changed the flow profile near the bottom allowing local sediment settlement. Around the sediment deposit, the colder seepage water spread over the bottom in the other directions.
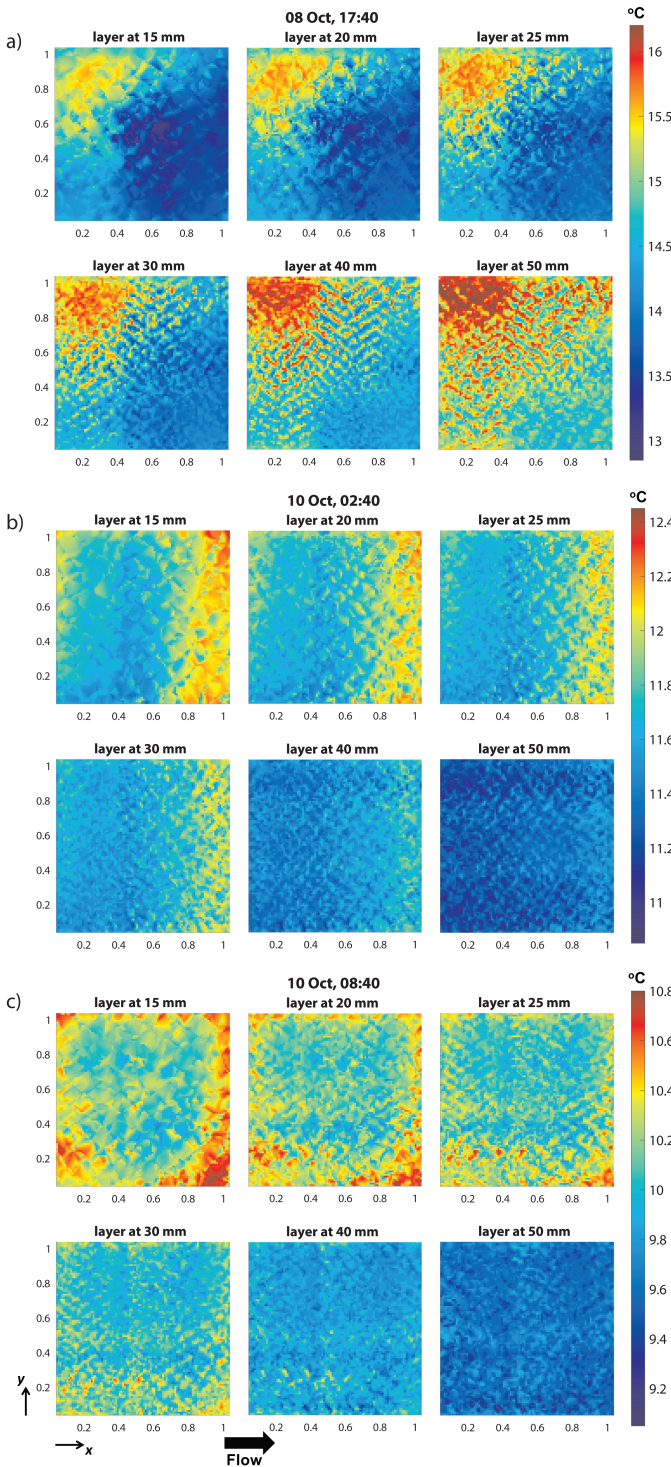
Figure 4.7: Horizontal temperature slices at 15, 20, 25, 30, 40, and 50 mm above a boil seep in the Noordplas Polder. The displayed situations are during **a)** a warm afternoon (8 October 2013, 17:40), **b)** at the start of a cold night after a warm day (10 October 2013, 2:40), and **c)** at the end of a cold night after a warm day (10 October 2013, 8:40).
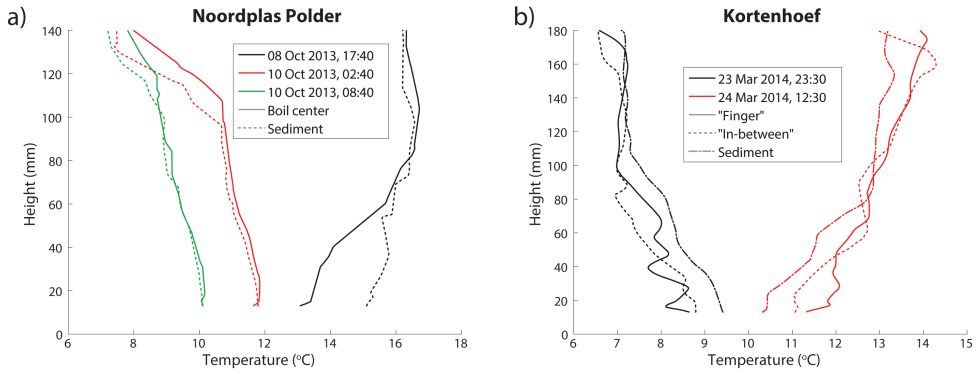
Figure 4.8: Vertical temperature profiles for the case studies in the Noordplas Polder (**a**) and Kortenhoef (**b**). The locations of the temperature profiles are selected to mark interesting differences in the vertical temperature patterns.

During the transition period, the surface water started to cool down from the top. Underneath, a warm layer temporarily persisted, which was disrupted by the slightly less warm seepage water in the centre of our measurement set-up (Fig. 4.7b). The hot spots near the edges of Fig. 4.7b show that sediment, which was heated over the past day, had further accumulated around the boil during the measurement period. Due to the salinity gradient, both the seepage water and the surrounding warm water remained denser than the overlying surface water ($-69° < Tu < -45°$). The weak diffusive layering at these Turner angles is not clearly visible in Fig. 4.8a, although some unsharp steps can already be spotted for the small temperature gradient at this time. On October 10, 2:40, the surface water had cooled down to about 11.2 °C at a level of 50 mm. The sediment temperature was approximately 1 °C higher.

At 8:40, the sediment had further cooled down to 10.7 °C, and the cold water had reached the lower 1.5 cm (Fig. 4.7c). In the centre, the warmer seepage water mixed with the surface water within the lower 30 mm, above which the temperature decreased stepwise (Fig. 4.8a).

4.3.3 Case 3: field measurements Kortenhoef

Like Case 2, the field data from Kortenhoef showed an accumulation of sediment around the boil. Particularly during night, the heat sustaining sediment showed clear temperature patterns (Fig. 4.9a). Although the seepage water was approximately 10 °C, no direct traces of it were visible, as it tended to mix directly with the surface water. A colder horizontal band is visible around $y \approx 0.25$ m, which is on the shallow side of the DTS set-up.

At 12:30 the next day, the sediment showed a delayed heating of 1 °C compared to the enclosed surface water near the bottom (Fig. 4.9b). This time a warmer horizontal band is visible on the shallow side. Interestingly, a diffusive interface had developed at 50 mm above the bottom, from which salt fingers seemed to develop. The temperature patterns of the downward salt fingers extended to the layer at
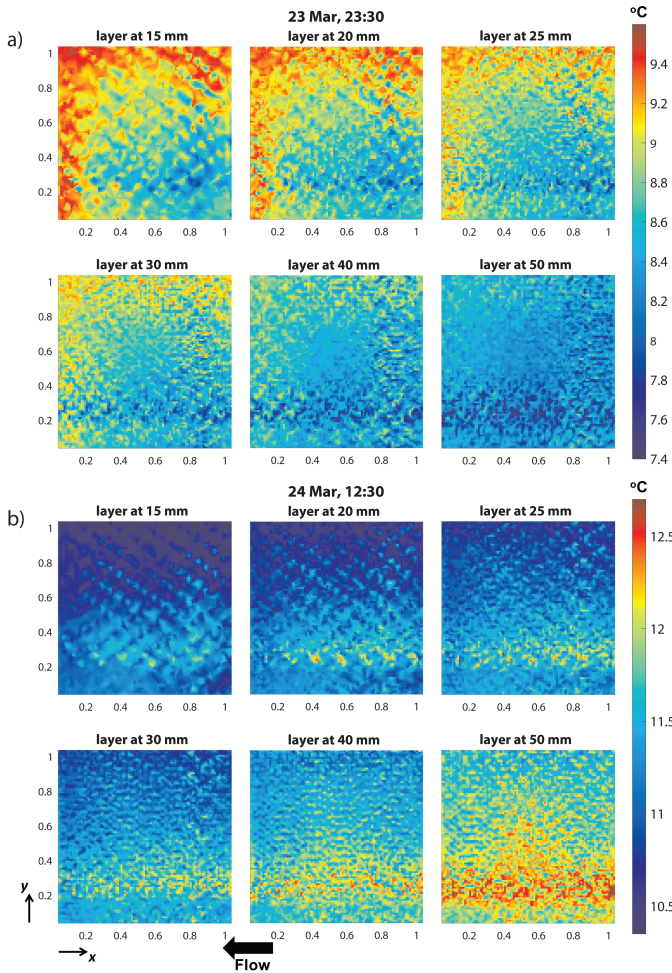
Figure 4.9: Horizontal temperature slices at 15, 20, 25, 30, 40, and 50 mm above a boil seep in Kortenhoef. The displayed situations are during **a)** a cold night after a warm day (23 March 2014, 23:30), and **b)** a warm afternoon (24 March 2014, 12:30).

15 mm, where they are still visible as yellow dots. In the layers above, these yellow dots widen, while approximately sustaining their position, although the data shows some interference patterns for the highest layers. Fig. 4.8b plots the temperature profiles at the location of an assumed salt finger and at a location in-between two salt fingers. The salt finger temperature was up to 1 °C higher underneath the interface at 50 mm, and colder above. Despite this clear pattern, care should be taken, as the temperature patterns at these two locations also differed at night, when overturning of the less dense bottom layer was expected.

The occurrence of weak salt fingering was expected based on the salinity gradient and a temperature gradient of more than 0.5 °C (Section 4.2.3). The data show that the DTS set-up was able to potentially localize these small-scale patterns.

4.4 Conclusion

This chapter describes a new DTS set-up which allows 3-D high-resolution temperature measurements. Stacked layers of cables woven through a cage in two horizontal directions allow the acquisition of a 3-D grid of temperature data points with free-to-choose resolutions. Because of our interest in thermal processes near the stream bed, we have chosen a very high vertical resolution within the lower 10 cm. Although the cable is bent at each turnaround, continuous coils are prevented. In order to correctly calibrate the temperature measurements and the location of the cable, the calibration method by Van de Giesen et al. (2012) was expanded with a procedure to account for thermal expansion of the cable.

One of the purposes of the 3-D DTS set-up is to study the evolution of temperature patterns in detail. Temperature measurements in three case studies demonstrated the set-up capability to observe small-scale temperature patterns, such as local seeps and double-diffusive processes. Although we have to be careful in our conclusions for the occurrence of salt fingers in Case 3, theory from double-diffusive phenomena confirm that they potentially occur in the studied thermohaline system. Besides, the accumulation of sediment around the studied boil seeps in lowland areas (Cases 2 and 3) could be observed based on the sediment's delayed heating and cooling compared to the surface water.

The influence of the DTS set-up on the observed water systems is difficult to quantify. In the laboratory studies, the closely spaced cable nets seemed to slightly influence the development of thermohaline interfaces. These disturbances need to be studied in more detail to be conclusive about the influence of the measurement set-up. However, the absence of cable supports in the area of interest makes it unlikely that the set-up influences the measurements more than the currently used constructions for coil-wrapped DTS (e.g., PVC conduits).

We recommend further study of the performance of the DTS set-up for small-scale patterns, as caused by salt fingers, in a laboratory set-up. This can for example be done by improving the presented laboratory set-up with a uniform inflow, allowing to slowly build up an interface with warmer and more saline water on top. Variation of the environmental temperature could allow to further study temperature effects on the calibrated cable positioning within the device.

5

Heat and salt transport near the sloping edge of a solar pond: a two-dimensional numerical study

Salt-gradient solar ponds are used to store incident solar radiation as thermal energy in a hypersaline water layer at the bottom. The density-gradients in the pond induce a system of double-diffusive convective layers, where the fresh top layer insulates the heated bottom layer. Despite the existence of numerous measurement and modelling studies, the underlying physics are not yet completely understood, especially near sloping side walls. This modelling study adds to the understanding of the principles behind the solar pond physics. In addition, the study examines the merit of free-surface models for these types of simulations, as most modelling studies have assumed a rigid-lid approach to solve the Navier-Stokes equations. To this end, a two-dimensional vertical free-surface model was set up for a laboratory scale solar pond with a sloping wall, including a new shortwave radiation extinction model for artificial lights. Measurements and modelling results compare well for the temperature development near the slope, although the model overpredicts the buoyant heat transport along the sloping wall. The model reveals how this heat flux warms up the non-convective zone, even above the flat pond bed. The results lead to a better understanding of the dynamics in a solar pond where a significant fraction of the total bed surface is inclined.

5.1 Introduction

A salt-gradient solar pond effectively stores heat from solar radiation in its artificially stratified water body (Weinberger, 1964). Over the past 40 yr, numerous studies have attempted to model the heat-storage in solar ponds (Rabl and Nielsen, 1975; Cathcart and Wheaton, 1987; Giestas et al., 2009; Suárez et al., 2010b). However, the effect of a sloping pond shore has never been included in these models. This article presents model results for a side-sloped solar pond, which are validated with laboratory results presented in Suárez et al. (2010a).

A solar pond stores solar energy in its hypersaline bottom layer, which is insulated from the top by a fresh water layer. A large salinity gradient prevents gravitational overturning of the water body when the bottom layer heats up. Instead, a system of double-diffusive convection is initiated with two convective zones in the fresh and saline layer, separated by a non-convective zone (NCZ) with a downwards increasing salinity and temperature gradient. The shortwave radiation penetrating the water body is stored as thermal energy. The energy stored in the upper convective zone (UCZ) is mainly lost through the water surface, as a consequence of convective transport. The energy stored in the lower convective zone (LCZ) is only lost by conduction over the pond bed and diffusion through the upper interface. Additionally, buoyant transport over a sloping shore may transport heat toward the surface. Nevertheless, a large part of the stored thermal energy remains within the LCZ, and may be recovered for energy consumption by a heat exchanger.

For more than half a century, researchers have been trying to model the heating of a solar pond and the potential energy recovery. Weinberger (1964) was one of the first applying a 1-dimensional (1-D) numerical model. Rabl and Nielsen (1975) carried out 1-D calculations focusing on the optimization of the solar pond dimensions. Cathcart and Wheaton (1987) modelled the thermal energy increase of a solar pond based on measured surface temperatures and a model for vertical mixing. González et al. (2016) applied constructal theory to a 1-D model in order to optimize the configuration and sizes of solar ponds within a solar pond field.

Giestas et al. (2009) presented a 2-D numerical study of the salt and heat transport. Their experimental and numerical data provided good insights into the development of the convection cells. Suárez et al. (2010b) applied a 2-D numerical approach as well to model effects of meteorological influences and the erosion of the NCZ on short and medium time-scales in a shallow eutrophic pond. Suárez et al. (2014) applied the same numerical model to a laboratory-scale solar pond to study the differences between small- and large-scale solar ponds. This modelling study did not yet include the sloping bed in their laboratory set-up.

Ouni et al. (2003) applied a mass balance and energy balance approach for the three zones of a solar pond in order to derive the temperature and salinity development over depth. Taking into account the heat extraction and replenishment of brine in the LCZ, and fresh water replenishment in the UCZ, they could also evaluate the stability criterion for the thermohaline stratification in the solar pond. Where Ouni et al. (2003) calculated stability based on the density gradient ratio, Branco and Torgersen (2009) applied a dimensionless stratification parameter to predict the stratification of mesotrophic or eutrophic shallow ponds. This parameter,

originally defined by Holloway (1980), applies the ratio of the buoyancy flux, which includes the net solar radiation, and the mixing energy in the water body. Although Branco and Torgersen (2009) did not study a solar pond, the stratification parameter can be used to study the functioning of a solar pond. Both Ouni et al. (2003) and Branco and Torgersen (2009) recognized that convection currents near the sloping edges of a pond may affect stratification.

Jubran et al. (2004) used a 2-D model to study the influence of a sloping wall on the growth of convective layers. Although the modelled convective layers compared reasonably well to experimental data and showed a significant effect of an inclined wall, this study does not predict the long-time performance of such a solar pond.

The current study models the laboratory set-up presented in Suárez et al. (2011, 2014) with SWASH, which is a free-surface Navier-Stokes model. Since SWASH was developed to simulate wave fields approaching the shore, the model supports the simulation of flow processes along the sloping wall. Further, the model is capable of simulating rapidly varied flows, which is important to the flow simulations in the pond due to its large density gradients. The modelling approach decomposes the pressure term into hydrostatic and non-hydrostatic terms. The latter incorporates local accelerations due to the large density gradients in the solution procedure, which are neglected when a hydrostatic approximation is applied. The SWASH model code is open source and can be extended for operational use (SWASH source code (Version 1.20), 2011). We extended the model code with a thermal energy module describing the heating of the solar pond due to incoming radiation and conductive heat exchange with its surroundings (Subsection 5.2.2).

The modelling study aims to help understanding the processes that play a role in a solar pond with a sloping wall. The second purpose is to investigate the added value of free-surface models for the simulation of solar ponds as compared to the rigid-lid assumption that is often applied. The 2-DV model set-up includes the sloping bed with an angle of 45°, which forms half of the total pond bed in the laboratory set-up. This grid set-up allows a close look at how a sloping bed affects the heat transport near the edge of a solar pond. The modelled temperatures along the sloping wall compare well with the laboratory data, although deviations occur above the flat pond bed.

5.2 Methods

5.2.1 Measurements

A diagram of the laboratory-scale solar pond where the data were collected is presented in Fig. 5.1. The pond has one diagonal (45°) and three vertical side walls. It was lined with a regular black-pond liner and insulated with ~5-cm thickness polystyrene foam sheets. Three high-intensity discharge lamps (Super Grow 1000 W, Hydrofarm Inc., Petaluma, CA) were installed over the pond to simulate solar radiation.

Air temperature and relative humidity were measured using a shielded sensor (HPMC45-L, Campbell Sci., Logan, UT). Two pyranometers (LP02, Hukseflux, Delft, the Netherlands) and one net radiometer (Q-7.1, Campbell Sci., Logan, UT) deter-

mined the net shortwave radiation (SWR) and longwave radiation (LWR) above the water surface.

We measured the temperature inside the pond with two systems. The first system is a vertical high-resolution distributed temperature sensing (DTS) system, which was installed near the middle of the flat pond bed, at $x = 36$ cm from the left vertical wall and at $y = 23$ cm from the front parallel side wall (Fig. 5.1). This system allowed observation of the thermal profile in the pond with a spatial resolution of 1.1 cm and a temporal integration time of 5 min. Wrapping a fiber-optic cable around a PVC pipe potentially leads to measurement errors when applying small-diameter windings and glue to fix the cable on the PVC pipe, and when solar radiation can directly heat the cable (Hilgersom et al., 2016d). To minimize these effects, the cable was secured by placing it on a threaded 52 mm-diameter tube and shrink-wrapping the cable with white plastic. A radiation shield prevented direct radiation on the DTS system by the lamps.

The second system comprises a set of fifteen electrical conductivity (EC) electrodes with temperature compensation (SK23T, Van London-Phoenix Company, Houston, TX) that were installed in one of the parallel side walls of the pond. Ten of these electrodes were placed in a vertical profile 38.5 cm from the left side wall, and five electrodes were installed near the diagonal wall (Fig. 5.1).

The EC electrodes were also used to monitor the EC profile within the pond and measured the variables at 5-min intervals. Literature provides contradictory EC - salinity relationships for high EC values (Walton, 1989). Since our EC measurements serve as a reference to investigate the shape of the salinity profile over depth, we employ a rough linear conversion constant $K = S/EC = 0.6$, which is selected to fit the highest initial salinities, S (g l^{-1}), to the highest initial EC measurements (mS cm^{-1}). No claims are made about the validity of the measurements nor the model values based on this relationship, which solely scales the measurements in order to compare them with the salinity profile.

The data used in this study were collected between 10 and 16 March 2009 as part of a long-term experiment that lasted more than four months. During the time period used to compare the model results, the actual water level varied between 1.03 and 0.98 m (measured from the bottom) due to evaporation losses. In this study, we considered an initial water level of 1 m disregarding the variations of the true water level. The lights over the pond were turned on for 12 h per day. Water samples at different depths within the pond were withdrawn at the start of the measurements and on 16 March using sampling tubes installed at approximately 0.1-m intervals. These samples were used to determine the fluid density using a portable density meter (DA-110M, Mettler Toledo, Columbus, OH).

5.2.2 Numerical model

In this study, we modelled the laboratory data collected in the period from from 10 March, 9 AM LT, until 16 March 2009, 6 PM LT. The governing Navier-Stokes and transport equations were solved numerically with the SWASH free-surface Navier-Stokes model (Zijlema et al., 2011). The heating of the water by solar radiation and heat exchange across the boundaries were implemented in a thermal energy
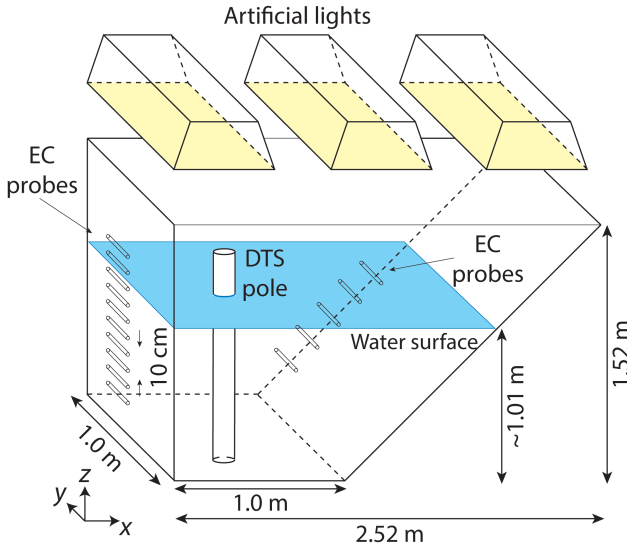
Figure 5.1: Diagram of the laboratory-scale solar pond, depicting the location of the EC electrodes and the vertical high-resolution DTS pole.

module, which coupled the heat increments with the temperature states in the transport model via source terms.

Free-surface Navier-Stokes model

SWASH was originally developed to simulate wave fields and rapidly varied flows in coastal waters. As such, the model code offers several advantages for the application in this study. First, the finite volume approach of SWASH applies terrain-following σ-layers, allowing cell depths to vary with the local water depth, both in space and in time. This allows an efficient implementation of the steep slope in the model set-up. Second, the model code allows the inclusion of wave run-up along the slope and dissipation of the wave's energy by applying a Sommerfeld radiation boundary condition. Third, the solution procedure guarantees conservation of mass and momentum, which is a requirement for the simulation of heat and mass transfer along the slope. Fourth, SWASH solves the Navier-Stokes equations for non-hydrostatic flow. This non-hydrostatic approach supports flow simulation in systems with large density gradients (Casulli and Stelling, 1998).

For the model structure and the governing equations, we refer to Zijlema et al. (2011). We did not include a turbulence model in our solution procedure, as low Reynolds numbers were generally found for the flow in shallow stratified ponds (Suárez et al., 2010b). We applied a relatively fine mesh to accurately solve the transport equations, allowing us to apply molecular values for the kinematic viscosity and diffusivity of salt and heat.

The applied mesh width was 1 cm. The cell depths were dependent on the local water depth and varied between 1.2 cm and 0 cm where the sloping bed reaches

the water surface. To accurately solve the transport equations, we applied a small time step of 2.5×10^{-3} s. The average computation time per hour of simulated time was ~8 h on three cores of an Intel Core i5-4670 processor. We consider such a long computation time necessary to maintain a small grid size, while having cell depths decreasing above the sloping wall toward 0 cm on the right boundary.

The selected procedure spatially discretizes the advective terms of the Navier-Stokes equations with a higher-order flux limiter scheme (Fringer et al., 2005): dissipative MINMOD flux limiters for the momentum equations, and MUSCL flux limiters for the transport equation. The remaining terms in the equations are spatially discretized with a central differences approach.

The horizontal time integration method for the momentum and transport equations is Euler explicit. For the solution of the horizontal advective terms in the momentum equations, the predictor-corrector scheme of MacCormack is applied (Hirsch, 1988). In vertical direction, the momentum equations are solved with a second-order Crank-Nicolson scheme and the transport equations are solved with a first-order Euler implicit scheme. For the time integration of the global continuity equation and the barotropic forcing in the horizontal momentum equation, the leapfrog scheme (Hansen, 1956) is applied.

At the free surface boundary, the non-hydrostatic pressure is defined as $q = 0$, and wind shear is neglected in the horizontal momentum equation because of the indoor environment. At the bottom boundary, the vertical velocity is derived from the kinematic condition for the local slope. A small bed friction defined by the smooth Chézy coefficient of 120 m$^{0.5}$/s was imposed for horizontal momentum, in order to impede high currents along the sloping bed. A Sommerfeld radiation boundary condition was selected for the potential wave run-up along the sloping bed. A fully reflective closed boundary was defined at the vertical wall. For the transport of heat and salt, a completely homogeneous Neumann boundary condition of gradient zero was applied at each boundary.

We extended the SWASH model code with some additional and modified modules. The general reason is that a solar pond has highly variable temperature and salinity states throughout the domain. Viscosities, diffusivities, and densities are in turn highly dependent on temperature and salinity. For the calculation of water density, ρ (kg m^{-3}), the Eckart formula in SWASH was replaced by the revisited Eckart formula (Wright, 1997), which is based on the UNESCO formula for water density (Unesco, 1981).

Giestas et al. (2009) stressed the importance of using temperature- and salinity-dependent viscosity values when modelling double-diffusive systems. We therefore extended SWASH with a module that calculates non-uniform kinematic viscosities based on the temperature and salinity states according to Equations 22 and 23 in Sharqawy et al. (2010).

Giestas et al. (1997) stressed the importance of non-uniform diffusivities in systems with large temperature and salinity gradients. Since we assume that molecular values for thermal and salt diffusivity can be applied in our case, we replaced the diffusivities in the SWASH transport module with temperature- and salinity dependent molecular diffusivities for heat and salt. These thermal and solutal diffusivities

(D_T and D_S, respectively, $m^2 s^{-1}$) are related to temperature, T (°C), and salinity, S (weight-%), by a linear regression on data presented in the International Critical Tables of Numerical Data, Physics, Chemistry and Technology (Washburn and West, 1933):

$$D_T = 1.3172{\cdot}10^{-7} + 4.2666{\cdot}10^{-10}{\cdot}T - 1.0924{\cdot}10^{-13}{\cdot}T^2 + 1.7405{\cdot}10^{-9}{\cdot}S - 3.1776{\cdot}10^{-11}{\cdot}S^2 \tag{5.1}$$

$$D_S = 7.6603{\cdot}10^{-10} + 2.3302{\cdot}10^{-11}{\cdot}T + 3.2197{\cdot}10^{-13}{\cdot}T^2 - 2.1829{\cdot}10^{-11}{\cdot}S + 1.3443{\cdot}10^{-12}{\cdot}S^2 \tag{5.2}$$

The modified transport module also includes so-called anti-creepage terms. These are additional diffusive terms in the transport equation, which follow from the full integration of the transport equation over the cell volume to guarantee mass conservation. The anti-creepage terms become relevant when the top and bottom cell faces are significantly inclined.

Thermal energy model

The thermal energy model describes the heating and cooling of the solar pond by incident and emitted LWR at the water surface, incoming SWR over the depth of the pond, and heat conductance over all the boundaries.

The incident and emitted LWR are described as in Henderson-Sellers (1986). However, as the solar pond is located indoor, some parameters have been modified. For the absorbed LWR, we write:

$$Q_{LWR;i} = (1 - A_{LWR}) \cdot \varepsilon_a \cdot \sigma \cdot T_a^4 \tag{5.3}$$

with the reflectivity $A_{LWR} = 0.03$ (-), emissivity ε_a (-), Stefan-Boltzmann constant $\sigma = 5.6697 \times 10^{-8}$ $W m^{-2} K^{-4}$, and the air temperature above the pond T_a (K). The emissivity ε_a for a concrete ceiling is assumed constant. A value of 0.95 was found convenient for our set-up, where literature suggests values of 0.85 to 0.95 for concrete slabs (Bilgen and Richard, 2002; Su et al., 2015). The emitted LWR is described assuming the water surface acts as a grey body emitter:

$$Q_{LWR;e} = -\varepsilon_w \cdot \sigma \cdot T_w^4 \tag{5.4}$$

with the water surface emissivity $\varepsilon_w = 0.972$ and the modelled water surface temperature T_w (K). The minus sign indicates heat loss.

The latent or evaporative heat flux is modelled according to Adams et al. (1990). For our indoor application, we assume negligible wind-forced convection. Hence, the latent heat flux is equal to the heat flux induced by free convection:

$$Q_{evap} = \begin{cases} -2.7 \cdot 10^{-2} \cdot (T_{wv} - T_{av})^{1/3} \cdot (e_{sw} - e_a) & T_{wv} > T_{av} \\ 0 & T_{wv} \leq T_{av} \end{cases} \tag{5.5}$$

with virtual water and air temperatures T_{wv} and T_{av} (K), respectively. The air vapor pressure e_a (Pa) and saturated vapor pressure at the water surface e_{sw} (Pa) are calculated according to Henderson-Sellers (1986):

$$e_a = \psi \cdot 2.1718 \cdot 10^{10} \cdot \exp\left(\frac{-4157}{T_a - 33.91}\right)$$

$$e_{sw} = 2.1718 \cdot 10^{10} \cdot \exp\left(\frac{-4157}{T_w - 33.91}\right)$$

where ψ is the relative humidity (-). The modelling approach only accounts for evaporation in terms of heat loss and does not account for the change in water volume.

The conductive heat flux across the water surface according to Thomann and Mueller (1987) consists of a wind-forced and free convective part as well (Kim and Chapra, 1997). Again, we only model the free convective part:

$$Q_{cond} = -c_1 \cdot 19.0 \cdot (T_w - T_a) \tag{5.6}$$

with Bowen's coefficient $c_1 = 62\,\mathrm{Pa\,K^{-1}}$.

For accurate modelling of the downward SWR extinction over the water column, the absorbed SWR is usually divided over multiple wavelength bands (Rabl and Nielsen, 1975; Branco and Torgersen, 2009; Suárez et al., 2010b). These studies employ extinction coefficients that are valid for solar radiation. Since we work with artificial lights that have a wavelength spectrum deviating from sun light, we have chosen to derive extinction coefficients that are specific for these artificial lights. Tsilingiris (1988) stressed that applying depth-varying extinction coefficients might improve the radiation extinction model for salt-gradient solar ponds. For calculation efficiency, we chose to divide our spectrum into three wavelength bands and to employ uniform extinction coefficients over depth.

We determined the extinction coefficients based on photon count data of an USB2000+ spectrometer and TP300-UV-VIS dip probe (both Ocean Optics, Dunedin, Florida) for the spectrum ranging from 350–1000 nm (Fig. 5.2). These data were published in Ruskowitz et al. (2014), but the current application demands an alternative analysis. We assume that photon numbers are applicable as a proxy for the SWR penetrating to a certain depth below the water surface. Based on information from the manufacturer of the lights, we expect that the measured spectral range mostly covers the spectral range of the SWR emitted by the artificial lights. For each wavelength, the photon numbers were normalized to the photon numbers at the water surface, before applying an exponential regression of the photon numbers over depth and wavelength.

Photon count data taken just above and just below the water surface displayed a strong dependence of the water surface reflectivity on wavelength (Fig. 5.3). For this reason, we use wavelength dependent surface reflectivities in the depth penetration model.

For our analysis, we divided the wavelength spectrum of the artificial lights into three bins (Table 5.1). Each of these bins was analysed for its average extinction coefficient μ and reflectivity A_{SWR} according to the SWR extinction model presented in Rabl and Nielsen (1975), which we modified to make the reflectivity wavelength dependent:
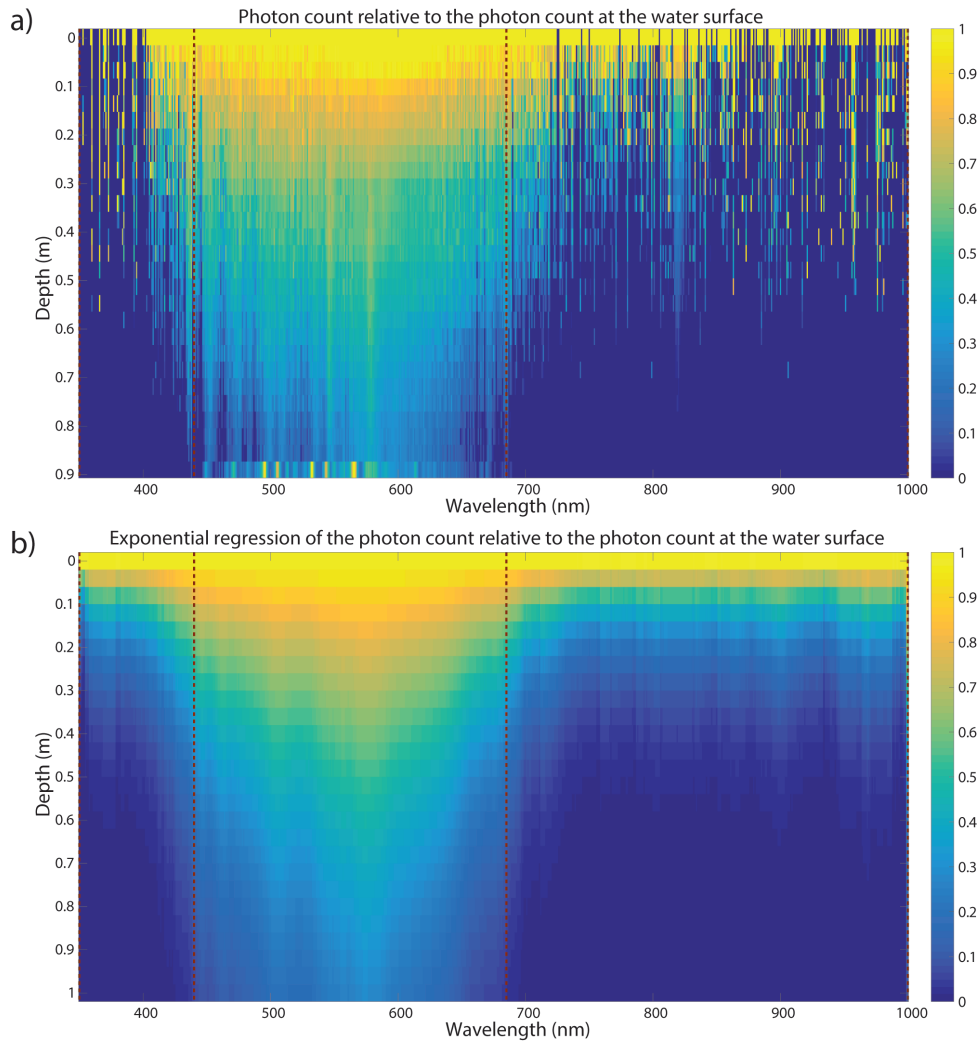
a) Photon count relative to the photon count at the water surface

b) Exponential regression of the photon count relative to the photon count at the water surface

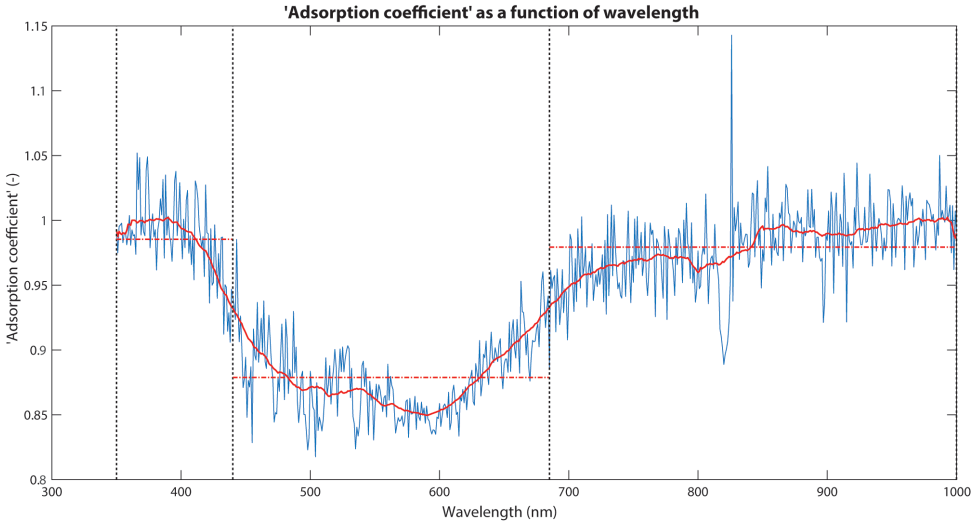Figure 5.2: Photon extinction data over depth before (**a**) and after (**b**) exponential regression

Figure 5.3: Spectral variation of the reflectivity based on photon count data

Table 5.1: Extinction coefficients μ (m^{-1}) and reflectivities A_{SWR} (-) for the artificial SWR divided over three ranges of wavelengths λ (nm), each representing η % of the total SWR penetrating the surface water body.

λ(nm)	A_{SWR} (-)	η (%)	μ (m^{-1})
350 - 440	0.015	5.54	6.43
440 - 685	0.121	71.75	1.89
> 685	0.021	22.71	7.21

$$Q_{SWR}(z) = Q_{SWR;0} \cdot \sum_{i=1}^{3} \left(1 - A_{SWR;i}\right) \cdot \frac{\eta_i}{100} \cdot \exp\left(-\mu_i \cdot z\right) \tag{5.7}$$

$Q_{SWR;0}$ is defined as 75 % of the measured incoming SWR, as 25 % is expected to be lost over the 10 cm between the sensor and the water surface.

Fig. 5.4 displays the percentages η of the total photon count that fall within each wavelength bin.

Besides conductive heat transfer over the water surface, we incorporated heat conduction through the pond's side walls and bottom:

$$Q_{wall} = \frac{T_w - T_{lab}}{c_r} \tag{5.8}$$

where T_{lab} (K) is the solar pond's ambient temperature. Based on literature values for the pond wall material, the conductive heat resistance factor c_r was estimated to 3.36 K m^2 W^{-1}, which makes it a good insulator.
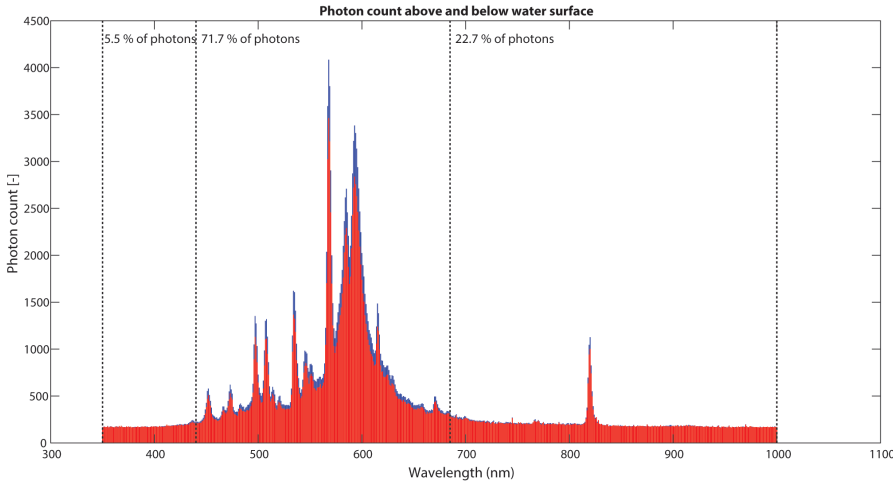
Figure 5.4: Division of the photon numbers over the three wavelength bins

Coupling the thermal energy and hydrodynamic transport model

Each time step Δt (s), the net thermal energy input for each grid cell is added as a source term in the transport equation according to its physical relationship:

$$\frac{\Delta T}{\Delta t} = \frac{Q_{LWR;i} + Q_{LWR;e} + Q_{evap} + Q_{cond} + Q_{SWR} + Q_{wall;ver}}{c \cdot \rho \cdot \Delta z} + \frac{Q_{wall;hor}}{c \cdot \rho \cdot \Delta x} \quad (5.9)$$

where a distinction is made between the vertical (ver) and horizontal (hor) wall conduction, as they should be divided over the cell depths (Δz) and cell widths (Δx), respectively. The variable specific heat capacity, c (J kg K^{-1}), is calculated from the temperature and salinity states. The dependence of c on temperature, T (°C), and salinity, S (weight-%), is found by a linear regression to data presented in the International Critical Tables of Numerical Data, Physics, Chemistry and Technology (Washburn and West, 1933):

$$c = 4184.92 + 2.05411 \cdot 10^{-1} \cdot T - 3.16068 \cdot 10^{-4} \cdot T^2 - 57.5177 \cdot S + 9.93871 \cdot 10^{-1} \cdot S^2 \quad (5.10)$$

5.3 Results and discussion

To allow intercomparison with the measurement data and investigate the hydrodynamics of the solar pond, model output was exported every five simulated minutes for water level, velocity, salinity, and temperature (Fig. 5.5). The steep water level gradient on the right side of Fig. 5.5a follows the sloping bed which crosses the water surface at this location. The dataset and its graphical representation in movies were published online (Hilgersom et al., 2016a).
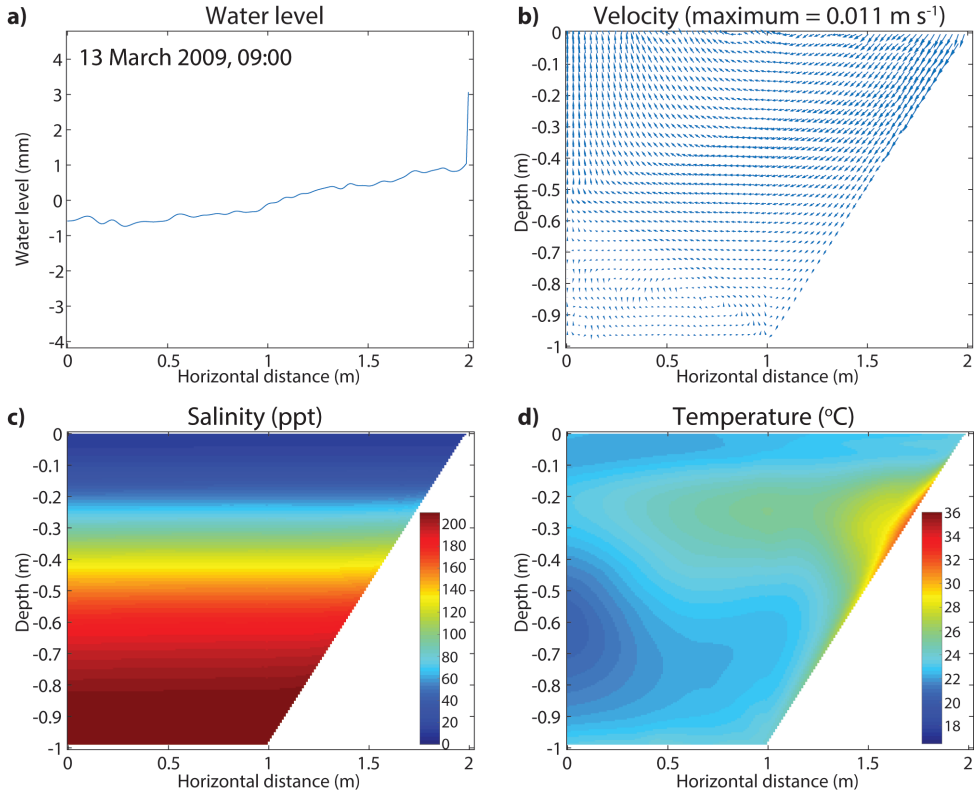
Figure 5.5: Model output after three days of simulation (13 March 2009, 09:00), with **a)** the water level, **b)** the velocity field, **c)** salinity, and **d)** temperature.

The modelled density flows induced oscillations in the water level, which were variably amplified and damped over time and reached a maximum excitation of 4 mm (Fig. 5.5a). These small seiches could neither be visually observed in the laboratory set-up nor be measured with the DTS pole, which had a maximum resolution of 1.1 cm, and previous hydrostatic simulations had given no indication of them. However, these seiches could actually occur in small ponds that are non-uniformly heated or have sloping side walls. When the water level excitation gets into the order of millimetres, the velocity profile is dominated by the wave-induced flow instead of double-diffusive convection cells (Fig. 5.5b).

When the velocity is not dominated by waves, we observe convection cells close to the sloping wall in the non-convective zone (Fig. 5.6). Although comparison of the modelled flow profiles with the actual flow profiles in the laboratory set-up is not possible, we hypothesize that the transition between convective and wave-induced flows is a merit of the non-hydrostatic model. Unfortunately, intercomparison with previous modelling studies (Suárez et al., 2010b, 2014) can not confirm this hypothesis, as different results may be both attributed to the sloping wall and the
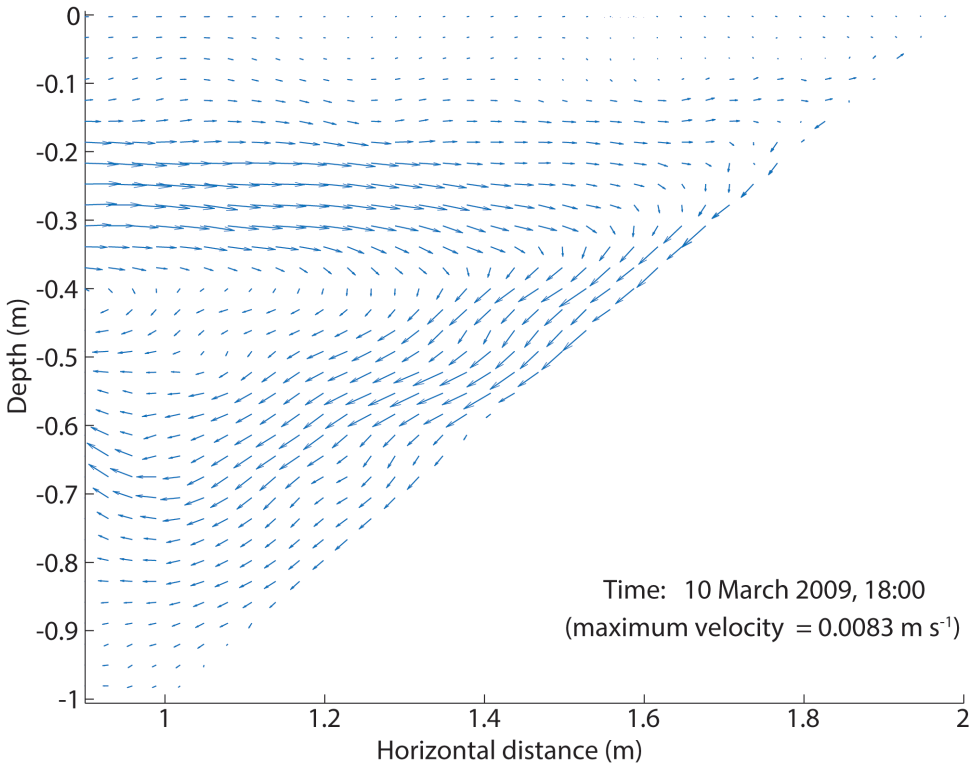
Figure 5.6: Example of a velocity plot (10 March 2009, 18:00 LT). The locations of the convection cells near the slope were highly variable over time.

hydrodynamics included in the model.

The observed convection patterns in the NCZ are in disagreement with the hypothesized functioning of a solar pond, where convection cells occur in the UCZ and LCZ. The flows through the NCZ transport additional salt and heat through this zone and can therefore be an additional mixing mechanism, which impedes the optimal functioning of the pond. Interestingly, the observed convection cell has a discontinuous shape at ~8 cm right of the start of the slope. Here, the water seems to flow around the warm water cell near the slope, which does not yet extend completely downward along the slope at this time.

The effect of the additional mixing mechanism is illustrated by the modelled salinity profile over depth (Fig. 5.7). The corresponding salinity measurements also display an erosion of the salinity profile, although less pronounced than the model results. In the initial salinity profile, the measured salinity and the salinity inverted from EC measurements using the linear conversion factor compare well for the extreme salinities. However, there is a slight deviation for the moderate salinities. No conclusive statements can be made whether these are caused by the conversion method or by measurement errors.

5

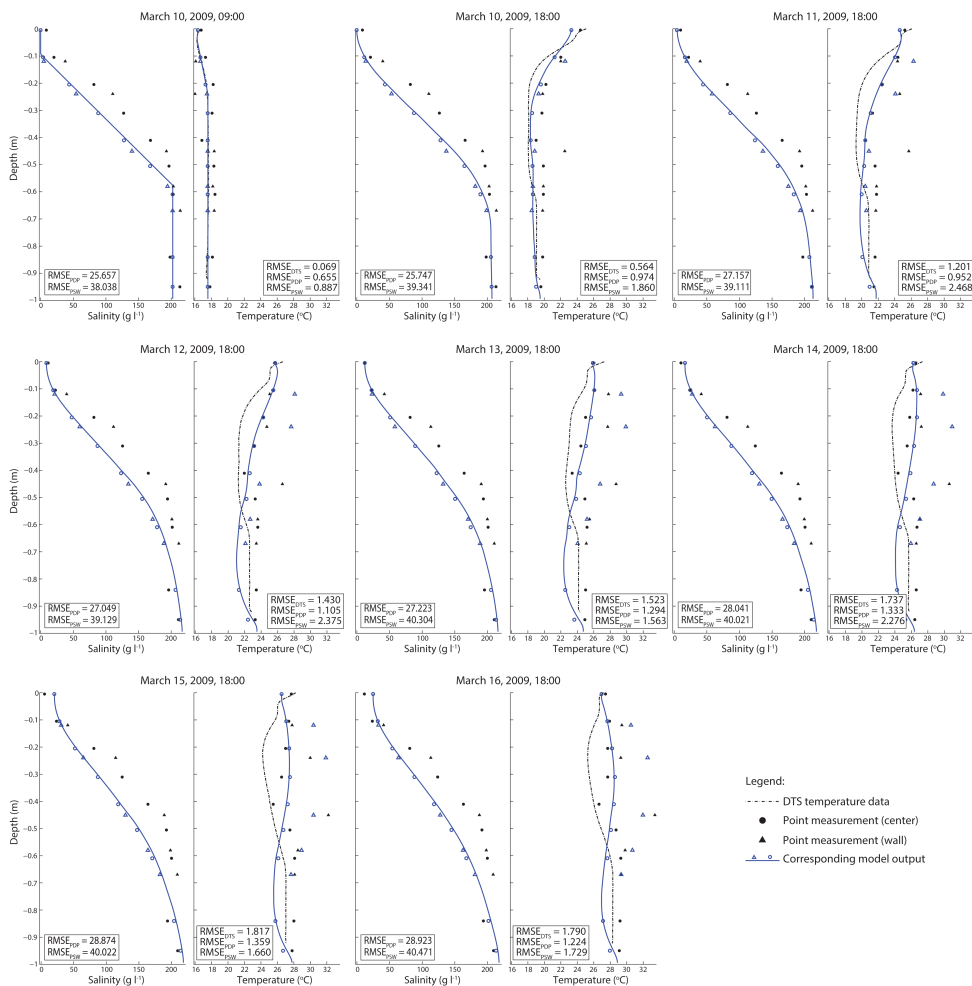Temporal evolution of the salinity and temperature depth profiles

Figure 5.7: Evolution of the measured and modelled salinity and temperature depth profiles over time. The root mean squared errors compare the measurement and model data for the DTS measurements ($RMSE_{DTS}$), the point measurements in the deep pond section ($RMSE_{PDP}$), and the point measurements along the sloping wall ($RMSE_{PSW}$).
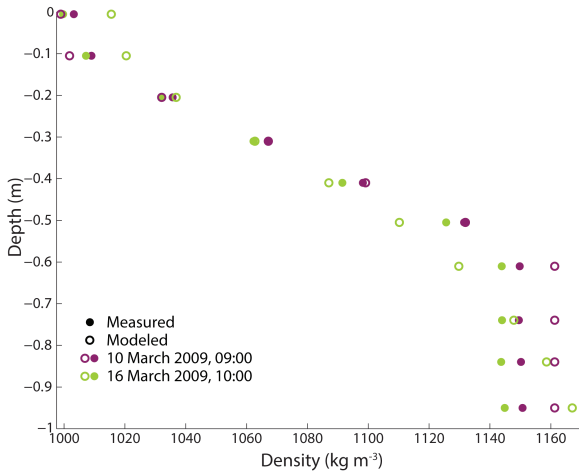
Temporal evolution of the density depth profile

Figure 5.8: Evolution of the measured and modelled density profiles over time.

For this reason, we also compare the measured and modelled density profiles at the start and after 6 d (Fig. 5.8). The initial density profile compares well to the measured profile, although the model slightly overestimates the density in the LCZ. This is most probably caused by the less accurate conversion of salinity and temperature to density at very high salinities by the revisited Eckart formula (Wright, 1997). As was also shown by the salinity profiles, the measured and modelled high-density layer in the LCZ is partly eroded after six days, with the salinity gradient extending to the bottom of the pond. Fig. 5.8 confirms the higher decrease in salinity in the model results compared to the measurements, especially in the top part of the LCZ. This suggests that the LCZ in the model does not develop as it does in the measurements. On the other hand, the measurements do show a slight erosion of the salinity in the upper part of the LCZ. Therefore, it seems that the model exaggerates the convective transport of salt and heat along the sloping bed. However, these processes are actually occurring, either as a consequence of the observed convection cells near the sloping wall or the small seiche that occurred in the model.

The evolution of the complete pond temperature field confirms the large heat transport along the sloping wall (Fig. 5.9). These higher temperatures are also observed from the point measurements along the sloping wall, which mostly agree well with the model results at these locations (Fig. 5.7). In general, the temperatures near the wall were slightly overestimated by the model at shallow depths, and underestimated at half depth. The spatially variable illumination of the water surface by the three lamps could have introduced additional uncertainty near the edges of the pond.

Fig. 5.10 shows that the modelled heat storage in the LCZ largely agrees with the DTS measured heat storage. During daytime, however, the measured heat
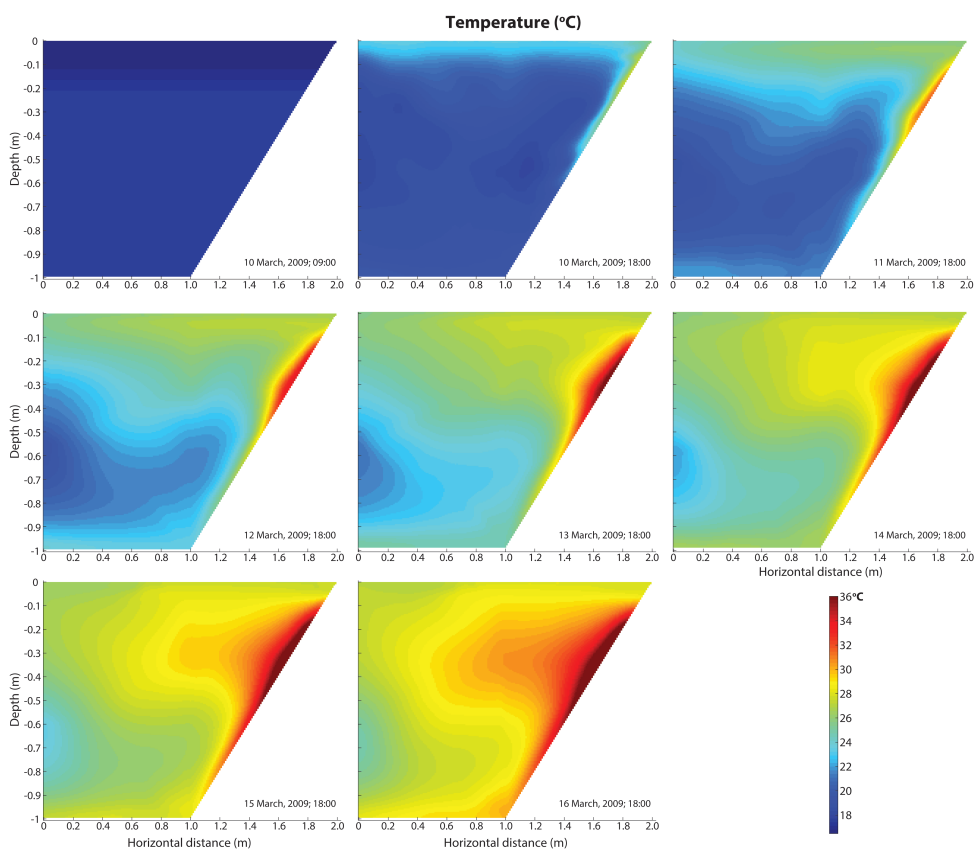
Figure 5.9: Evolution of the temperature field in the solar pond over time.
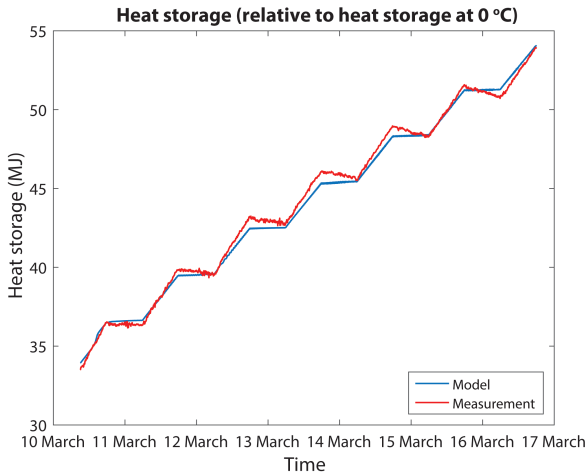
Figure 5.10: Measured and modelled heat storage in the LCZ over time. The LCZ is defined as the lower 0.4 m of the pond, and the measured heat storage is calculated from the DTS measurements by assuming a uniform horizontal temperature distribution.

storage increases faster than the modelled heat storage. This is consistent with the exaggerated heat transport along the slope in the model. During night time, the smaller heat increment in the model is compensated by a lower heat conduction to the NCZ and through the walls.

The influence of the slope extends above the flat bed, as displayed by the horizontal variation in temperature in this part of the pond (Fig. 5.9). For this reason, the DTS temperature measurements and the central point measurements deviate as well, since the DTS measurements were taken closer to the left vertical wall (Fig. 5.7). Both the model and measurements show lower temperatures in the NCZ at the DTS pole location, which was less affected by the sloping wall.

Deviating temperatures could also be caused by the position of the point measurements near one of the parallel side walls, whereas the DTS sensor was located more than 20 cm from a side wall. This would suggest that variations in the y-dimension could also play a role in the modelling study. Although a 3-D modelling approach could account for these variations, it would be unnecessarily computational expensive as it is believed that 2-D models are able to capture the general structure of double-diffusive convective systems (Molemaker and Dijkstra, 1997).

In general, the performance of the central temperatures in the model is good compared to the point measurements (Fig. 5.7). In the LCZ, the modelled temperatures remain slightly lower, which could be explained by the heat transport along the slope in the model. However, in the NCZ and UCZ the point measurements compare well with the model data. The point measurement at ~0.4-m depth is generally slightly lower than the model predictions and the other point measurements. Suárez et al. (2011) have shown that this probe, which was made of epoxy whereas the others were made of glass, consistently measures deviating temperatures.

Comparison between the DTS data and the corresponding model data confirms the behavior of the LCZ that was observed in the previous comparison with the point measurements. However, this comparison also shows a difference in heating of the upper part of the NCZ in the model. It is unlikely that the temperature variations at this level are so substantial because of the sensor positioning in the y-dimension. Therefore, these results seem to support that the sloping wall influences the temperature pattern in x-dimension.

The horizontal variations in temperature due to transport along the sloping wall also cause a cold spot near the left vertical wall (Fig. 5.9). The cold spot extends into the LCZ, but starts to heat up from below after several days. The delayed heating of the LCZ at this location seems a consequence of the heat transport along the slope. This zone apparently starts functioning as expected only after a few days when local convection makes the temperature in the LCZ more uniform. Presumably, this process would start earlier if a larger fraction of the solar pond has a flat bottom.

5.4 Conclusions

A free-surface Navier-Stokes model was set up to simulate a laboratory scale solar pond with a sloping side wall. The SWASH model was selected to facilitate mass conserving calculations in a terrain-following mesh, including wave run-up along the sloping wall, where the cell depths decrease toward 0 cm. The non-hydrostatic approach supports the simulation of large density gradients and double-diffusive convection.

In general, the model performed well, although the transport of heat and salt along the sloping side wall was overestimated compared to measured data. Nevertheless, the measurement data did capture the upward flow of warm water along the slope as well. Both the measurements and model data showed an increased warming of the upper part of the NCZ that extended above the flat bottom of the solar pond. Because half the pond bed was sloping in this set-up, we expect that the influence of the slope on the thermal profile in the pond is large and will decrease when the fraction of the sloped pond bed to the total bed surface decreases.

Small seiches occurred during parts of the modelling period, resulting in a maximum water level excitation of 4 mm. Although these waves could not be physically observed in the solar pond, their presence is not unthinkable in a pond that is heated non-uniformly and has a buoyant flow along its sloping wall. Therefore, the results of this free-surface modelling study could have important implications for the mixing and stability of these ponds with a sloped wall. The seiches and the side slope-induced convection reduced the magnitude of the salt gradient toward the LCZ, consequently reducing its effectiveness. Because the operation of solar ponds relies on suppressed mixing processes, understanding these seiches is important and further study of this phenomenon is recommended.

With the occurrence of seiches, the free-surface model identified an issue which potentially disrupts the functioning of a solar pond, and which could not be observed from the laboratory measurements and previous studies with a rigid-lid approach. Besides qualitative conclusions, however, the added value of the free-surface modelling approach is difficult to quantify. Comparison with previous modelling studies

for this solar pond (Suárez et al., 2010b, 2014), which also demonstrated good results, does not provide strong conclusions about the added value, because these studies did not include a sloping side wall which strongly affects the results. Qualitatively, we can state that this modelling approach results in explainable flow profiles in a system with large density gradients that largely reproduce our observations.

New coefficients for the SWR extinction model by Rabl and Nielsen (1975) were derived for the artificial lights that were used in the indoor environment. We describe a new approach for the inversion of the extinction coefficients and the fractions of the wavelength spectrum for which they apply from photon count data taken over the complete depth of the solar pond. The extinction coefficients deviate from those reported for solar radiation. We argue that the small deviations in the heating of the LCZ are mainly caused by the buoyant transport along the slope, which counteracts the development of convection in the LCZ, rather than errors introduced by the shortwave radiation extinction model.

In all, the developed model provides insight into the dynamics of a solar pond with a sloping wall. The free-surface modelling approach revealed the importance of wave dynamics and convective transport near the slope for the development of the temperature profile over depth.

5

6

An axisymmetric non-hydrostatic model for double-diffusive water systems

The three-dimensional (3-D) modelling of water systems involving double-diffusive processes is challenging due to the large computation times required to solve the flow and transport of constituents. In systems that approach axisymmetry around a central location, computation times can be reduced by applying a quasi 3-D axisymmetric model set-up. This chapter applies the Navier-Stokes equations described in cylindrical coordinates, and integrates them to guarantee mass and momentum conservation. The discretized equations are presented in a way that a Cartesian finite volume model can be easily extended to this quasi 3-D framework, which is demonstrated by the implementation into a non-hydrostatic free-surface flow model. This model employs temperature and salinity dependent densities, molecular diffusivities, and kinematic viscosity. Four qualitative case studies demonstrate a good behaviour with respect to the expected double-diffusive processes and the resulting density-driven flows in shallow water bodies. A fifth case study involves a new validation method that quantifies the radial expansion of a dense water layer developing from a central inflow at the bottom of a shallow water body.

6.1 Introduction

Over the past decades, numerical salt and heat transport models have increased their capability to capture patterns of double-diffusion on scales varying from laboratory set-ups to the ocean (Yoshida and Nagashima, 2003; Kunze, 2003). Despite the advance in computation power and parallel computing, the requirement of dense grids for the three-dimensional (3-D) modelling of salt and heat transport often yields unacceptable computation times. In this chapter, we present a framework for a quasi 3-D finite volume approach that allows free-surface flow modelling in an axisymmetric grid. The model framework is intended for a shallow water body where salinity and temperature gradients potentially induce double-diffusive processes. As such, the model intends to simulate larger-scale features of double-diffusion (i.e., interface locations in a stratified system and heat and salt transport).

Kunze (2003) stresses that numerical and analytical methods to model double-diffusion often only apply at specific scales. For example in oceans, internal wave-shear and strain enhance salt-finger growth, leading to higher salt and heat fluxes over stratified interfaces. Traxler et al. (2011) addresses the issue of scale by describing four modes of instability in salt-fingering systems, which play a role on different scales. Their 3-D simulations of large-scale instability in salt-fingering systems are the first known successful direct numerical simulations (DNS). Carpenter et al. (2012) were among the first to model systems in the double-diffusive convection regime with 3-D DNS. Their detailed simulations showed that, in this regime, the salt and heat fluxes across the interface are largely governed by molecular diffusion and that these salt and heat diffusion rates control the thickness of the salt and heat interface, respectively. Kimura and Smyth (2007) used 3-D DNS to model salt sheets for a double-diffusively stratified flow interacting with inflectional shear.

Yoshida and Nagashima (2003) have shown that 2-D numerical models are already well able to simulate small-scale processes in laboratory set-ups. On a larger scale, Sommer et al. (2014) confirm the findings of Carpenter et al. (2012) with 2-D DNS and high-resolution measurements of a double-diffusive staircase in Lake Kivu for density ratios larger than three, noting that in these systems external turbulence by shear or internal waves should be absent to maintain diffusion as the main driver for salt and heat transport. Noguchi and Niino (2010a,b) used 2-D DNS to study the spontaneous layer formation in the double-diffusive convection regime and explores the layer formation from the non-linear evolution of disturbances.

Most numerical modelling studies of double-diffusive processes calculate interfaces and salt and heat fluxes at oceanic scale (Stommel and Fedorov, 1967; Stern, 1967; Ruddick and Gargett, 2003; Kelley et al., 2003; Kunze, 2003; Kimura et al., 2011). This can be explained by the ubiquity of these systems in oceans (Huppert and Turner, 1981), and by the potential of oceanic thermohaline stratification as an energy source (Stommel et al., 1956; Vega, 2002). These larger-scale simulations are commonly performed with Reynolds-averaged Navier-Stokes (RANS) models. For example, Radko et al. (2014a,b) successfully applied a 3-D RANS model to an oceanic scale salt-finger staircase. Recently, modelling of these phenomena in smaller-scale water bodies has started to be developed. For example, double-diffusive processes like thermohaline staircasing have been successfully modelled

in lakes (Schmid et al., 2003), although these systems are generally modelled with analytical or empirical formulations (Kelley et al., 2003; Schmid et al., 2004; Arnon et al., 2014a). Other known numerical modelling studies consider double-diffusive convection in monitoring wells (Berthold and Börner, 2008), and the collection of thermal energy in solar ponds (Cathcart and Wheaton, 1987; Giestas et al., 2009; Suárez et al., 2010b, 2014). However, modelling these complex physical processes in shallow waters still imposes a major scientific and computational challenge (Dias and Lopes, 2006).

Axisymmetric CFD models are applied in a wide variety of fields. Examples of applications include the modelling of flow of gas past a gravitating body in astronomy (Shima et al., 1985), radiative heat transfer in cylindrical enclosures (Menguc and Viskanta, 1986), the heating of air flowing through a combustion burner (Galletti et al., 2007), and acoustic axisymmetric waves in elastic media (Schubert et al., 1998). The similarity between these examples is that a model calculating in two spatial dimensions models 3-D processes due to axisymmetry. In geohydrology, axisymmetric models are often applied for groundwater flow around injection and abstraction wells (Bennett et al., 1990). Groundwater modelling software often offers code extensions that adjust several input parameters to allow such modelling approaches (Reilly and Harbaugh, 1993; Langevin, 2008).

In some cases, axisymmetric grid set-ups can also be preferential for hydrodynamic surface water models. Examples of such cases are close-to-circular water bodies with uniform boundaries, and the flow around a central point (e.g., a local inflow from a pipe or groundwater seepage). The occurrence of local saline seepage inflows into shallow water bodies of contrasting temperatures has been described by De Louw et al. (2013). Hilgersom et al. (2016c) has shown how these local inflows can induce thermohaline stratification in the shallow surface water bodies above these inflows.

This chapter derives a framework for an axisymmetric free-surface RANS model, which is implemented in SWASH. SWASH is an open source non-hydrostatic modelling code for the simulation of coastal flows including baroclinic forcing (SWASH source code (Version 1.20), 2011). It is suitable for the simulation of flows and transport in varying density fields, because 1) the staggered grid allows a momentum and mass conservative solution of the governing equations, which is required for accurate salt and heat transport modelling, and 2) the non-hydrostatic pressure terms aid the simulation of flows in fields with large density variations. Another major advantage of SWASH is the flexible and easily extendible code, which can be applied for free under the GNU GPL license. Other properties of SWASH are the opportunity to apply terrain-following σ-layers for the definition of cell depths and the user-friendly pre- and post-processing.

The development of an axisymmetric variation of SWASH falls in line with our research to localized saline water seepage in Dutch polders. To simulate the effect of a local seepage inflow on the temperature profile of the surface water body, a numerical model is required that accounts for sharp density gradients, a free surface and potential double-diffusive processes. The axisymmetric grid set-up aids in correctly representing the volumetric inflow and modelling the flow processes

6

around the local inflow.

In this chapter, we present the resulting numerical framework to extend a 2-D finite volume model into a quasi 3-D model by adding few terms to the solution of the governing Navier-Stokes and transport equations. These terms are implemented in the SWASH code. The model code is further extended with a new transport module calculating salt and heat transfer. Although the model generally calculates with a mesh size that is larger than the size required to solve small-scale double-diffusive instabilities, the aim is to allow the model to approximate interface locations and salt and heat fluxes. The functioning of the code is validated with case studies involving different salinity and temperature gradients.

6.2 Method

6.2.1 Governing equations

The governing equations in this study are the Navier-Stokes equations for the flow of an incompressible fluid, derived in cylindrical coordinates (r, α, z) (Batchelor, 1967). Due to point symmetry, the gradients in tangential direction (α) are set to zero, which leaves the solution of the equations in one horizontal and one vertical dimension (i.e., 2-DV):

$$\frac{1}{r}\frac{\partial ur}{\partial r} + \frac{\partial w}{\partial z} = 0 \tag{6.1}$$

$$\frac{\partial u}{\partial t} + \frac{\partial uu}{\partial r} + \frac{\partial wu}{\partial z} = -\frac{1}{\rho}\frac{\partial p}{\partial r} + \left(\frac{1}{r}\frac{\partial}{\partial r}\left(v_h r \frac{\partial u}{\partial r}\right) - \frac{v_h u}{r^2} + \frac{\partial}{\partial z}\left(v_v \frac{\partial u}{\partial z}\right)\right) \tag{6.2}$$

$$\frac{\partial w}{\partial t} + \frac{\partial uw}{\partial r} + \frac{\partial ww}{\partial z} = -\frac{1}{\rho}\frac{\partial p}{\partial z} + \frac{1}{r}\frac{\partial}{\partial r}\left(v_h r \frac{\partial w}{\partial r}\right) + \frac{\partial}{\partial z}\left(v_v \frac{\partial w}{\partial z}\right) - g \tag{6.3}$$

In these equations, r represents the horizontal axis in radial direction and z the vertical axis, with u and w the velocities along these axes, respectively. The density ρ is calculated from the local temperature and salinity states by the updated Eckart formula (Eckart, 1958; Wright, 1997), which is based on the UNESCO IES80 formula (Unesco, 1981).

In this RANS model, turbulence is modelled with the standard k-ϵ model (Launder and Spalding, 1974). The modelled eddy viscosity is added to the molecular viscosity, yielding a non-uniform vertical viscosity v_v. For the calculations in this thesis, the horizontal kinematic viscosity v_h is set uniform to its molecular value ($\sim 10^{-6}\,\mathrm{m^2\,s^{-1}}$).

The pressure terms are split into hydrostatic and hydrodynamic terms, according to Casulli and Stelling (1998):

$$\frac{1}{\rho}\frac{\partial p}{\partial r} = \frac{g}{\rho}\frac{\partial \int_{z'=z}^{\zeta} \rho\,(r, z', t)\,dz'}{\partial r} + \frac{\partial q}{\partial r} \tag{6.4}$$

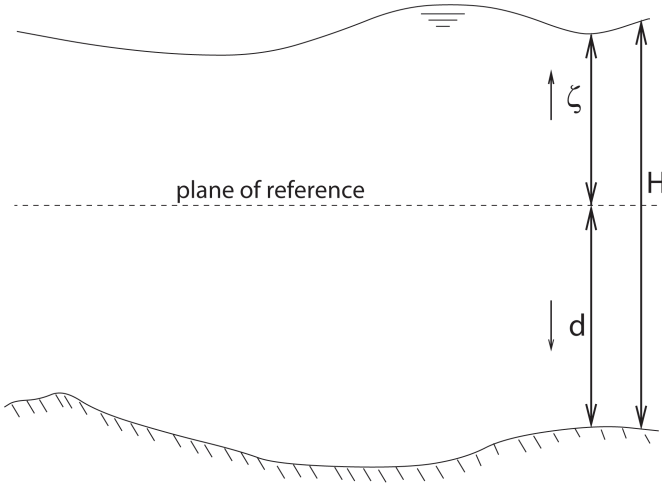$$\frac{1}{\rho}\frac{\partial p}{\partial z} + g \equiv \frac{\partial q}{\partial z} \tag{6.5}$$

Figure 6.1: Definition of the free surface level ζ and the bottom level d (Zijlema and Stelling, 2005).

where q denotes the hydrodynamic pressure component and ζ the local free surface level relative to the reference plane (Fig. 6.1). Horizontal variations in atmospheric pressure are neglected. The first right-hand side term of Eq. 6.4 is split into baroclinic and barotropic components when the equations are integrated over the cell depth in Section 6.2.3. In the vertical, the baroclinic pressure gradient and the gravitational acceleration cancel each other out, leaving the hydrodynamic pressure gradient (Eq. 6.5).

The free surface is calculated according to Zijlema and Stelling (2008), by integrating Eq. 6.1 over the depth of the water column:

$$y \cdot \frac{\partial \zeta}{\partial t} + \frac{\partial Q}{\partial t} = 0$$
$$Q \equiv UHy = \int_{y_0}^{y_1} \int_{-d}^{\zeta} u \, dz \, dy \tag{6.6}$$

where U is the depth-averaged velocity, and d is the local bottom depth (Fig. 6.1).

Transport of mass and heat is calculated with the convection-diffusion equation:

$$\frac{\partial c}{\partial t} + \frac{1}{r} \frac{\partial ruc}{\partial r} + \frac{\partial wc}{\partial z} = \frac{1}{r} \frac{\partial}{\partial r} \left(D_h r \frac{\partial c}{\partial r} \right) + \frac{\partial}{\partial z} \left(D_v \frac{\partial c}{\partial r} \right) \tag{6.7}$$

where the concentration c represents either the salinity S or temperature T.

To account for vertical turbulent diffusion, D_v is calculated by adding the molecular diffusivity and turbulent diffusivity: $D = D_{mol} + D_{turb}$. The turbulent diffusivity is calculated by dividing the eddy viscosity v_{turb} by the turbulent Prandtl number ($Pr = 0.85$) in the case of heat transport, or by the turbulent Schmidt number ($Sc = 0.7$) in the case of salt transport:

$$D_{turb;T} = \frac{\nu_{turb}}{Pr} = \frac{\nu_{turb}}{0.85} \qquad (6.8)$$

$$D_{turb;S} = \frac{\nu_{turb}}{Sc} = \frac{\nu_{turb}}{0.7} \qquad (6.9)$$

with $D_{turb;T}$ and $D_{turb;S}$ being the thermal and solutal turbulent diffusivities in $m^2\,s^{-1}$, respectively.

In non-turbulent thermohaline systems, stability largely depends on density gradients and molecular heat and salt diffusion rates, which in turn are highly dependent on temperature and salinity. The heat and salt diffusivities are related to temperature T (°C) and salinity S (weight-‰) by a quadratic regression on data presented in the International Critical Tables of Numerical Data, Physics, Chemistry and Technology (Washburn and West, 1933):

$$D_{mol;T} = 1.31721 + 4.26657 \cdot 10^{-3} \cdot T - 1.09237 \cdot 10^{-6} \cdot T^2 + 1.74051 \cdot 10^{-2} \cdot S - 3.17759 \cdot 10^{-4} \cdot S^2 \qquad (6.10)$$

$$D_{mol;S} = 7.66025 + 2.33023 \cdot 10^{-1} \cdot T + 3.21974 \cdot 10^{-3} \cdot T^2 - 2.18290 \cdot 10^{-1} \cdot S + 1.34431 \cdot 10^{-2} \cdot S^2 \qquad (6.11)$$

6.2.2 Boundary conditions

At the free surface, we assume no wind and $q|_{z=\zeta} = 0$. At the bottom boundary, the vertical velocity is calculated by imposing the kinematic condition $w|_{z=-d} = -u\partial d/\partial r$. The presented case studies (Section 6.3) include a local seepage inflow at the bottom boundary, for which the seepage velocity is added to the kinematic condition. For horizontal momentum, the bottom friction is imposed by the logarithmic wall law, where a Nikuradse roughness height determines the amount of friction (Launder and Spalding, 1974).

A special case is the inner boundary, where symmetry occurs: for all variables, the gradient is set to zero, except for horizontal momentum: $u|_{r=0} = 0$. For the presented case studies, we define a Dirichlet boundary condition for u momentum at the outer boundary, where the total outflow is equated to the instantaneous seepage inflow.

For the transport equation, a homogeneous Neumann boundary condition is defined at each boundary ($\frac{\partial cr}{\partial r} = 0$ and $\frac{\partial c}{\partial z} = 0$), except at a defined seepage inflow of known temperature and salt concentration, where a Dirichlet boundary condition is imposed.

6.2.3 Numerical framework and implementation

The physical domain is discretized with a fixed cell width in radial direction. The width of the cells in the tangential direction increases by a fixed angle α, which allows us to consider the horizontal grid as a pie slice (Fig. 6.3). In the model, α could be assigned any value (i.e., also 2π for a completely circular grid). However,
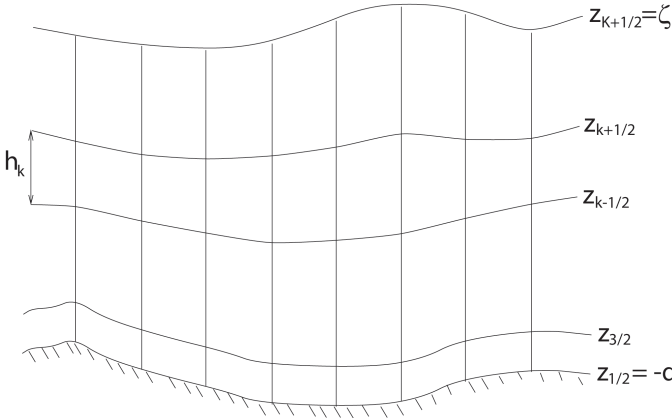
Figure 6.2: Vertical grid definition (sigma layers) (Zijlema and Stelling, 2005)
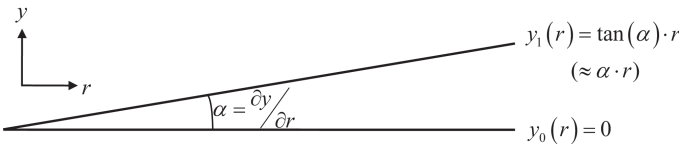

Figure 6.3: Axis definition

to allow a simple presentation of the integration step in this subsection, we consider α as a small angle.

For the vertical grid, sigma layering is employed, although part of the layers can be defined by a fixed cell depth (Fig. 6.2). A classical staggered grid is applied with velocities defined at the cell boundaries and the other states in the cell centre.

For reasons of momentum and mass conservation, Zijlema and Stelling (2005) integrated the governing equations over the cell depth using the Leibniz integral rule (Appendix A). In our case, the cell width in tangential direction varies as well. Therefore, the equations are integrated over the cell depth and the width in tangential direction, which is in this case defined as the y-dimension. For the continuity equation, this yields (cf. Fig. 6.2 and 6.3):

$$\int_{z_{k-\frac{1}{2}}}^{z_{k+\frac{1}{2}}} \int_{y_0}^{y_1} \left(\frac{1}{r}\frac{\partial ur}{\partial r} + \frac{\partial w}{\partial z} \right) dydz = \frac{\partial \phi_k y_1}{\partial r} + y_1 \omega_{k+\frac{1}{2}} - y_1 \omega_{k-\frac{1}{2}} + y_1 \frac{\partial h_k}{\partial t} = 0 \quad (6.12)$$

with $\phi_k = u_k \cdot h_k$ is the cell depth integrated velocity and the relative vertical velocity ω as defined in Eq. 16 of Zijlema and Stelling (2005).

The momentum equations and the transport equation are integrated in a similar fashion:

$$\overline{y_1}^r \frac{\partial u_k \overline{h_k}^r}{\partial t} + \frac{\partial \overline{\phi_k}^r \hat{u}_k \overline{y_1}^r}{\partial r} + \overrightarrow{y_1} \hat{u}_{k+\frac{1}{2}} \overline{\omega_{k+\frac{1}{2}}}^r - \overrightarrow{y_1} \hat{u}_{k-\frac{1}{2}} \overline{\omega_{k-\frac{1}{2}}}^r - \boxed{\alpha \phi_k u_k} + g \overline{h_k}^r \overline{y_1}^r \frac{\partial \zeta}{\partial r} +$$

$$\frac{\partial q_k h_k y_1}{\partial r} - \overline{y_1}^r \overline{q}^{rz} \frac{\partial z_{i+\frac{1}{2},k+\frac{1}{2}}}{\partial r} + \overline{y_1}^r \overline{q}^{rz} \frac{\partial z_{i+\frac{1}{2},k-\frac{1}{2}}}{\partial r} - \boxed{\alpha \overline{h_k}^r \overline{q_k}^r} + \overline{y_1}^r \frac{g}{\overline{\rho_k}} \frac{\partial \overline{\rho_k}}{\partial r} \frac{\left(\overline{h_k}^r\right)^2}{2} +$$

$$\frac{g \overline{h_k}^r \overline{y_1}^r}{\overline{\rho_k}} \sum_{j=1}^{k-1} \left(\overline{h_j}^r \frac{\partial \overline{\rho_j}}{\partial r} + (\overline{\rho_j} - \overline{\rho_k}) \frac{\partial h_j}{\partial r} \right) - \frac{\partial}{\partial r} \nu_h h_k y_1 \frac{\partial \overline{u_k}}{\partial r} +$$

$$\boxed{\alpha h_k u_k \frac{\nu_h}{r}} - \overline{y_1}^r \left[\nu_v \frac{\partial u}{\partial z} \right]_{k-\frac{1}{2}}^{k+\frac{1}{2}} = 0$$

(6.13)

$$y_1 \frac{\partial \overline{w_{k+\frac{1}{2}} h_{k+\frac{1}{2}}}^z}{\partial t} + \frac{\partial \overline{\hat{w}_{k+\frac{1}{2}} \phi_{k+\frac{1}{2}}}^z y_1}{\partial r} - \boxed{\alpha \overline{\phi_{k+\frac{1}{2}}}^{rz} w_{k+\frac{1}{2}}} + y_1 \hat{w}_{k+1} \overline{\omega_{k+1}}^z - y_1 \hat{w}_k \overline{\omega_k}^z +$$

$$y_1 q_{k+1} - y_1 q_k - \frac{\partial}{\partial r} \nu_h \overline{y_1}^r \overline{h_{k+\frac{1}{2}}}^{rz} \frac{\partial \overline{w}}{\partial r} - y_1 \left[\nu_v \frac{\partial w}{\partial z} \right]_k^{k+1} = 0$$

(6.14)

$$y_1 \frac{\partial c_k h_k}{\partial t} + \frac{\partial \phi_k c_k y_1}{\partial r} + y_1 \omega_{k+\frac{1}{2}} \hat{c}_{k+\frac{1}{2}} - y_1 \omega_{k-\frac{1}{2}} \hat{c}_{k-\frac{1}{2}} - \frac{\partial}{\partial r'} \left\{ D_h \overline{y_1}^r \overline{h_k}^r \frac{\partial c}{\partial r'} \right\} -$$

$$y_1 \left[D_v \frac{\partial c}{\partial z'} \right]_{z_{k-\frac{1}{2}}}^{z_{k+\frac{1}{2}}} + \frac{\partial}{\partial r'} \left\{ D_h \overline{y_1}^r \overline{h_k}^r \frac{\partial \overline{c_k}^r}{\partial z'} \frac{\partial \overline{z}^z}{\partial r'} \right\} + y_1 \left[D_h \frac{\partial z_k}{\partial r} \frac{\partial c}{\partial r'} \right]_{z_{k-\frac{1}{2}}}^{z_{k+\frac{1}{2}}} -$$

$$y_1 \left[D_h \left(\frac{\partial z}{\partial r} \right)^2 \frac{\partial c}{\partial z'} \right]_{z_{k-\frac{1}{2}}}^{z_{k+\frac{1}{2}}} = 0$$

(6.15)

where overlined variables denote spatially averaged values for these variables in r or z directions, and arrows denote the use of values from downstream cells. The boxes mark the *alpha terms*, which mark the additional angular terms compared to the 2-DV solutions for the momentum equations in Cartesian coordinates. In the integrated transport equation (Eq. 6.15), the latter three terms on the left-hand side are the so-called anti-creepage terms, which should be incorporated for the calculation of transport when large gradients in water depth occur.

Since u and w are the primitive variables in the momentum equations, and not uh and wh as in Eq. 6.13 and 6.14, we further rewrite the momentum equations according to Zijlema and Stelling (2008). In order to do this for the u momentum equation, we first spatially discretize the continuity equation in point $i+\frac{1}{2}$:

$$\overline{y_{1;i+\frac{1}{2}}}^r \frac{\partial \overline{h}_{i+\frac{1}{2},k}^r}{\partial t} + \frac{y_{1;i+1}\overline{\phi}_{i+1,k}^r - y_{1;i}\overline{\phi}_{i,k}^r}{\Delta r} + \overline{y}_{1;i+\frac{1}{2}}^r \left(\overline{\omega}_{i+\frac{1}{2},k+\frac{1}{2}}^r - \overline{\omega}_{i+\frac{1}{2},k-\frac{1}{2}}^r \right) = 0 \quad (6.16)$$

We then spatially discretize the u momentum equation and expand $\partial u_k h_k / \partial t$ to $h_k \partial u_k / \partial t + u_k \partial h_k / \partial t$. The latter term falls out by subtracting Eq. 6.16 multiplied by u_k from Eq. 6.13:

$$\overline{y}_{1;i+\frac{1}{2}}^r \overline{h}_{i+\frac{1}{2},k}^r \frac{\partial u_{i+\frac{1}{2},k}}{\partial t} + \frac{\overline{\phi}_{i+1,k}^r \overline{y}_{1;i+1}^r \left(\hat{u}_{i+1,k} - u_{i+\frac{1}{2},k} \right) - \overline{\phi}_{i+1,k}^r \overline{y}_{1;i+1}^r \left(\hat{u}_{i+1,k} - u_{i+\frac{1}{2},k} \right)}{\Delta r} +$$

$$\overrightarrow{y}_{1;i+\frac{1}{2}} \hat{u}_{i+\frac{1}{2},k+\frac{1}{2}} \overline{\omega}_{i+\frac{1}{2},k+\frac{1}{2}}^r - \overrightarrow{y}_{1;i+\frac{1}{2}} \hat{u}_{i+\frac{1}{2},k-\frac{1}{2}} \overline{\omega}_{i+\frac{1}{2},k-\frac{1}{2}}^r - \boxed{\alpha \phi_{i+\frac{1}{2},k} u_{i+\frac{1}{2},k}} +$$

$$g \overline{h}_{i+\frac{1}{2},k}^r \overline{y}_{1;i+\frac{1}{2}}^r \frac{\zeta_{i+1} - \zeta_i}{\Delta r} + \frac{q_{i+1,k} h_{i+1,k} y_{1;i+1} - q_{i,k} h_{i,k} y_{1;i}}{\Delta r} -$$

$$\overline{y}_{1;i+\frac{1}{2}}^r \overline{q}_{i+\frac{1}{2},k+\frac{1}{2}}^{rz} \frac{z_{i+1,k+\frac{1}{2}} - z_{i,k+\frac{1}{2}}}{\Delta r} + \overline{y}_{1;i+\frac{1}{2}}^r \overline{q}_{i+\frac{1}{2},k-\frac{1}{2}}^{rz} \frac{z_{i+1,k-\frac{1}{2}} - z_{i,k-\frac{1}{2}}}{\Delta r} -$$

$$\boxed{\alpha \overline{h}_{i+\frac{1}{2},k}^r \overline{q}_{i+\frac{1}{2},k}^r} + \overline{y}_{1;i+\frac{1}{2}}^r \frac{g}{\overline{\rho}_{i+\frac{1}{2},k}^r} \frac{\rho_{i+1,k} - \rho_{i,k}}{\Delta r} \frac{\left(\overline{h}_{i+\frac{1}{2},k}^r \right)^2}{2} +$$

$$\frac{g \overline{h}_{i+\frac{1}{2},k}^r \overline{y}_{1;i+\frac{1}{2}}^r}{\overline{\rho}_{i+\frac{1}{2},k}^r} \sum_{j=1}^{k-1} \left(\overline{h}_{i+\frac{1}{2},j}^r \frac{\rho_{i+1,j} - \rho_{i,j}}{\Delta r} + \left(\overline{\rho}_{i+\frac{1}{2},j}^r - \overline{\rho}_{i+\frac{1}{2},k}^r \right) \frac{h_{i+1,j} - h_{i,j}}{\Delta r} \right) -$$

$$\frac{\nu_h}{\Delta r} \left(h_{i+1,k} y_{1;i+1} \frac{u_{i+\frac{3}{2},k} - u_{i+\frac{1}{2},k}}{\Delta r} - h_{i,k} y_{1;i} \frac{u_{i+\frac{1}{2},k} - u_{i-\frac{1}{2},k}}{\Delta r} \right) + \boxed{\alpha \overline{h}_{i+\frac{1}{2},k}^r u_{i+\frac{1}{2},k} \frac{\nu_h}{r_{i+\frac{1}{2}}}} -$$

$$\overline{y}_{1;i+\frac{1}{2}}^r \left(\nu_{v;i+\frac{1}{2},k+\frac{1}{2}} \frac{u_{i+\frac{1}{2},k+1} - u_{i+\frac{1}{2},k}}{\overline{h}_{i+\frac{1}{2},k+\frac{1}{2}}^{rz}} - \nu_{v;i+\frac{1}{2},k-\frac{1}{2}} \frac{u_{i+\frac{1}{2},k} - u_{i+\frac{1}{2},k-1}}{\overline{h}_{i+\frac{1}{2},k-\frac{1}{2}}^{rz}} \right) = 0$$

$$(6.17)$$

Again, the alpha terms are marked with boxes. Another addition compared to the Cartesian 2-DV solution are the y-factors throughout the equation, which serve as width compensation factors. For w momentum, a similar procedure is applied.

The governing equations are spatially discretized with a central differences approach, except for the advective terms. The advective terms are discretized with higher-order flux limiters (Fringer et al., 2005), namely MINMOD flux limiters in the case of the momentum equations, and MUSCL flux limiters in the case of the transport equation.

The horizontal time integration of the momentum and transport equations is Euler explicit. The horizontal advective terms in the momentum equations are solved with the predictor-corrector scheme of MacCormack (Hirsch, 1988). The vertical time integration is semi-implicit, applying the θ-scheme. The global continuity equation (Eq. 6.6) and barotropic forcing are solved semi-implicitly (Casulli and Cheng,

1992). The case studies (Section 6.2.4) apply an implicitness factor $\theta = 1$ (i.e., the Euler implicit scheme) for the vertical momentum and transport equations, the global continuity equation, and the barotropic forcing. The non-hydrostatic pressure is standard solved with the Euler implicit scheme. The complete discretizations are shown in Appendix B.

The numerical framework largely follows the SWASH solution procedure (Zijlema et al., 2011). The code was expanded by adding the alpha terms and factors accounting for the varying cell width in tangential direction. The density and transport calculation modules were replaced by new modules based on the selected density equation (Wright, 1997), and the presented diffusivity equations.

6.2.4 Verification and validation

This chapter validates the model qualitatively and quantitatively. The qualitative validation is based on the expected stability of a dual layered double-diffusive system. The stability of a double-diffusive system is assessed based on its Turner angle Tu (Eq. 1.3; Ruddick, 1983).

The volumetric thermal expansion coefficient α_V ($°C^{-1}$) and salinity expansion coefficient β_V ($10^3 \, kg \, kg^{-1}$) are dependent on temperature and salinity itself, and are calculated for the average salinity and temperature on the interface. The expansion coefficients are derived from a linear regression to the density derivatives to temperature and salinity, where the density is calculated according to Wright (1997):

$$\alpha_V(T,S) = -2.285097 \cdot 10^{-5} + 1.324876 \cdot 10^{-5} \cdot T - 9.288537 \cdot 10^{-8} \cdot T^2 + 1.563353 \cdot 10^{-6} \cdot S$$

$$\text{(6.18)}$$

$$\beta_V(T,S) = 7.998742 \cdot 10^{-4} - 2.774404 \cdot 10^{-6} \cdot T + 3.188185 \cdot 10^{-8} \cdot T^2 - 4.151510 \cdot 10^{-7} \cdot S$$

$$\text{(6.19)}$$

The Turner angles are calculated for several case studies by taking the average of the expansion coefficients for the layers above and below the interface (Table 6.1). Cases 1 and 2 concern a system with two layers of equal depth, where a warm and salt water layer is overlying a cold and fresh water layer. Based on the Turner angle, salt-fingers are expected to occur. These salt-fingers are induced by applying a few very small perturbations of order 10^{-6} °C throughout the temperature field. Case 1 has a larger density ratio $R_\rho = -N_T^2/N_S^2$ than Case 2, yielding a lower salt flux over the interface (Kunze, 2003). In Case 3 and 4, a dual-layered system is built up by a central inflow through the bottom with an outer radius of 0.25 m. The inflow velocity w_{in} is built up linearly over the first 10 min to prevent a sudden pressure wave at $t = 0$. The average water level is kept constant by an uniform outflow with the same discharge over the right, outer boundary. Based on the Turner angle, a system with double-diffusive convection is expected to build up in Case 3, whereas a gravitationally unstable system is expected to develop in Case 4.

The quantitative validation is based on an analytical solution for the radial expansion of a layer of dense water around a central inflow under laminar flow conditions

Table 6.1: The dimensions, properties, and consequent stability parameters applied in the case studies. *Up* and *Down* refer to the upper and lower layer of the dual layered system (in Case 3 to 5, the lower temperatures and salinities are properties of the central inflow).

Case	Dimension (m)		T (°C)		S (weight-‰)		w_{in} (m s^{-1})	Tu (°)	R_ρ (-)
	Depth	Radial	Up	Down	Up	Down			
1	0.7	3.0	20	10	1	0	-	71.2	2.04
2	0.7	3.0	20	15	1	0	-	85.0	1.19
3	0.5	1.5	20	25	1	3	$1 \cdot 10^{-3}$	-85.5	0.77
4	0.5	1.5	20	26	1	2.5	$1 \cdot 10^{-3}$	-96.4	1.25
5	0.4	3.0	30	5	0	10	$5 \cdot 10^{-4}$	-13.2	-0.62

(Case 5; Table 6.1). The interface expansion is described by its increasing interface radius r_{int} over time. When the inflow is colder and more saline than the overlying water body, the developing layer has different growth rates for the salinity and temperature interface (Fig. 6.4). This is a consequence of the molecular heat diffusion, which is approximately 100 times larger than the diffusion of salt. In laminar flow conditions, molecular diffusion is the main driver of heat and salt exchange in stable layered systems.

In this quantitative case study, the central inflow has an outer radius of 0.2 m. To allow a slow development of the bottom layer, the inflow is placed slightly deeper compared to the rest of the bottom, and the inflow velocity linearly increases over the first 20 min. Like Case 3 and 4, the discharge over the right outflow boundary is set equal to the inflow discharge:

$$Q_{out} = Q_{in} = w_{in} \cdot A_{in} \tag{6.20}$$

To derive the growth rates of the temperature and salinity interfaces, we consider the similarity solution of the heat equation for a fixed boundary concentration (Bergman et al., 2011):

$$c(x,t) = c_{in} + \Delta c \cdot \text{erfc}\left(\frac{x}{\sqrt{4 \cdot D \cdot t}}\right) \tag{6.21}$$

where x is the distance from the interface. $\Delta c = c_0 - c_{in}$ is the difference in concentrations (salinity or temperature) between the upper water body, represented by its initial concentration, and the inflow. The total mass M that has crossed the interface is found by integration of Eq. 6.21 over $x = 0 \rightarrow \infty$, and multiplication the growing interface surface A_{int}:

$$M(t) = A_{int} \cdot \int_0^\infty (c - c_{in})\, dx = A_{int} \cdot \Delta c \cdot \int_0^\infty \text{erfc}\left(\frac{x}{\sqrt{4 \cdot D \cdot t}}\right) dx = A_{int} \cdot \Delta c \cdot \frac{\sqrt{4 \cdot D \cdot t}}{\pi} \tag{6.22}$$

Derivation over time results in the time dependent mass flux over the interface:
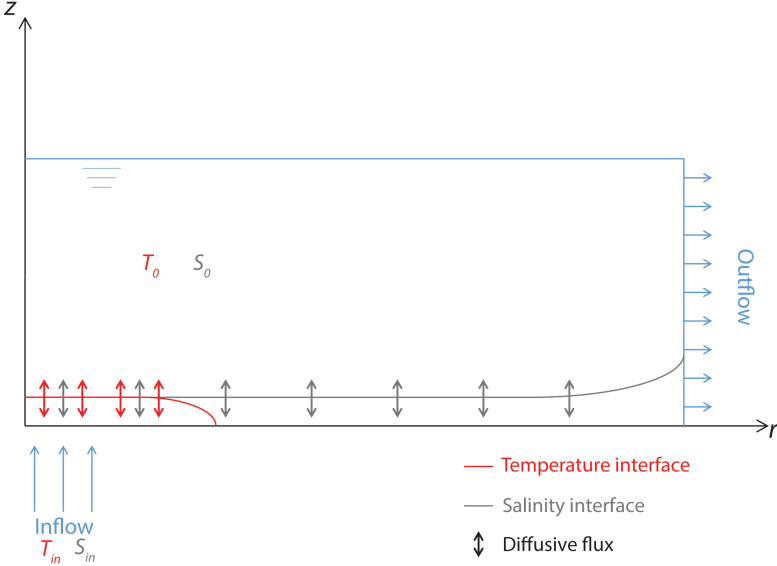
Figure 6.4: Conceptualization of the quantitative validation (Case 5), with locations of the salinity and temperature interfaces at a certain time after the start of a central inflow. The inflow is colder and more saline than the overlying water body.

$$\Phi_{int}(t) = \frac{dM}{dt} = \Delta c \cdot \sqrt{\frac{D \cdot t}{\pi}} \cdot \left(2 \cdot \frac{dA_{int}}{dt} + \frac{A_{int}}{t}\right) \tag{6.23}$$

With $A_{int} = \pi r_{int}^2$, and assuming that the interface surface increases linearly with time at a constant inflow, we can rewrite:

$$r_{int}(t) = \sqrt{\frac{\Phi_{int}}{3 \cdot \Delta c} \cdot \sqrt{\frac{t}{D \cdot \pi}}} \tag{6.24}$$

We assume that no mass is stored in the lower layer. Consequently, the mass flux that crosses the interface is equal to the net mass flux into the domain $\Phi_{in} - \Phi_{out} \approx w_{in} \cdot A_{in} \cdot (c_{in} - c_0)$:

$$r_{int}(t) = \sqrt{\frac{w_{in} \cdot A_{in}}{3} \cdot \sqrt{\frac{t}{D \cdot \pi}}} \tag{6.25}$$

This equation can be used to validate the interface growth of both the salinity and temperature interface in the case of laminar flow.
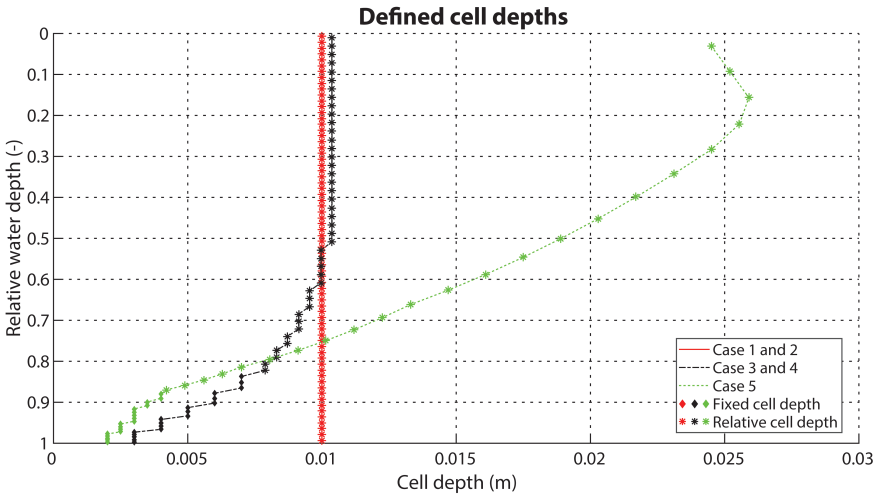
Figure 6.5: Defined cell depths for the Cases 1 to 5. For plotting reasons, the vertical axis displays the depth from the water surface relative to the local water depth. The cell depths that are defined relative to the local water depth (as marked by *) are displayed for the average water depth in each case study.

In all the case studies, we applied a time step of 2 ms and a horizontal mesh size of 5 mm in radial direction. The vertical mesh size in Case 1 and 2 was set uniformly to 10 mm. In the Cases 3 until 5, the vertical mesh size varied over depth. Because the processes of most interest occurred near the bottom, the mesh size was decreasing towards the bottom (Fig. 6.5).

6.3 Results and discussion

The performance of the numerical framework was tested in several case studies subject to double-diffusive processes. The numerical results of these case studies and the extended SWASH code are presented in Hilgersom et al. (2016e).

6.3.1 Case 1 and 2: Salt-fingers

The temperature and salinity gradients in the Cases 1 and 2 yield a theoretical onset of salt-fingers, with respective Turner angles of 71.2° and 85.0°. The numerical results confirm that salt-fingers are formed over the interface (Fig. 6.6). Based on the difference in density ratios, the salt-fingers in Case 2 are hypothesized to transport more salt and heat. Fig. 6.7 shows an interface rise of about 0.02 m in Case 1 and 0.09 m in Case 2 over a numerical model run of 1.5 h. Given the system of closed boundaries, we therefore find a significantly larger transport over the interface in Case 2.

The effective transport of heat and salt over an interface while maintaining a sharp interface is a clear property of double-diffusive salt-fingers (Turner, 1965). Care should be taken that these salt-fingers are calculated in a 2-D radial grid. Yoshida and Nagashima (2003) pointed out that there is still a lack of knowledge
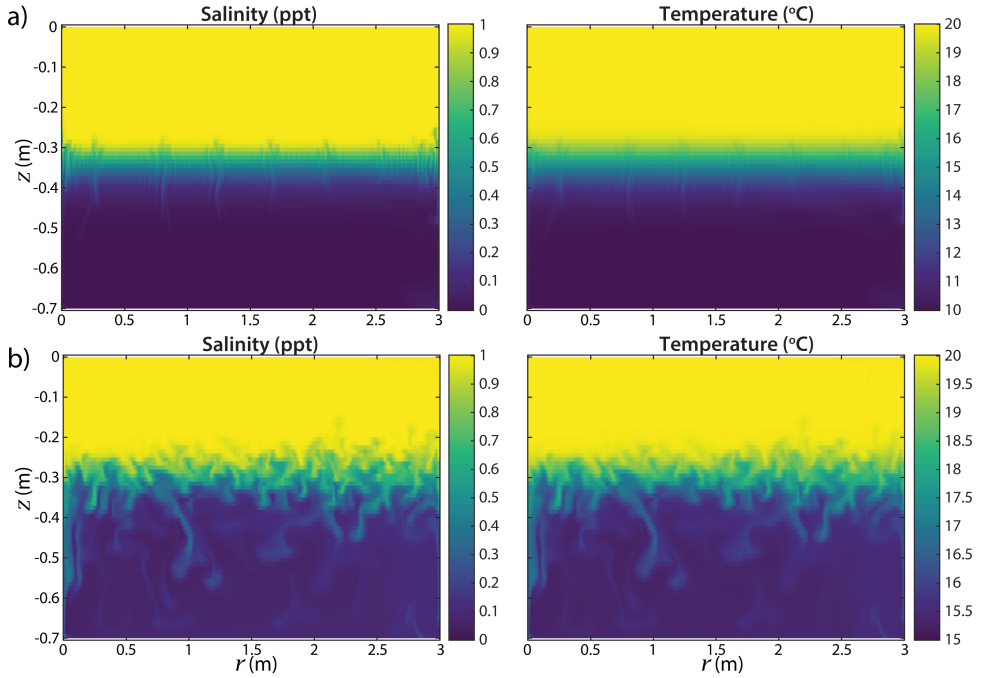
Figure 6.6: Salt-fingering in a layered system with a warm and saline water on top of a cold and fresh layer ($t = 4500$ s since the start), with density ratios of a) $R_\rho = 2.04$ (Case 1), and b) $R_\rho = 1.19$ (Case 2).

about the 2-D and 3-D structures of salt-fingers and its implications for the interpretation of 2-D numerical results.

6.3.2 Case 3: Double-diffusive convection

The temperature and salinity gradients in Case 3 yield the onset of double-diffusive convection. Like Case 1 and 2, a sharp interface develops over which salt and heat is transported by diffusion. Fig. 6.8 confirms the development of a salt-heat interface and a convective layer above the boil. Other convective cells further transport the salt and heat above the interface. Fig. 6.8 shows that already a considerable amount of heat and salt was conveyed to the upper layer over the first 1.5 h. The lower convective layer slowly builds up, and local eddies clearly counteract the development when the lower convective layer is still thin.

6.3.3 Case 4: Gravitationally unstable system

Compared to Case 3, a slightly altered inflow temperature and salinity in Case 4 theoretically makes the developing layer gravitationally unstable (Table 6.1). In other words, the water body itself is denser than the inflowing water, which consequently flows upwards. The numerical results confirm the onset of a central buoyant flow above the inflow (Fig. 6.9).

Interestingly, plumes develop from the upward flow. Downward plumes are
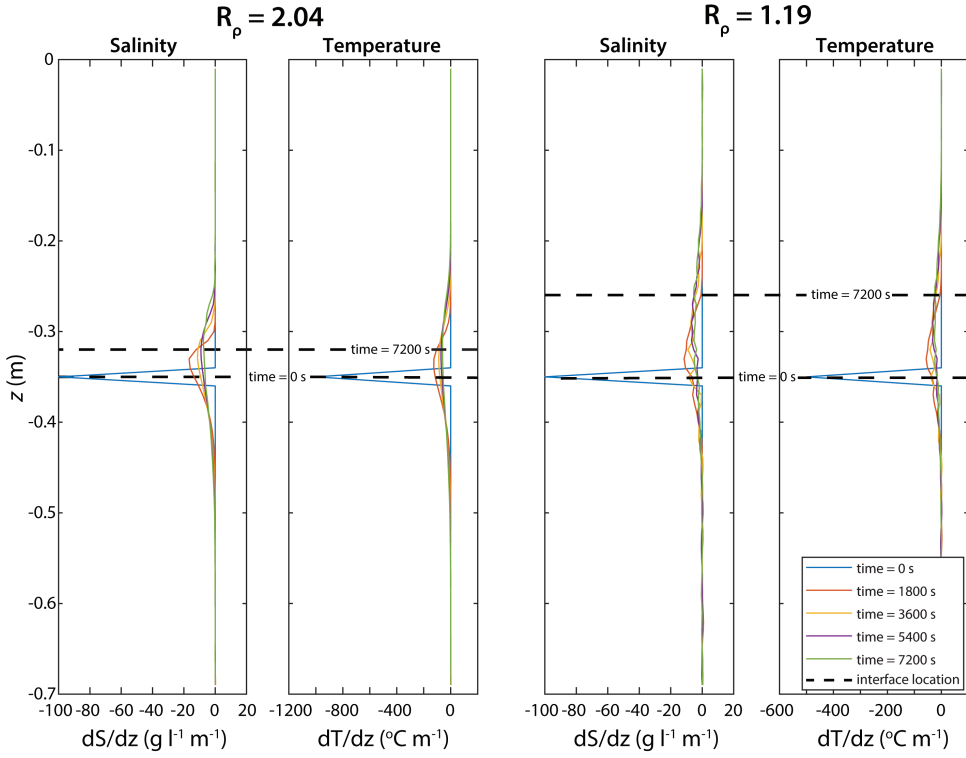
Figure 6.7: Interface positioning over time, displayed by the derivatives $\partial S/\partial z$ and $\partial T/\partial z$ of the salinity and temperature profiles, for the density ratios $R_\rho = 2.04$ (Case 1) and $R_\rho = 1.19$ (Case 2).
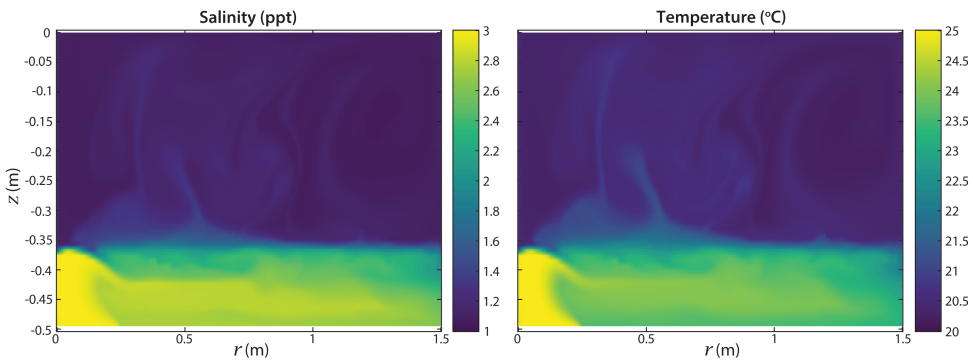

Figure 6.8: Double-diffusive layering (Case 3) with cold and fresh water on top of a warm and saline inflow ($t = 5400\,\text{s}$ since the start).
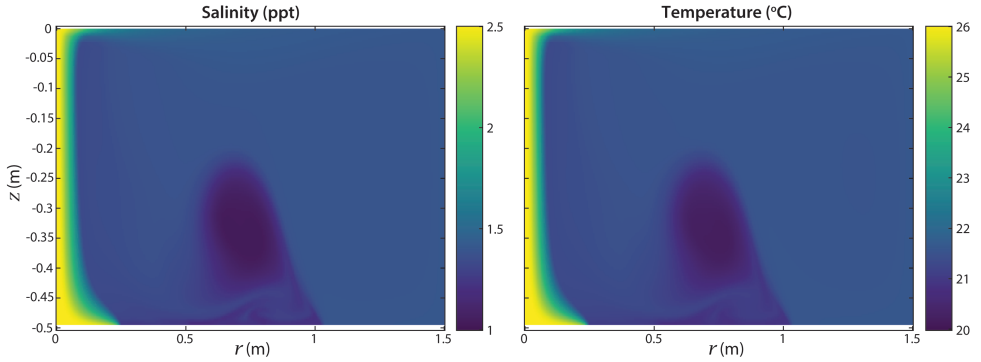
Figure 6.9: Unstable system (Case 4) with denser cold and fresh water on top of a warm and saline inflow (t = 5400 s since the start). The inflowing water flows upward through the centre, independent of the inflow velocity.

also visible below the floating warm and saline water. Like the salt-fingers in Case 1 and 2, where warm and saline water also overlaid cold and fresh water, this is a mechanism to dissipate the heat and salt gradients.

6.3.4 Case 5: Radial expansion of a dense water layer

The analytical solution for the radial expansion of inflowing cold and saline water (Eq. 6.25) holds for a situation with laminar flow. Given the geometric properties of the conceptualized situation and the initially very thin layer of dense water, it is difficult to define the inflow properties so that the flow near the inflow is immediately laminar. For the selected inflow parameters (Table 6.1), laminarisation of the flow appears to occur after approximately 1700 s (Fig. 6.10). From that moment, the numerical results show significant differences between the salinity and temperature interface growth. The analytical results are therefore shifted in time to match the interface radii with the numerical results at the moment that the flow becomes laminar.

Accounting for a purely molecular diffusion, the numerical results show a fair agreement with the analytical results. As we found some small occasional eddies occurring after t = 1700 s, we also plotted results analytical results assuming the diffusivity was on average for 0.2 % influenced by turbulent diffusion. Here, the turbulent diffusion was calculated from a kinematic viscosity $\nu = 10^{-6}\,\mathrm{m^2\,s^{-1}}$ by applying the Prandtl-Schmidt number. The assumption of a slight influence of turbulence diffusion shows a better agreement with the numerical results.

One critical note here is the sensitivity of the interface growth to the definition of the interface location. We defined the interface location at the position of 50 % of the step change between the inflow concentration (T_{in} and S_{in}) and the concentration of the water body (T_0 and S_0), because this matches our visual interpretation of the interface in the numerical results. However, selecting the interface at a larger percentage of the step change significantly increases the growth, and makes the numerical and analytical results incomparable.
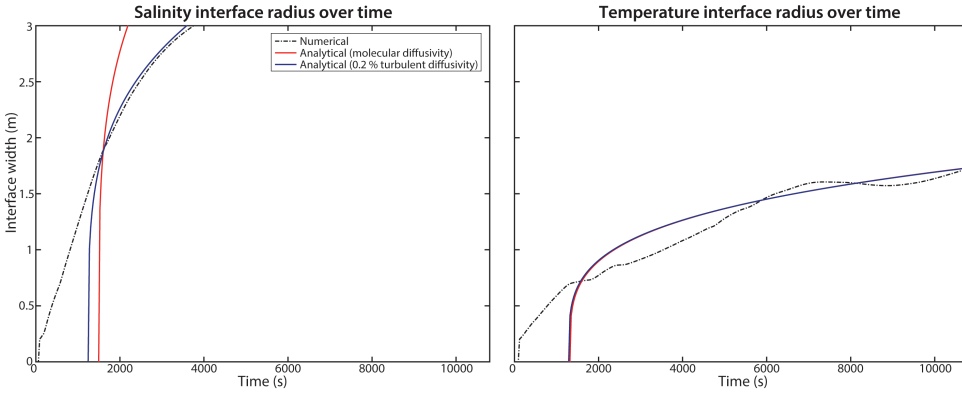
Figure 6.10: Evolution of the interface between a warm and fresh water body and a bottom cold and saline layer developing form a central inflow. After $t = 1700\,\text{s}$, the flow in the numerical results becomes laminar and differences between the temperature and salinity interface growth become visible. Analytical results are plotted for the assumptions of completely molecular diffusion (red), and for diffusivities that are for 0.2 % influenced by turbulent diffusion (blue).

6.4 Conclusions

This study shows the successful derivation of an axisymmetric framework for a hydrodynamic model incorporating salt and heat transport. This model set-up allows to efficiently calculate salt and heat transport whenever a situation is modelled that can be approximated by axisymmetry around a central location. The quasi 3-D grid description demands approximately the same execution time as a 2-DV description with the same dense mesh, and therefore avoids the need to solve the equations over a dense mesh in the third spatial dimension.

For our purpose of studying shallow water bodies, three aspects were important: 1) the inclusion of a free surface, 2) the efficient solution of a circular seepage inflow, which makes the problem three-dimensional, and 3) a proper simulation of density driven flow and double-diffusivity driven salt and heat transport. The former aspect was already fulfilled by employing the SWASH framework.

The second aspect was solved by assuming axisymmetry for the Navier-Stokes equation in cylindrical coordinates. The derived numerical framework is presented as a Cartesian 2-DV description with few additional terms and width compensation factors. Our implementation of these terms in the non-hydrostatic SWASH model demonstrates the opportunity to easily expand a 2-DV model towards the presented quasi 3-D model.

The third aspect was fulfilled by extending SWASH with a new density and diffusivity module. The case studies demonstrate explainable behaviour for density driven flow and double-diffusivity driven salt and heat transport. The formation of convective layers and salt-fingers are in accordance with the theory of double-diffusivity. A quantitative validation method was presented to evaluate the model's performance for a cold and saline inflow developing a dense water layer near the bottom. For laminar flow conditions, the numerical model showed a similar radial

expansion of the bottom layer as expected from analytical results.

Although the model is already able to show expected behaviour in the double-diffusive regime, we recommend a further exploration of its limitations and possibilities. For example, a grid convergence study should indicate whether the selected mesh size yields a convergence of results for all diffusion and advection dominated cases. Further, the effect of sharp density gradients on the accuracy of the standard k-ϵ model should be examined, and a comparison with DNS model results would support the validation of the model. In future applications, we stress that this model approach should be employed as a RANS model that simulates thermohaline stratification processes on a larger scale. As such, the model can be favourable in applications that allow an axisymmetric approach.

6

7

Modelling dense 3-D temperature data from a laboratory setup

The developed numerical framework for an axisymmetric non-hydrostatic transport model (Chapter 6) is applied to simulate the density-driven flow in a laboratory set-up, for which the data were presented in Chapter 4. The model demonstrates its capability to correctly represent larger-scale double-diffusive phenomena that were found in the laboratory set-up. However, due to unexpected flows within the measurement set-up, which could not be simulated within our model, the developing stratified layers in the measurements deviate from the model results. In general, it can be concluded that the expectations of models regarding the capturing of double-diffusive phenomena should always be limited to a correct representation of the developing system: the occurrence of occasional plumes can be predicted, but cannot be predicted on specific locations and times.

This chapter was not submitted for peer review.

7.1 Introduction

Within this thesis, we have presented a method to measure dense distributed temperature profiles and a non-hydrostatic modelling approach for density-driven flows. This chapter tests the model capability to simulate the measured temperature profiles in the laboratory set-up. In this set-up, the temperatures, salinities, and discharges of the seepage source are known, and deviating from the salinities and temperatures in the surface water.

Chapter 4 demonstrated that the 3D dense DTS set-up can measure very detailed temperature profiles. In double-diffusive systems, even the occurrence of plumes and potential salt-fingers were revealed (Hilgersom et al., 2016c).

The unstable nature of these small-scale double-diffusive phenomena prevent their numerical simulation in time and in place. Besides, the high computational demand of 3-D transport models due to the requirement of a fine mesh makes 3-D simulations on very small scales undesirable. In Chapter 6, we have seen a successful implementation of a quasi 3-D axisymmetric transport model. By calculating in two spatial dimensions, calculation times are reduced drastically. Although this grid set-up is definitely not capable of simulating the occurrence of double-diffusive phenomena at exact locations, we have demonstrated its general capability to simulate double-diffusion.

This chapter aims to validate the model with data from the laboratory set-up presented in Chapter 4 (Hilgersom et al., 2016b). To this end, the known characteristics (seepage discharge, salinity, and temperature) are simulated, and the resulting temperature profiles are compared with the measured high-resolution temperature profiles. Finally, this chapter aims to provide insight in the model's applicability for inversion of a seepage discharge from a measured 3-D temperature profile time series.

7.2 Method

7.2.1 Model input data

The measurements were performed with the set-up described in Section 4.2.3 and Fig. 7.1. During the measurements, some unexpected flows were observed along the edges of the covering anti-rooting membrane (Section 4.3.1). Besides, the CTD-diver, which was located in the small reservoir underneath the membrane, indicated an increase of the water pressure each laboratory run (Fig. 7.2). This confirms that the water did not flow freely through the anti-rooting membrane, but was pushed sideways underneath the wooden strips that fixated the membrane around the boil.

The discharge from the preparation reservoir to the small reservoir underneath the anti-rooting membrane was measured by measuring the weight decrease of the preparation reservoir with a scale (Fig. 7.1). Since the membrane was found to impede the outflow from the small reservoir, and the excess inflowing water was stored by increasing the water pressure, we assessed the outflow over the membrane by a linear reservoir approach:
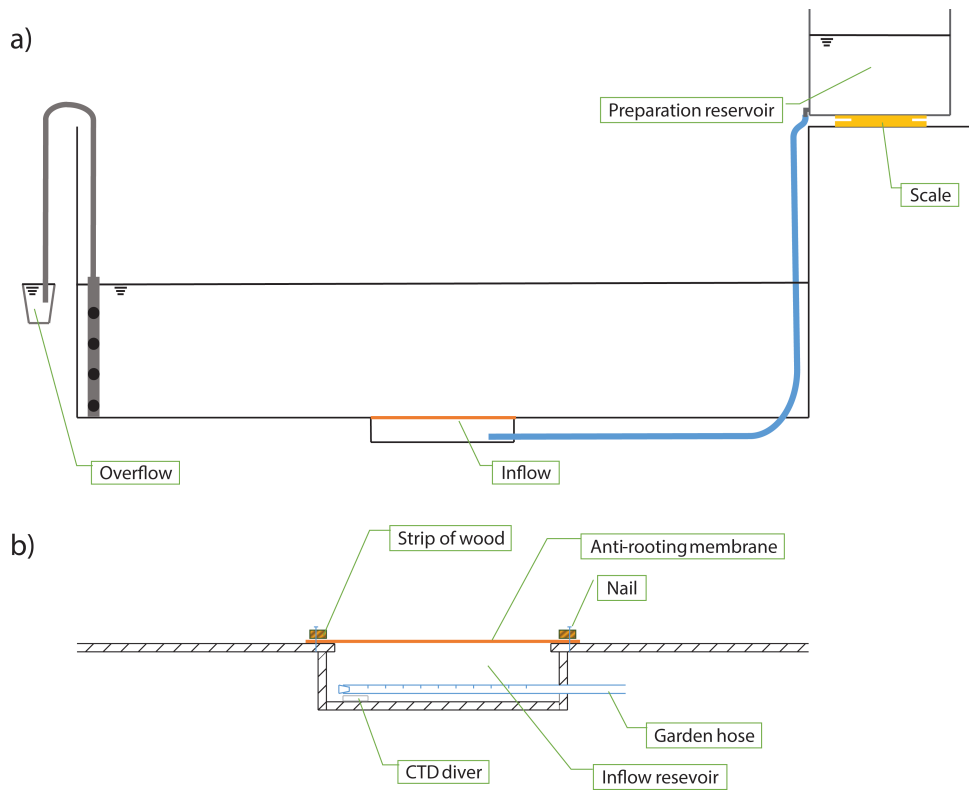
Figure 7.1: **a)** Schematization of the measurement set-up. **b)** Detail of the inflow.
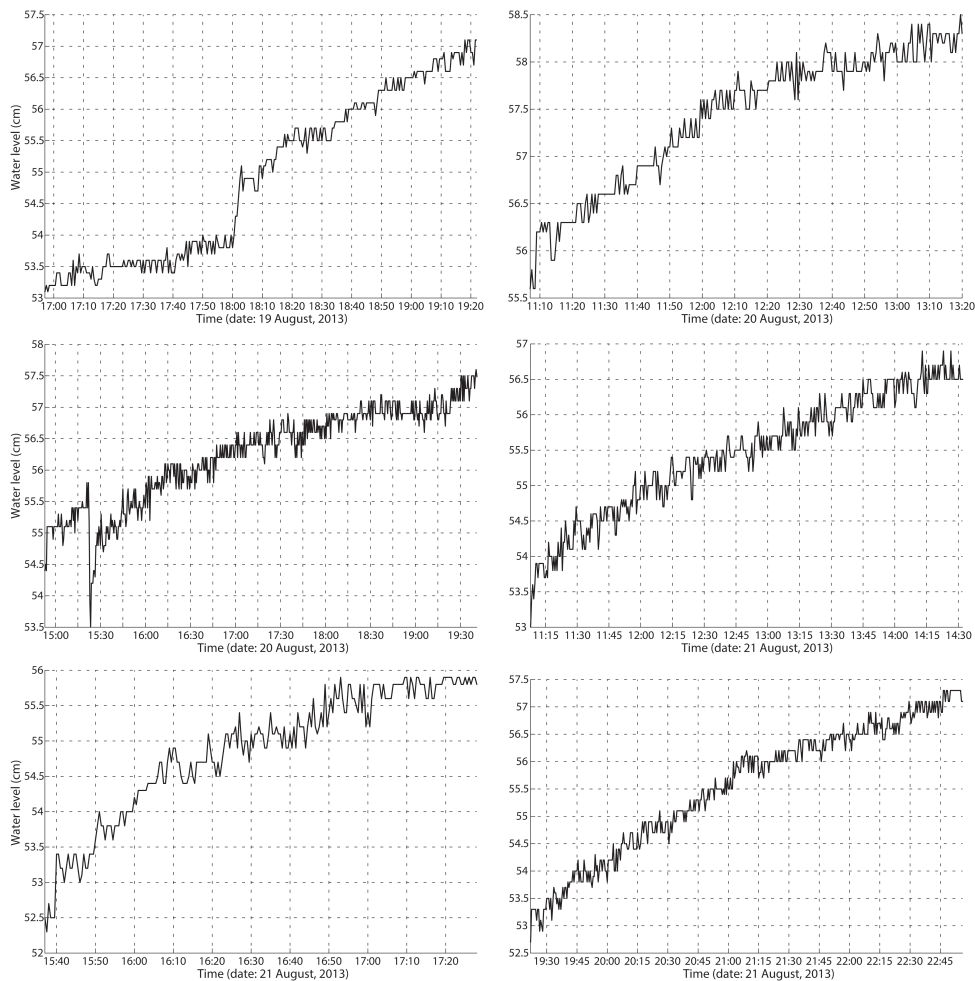
Figure 7.2: Water pressure (in cm water column) over time for Runs 1 to 6, as a measure for the linear reservoir storage underneath the anti-rooting membrane.

$$Q_{out}^{n} = Q_{out}^{n-1} \cdot \exp\{-k_{lin} \cdot \Delta t\} + Q_{in}^{n-1/2} \cdot [1 - \exp\{-k_{lin} \cdot \Delta t\}] \qquad (7.1)$$

where Q_{in} and Q_{out} are the inflow from the preparation reservoir and the outflow through the membrane divided by the horizontal surface of the small reservoir underneath the membrane ($\mathrm{m\,s^{-1}}$). Δt is the time difference between the current and the previous time step, which are indicated by the superscripts n and $n-1$, respectively. The linear reservoir coefficient k_{lin} ($\mathrm{d^{-1}}$) can be seen as the reciprocal of the outflow resistance, which is imposed by the membrane or the flow paths underneath the wooden strips that fixate the membrane. k_{lin} is selected constant and equal for each run, and is calibrated manually based on the measured inflow of heat for each of the six runs.

The inflow temperature and salinity were measured with the CTD-diver in the inflow reservoir. Since the measured temperature and salinity are measured at the bottom of the inflow reservoir near the location where the inflow reservoir is recharged from the preparation reservoir, these measurements do not represent the water temperature and salinity crossing the membrane. Therefore, the model input temperatures and salinities are calculated from the output of a well-mixed mass balance model for the inflow reservoir:

$$C_{out}^{n} = \frac{C_{out}^{n-1} \cdot V_{res}^{n-1} + C_{in}^{n-1/2} \cdot Q_{in}^{n-1/2} \cdot \Delta t - C_{in}^{n-1/2} \cdot Q_{out}^{n-1/2} \cdot \Delta t}{V_{res}^{n}} \qquad (7.2)$$

where V_{res} is the uncompressed equivalent of the water volume in the reservoir. The inflow concentration C_{in} represents the measured temperature or salinity at the entrance of the inflow reservoir, entering with the measured discharge Q_{in}. The reservoir concentration C_{out} is assumed well-mixed and representative for the concentration of the water flowing through the membrane with discharge Q_{out} calculated from the linear reservoir model.

The initial conditions for the non-hydrostatic model are set uniform with zero velocity. The initial temperature is set to the spatial average of the temperatures measured with the 3-D dense DTS set-up at the start of the measurements. The initial salinity is calculated from electrical conductivity (EC) measurements with a hand-held EC meter, by applying the equation presented by Schemel (2001).

Chapter 4 analysed two laboratory case studies (Runs 2 and 6, Table 4.1). In this chapter, we simulate and analyse the results of all six laboratory case studies presented in Table 4.1.

7.2.2 Model set-up

The model simulations of the laboratory measurements are similar to the case studies presented in Chapter 6. However, in this case a fine bottom profile is defined including a sharp threshold on the location of the square PVC ring in the DTS set-up, which obstructs horizontal flows along the bottom. As the model set-up is axisymmetric, an additional assumption is required: the location in radial distance is defined as the average of the distances from each point on the square PVC ring to the centre.
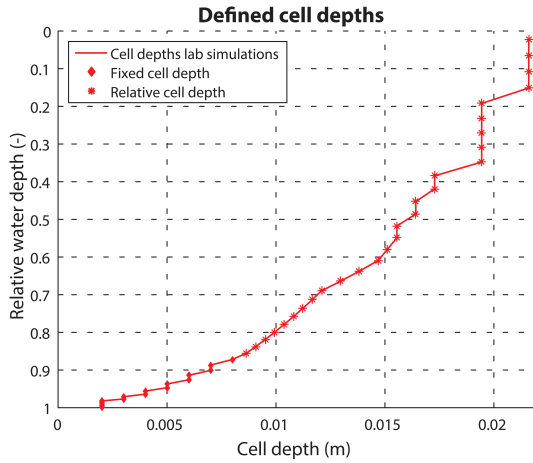
Figure 7.3: Cell depths applied during all model runs.

The horizontal dimension of the model domain is defined by an equal recalculation from the horizontal dimensions of the square 2.5 m by 2.5 m container to the average radius from the centre: $r = 1.403$ m. The water level is initially uniform on 0.5 m, and its average value remains constant over each model run, since the outflow is set equal to the inflow discharge.

The selected numerical time step is 2 ms. The radial mesh size is uniform and approximately 6 mm. As explained in Chapter 6, SWASH applies depth-following sigma layers. This means that at least part of the cell depths are defined relative to the water level. As the most interesting processes occur near the bottom, we have chosen for small and fixed cell depths near the bottom. Toward the surface, the cell depths increase and from the seventeenth cell the cell depths are defined relative to the water depth (Fig. 7.3).

7.3 Results and discussion

The linear reservoir coefficient was calibrated manually by determining the best model performance for the total heat storage over time. For $k_{lin} = 70 \, \text{d}^{-1}$, the modelled total heat storage in the area of the measurement set-up appears in fair agreement with the measured heat storage (Fig. 7.4). Although this linear reservoir coefficient does not result in heat inflows that are accurately matching the measured heat increments in all cases, the results can be considered acceptable, and the selection of one equal coefficient for all cases is considered more important from a physical point of view.

In this section, we compare the measured and modelled temperature profiles near the end of each laboratory run (Fig. 7.5). For this comparison, the measured temperature data is converted to cylindrical coordinates and averaged in tangential direction around the centre of the inflow. The modelled temperature data sets are clipped to the space which is covered by the 3-D dense DTS set-up. Linear
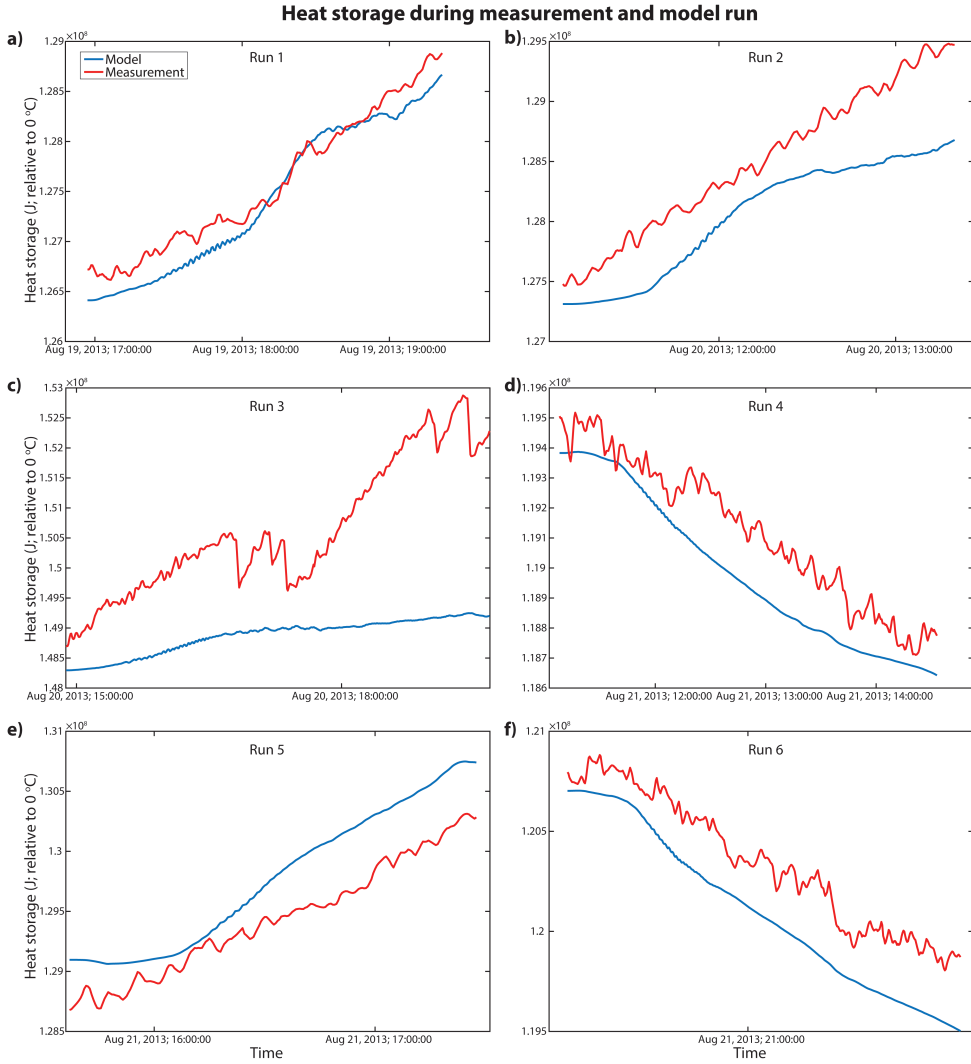
Figure 7.4: Measured and modelled heat storage in the water volume covered by the measurement set-up. The model applies a linear reservoir coefficient $k_{lin} = 70\,\mathrm{d}^{-1}$ to the measured discharge from the preparation reservoir.
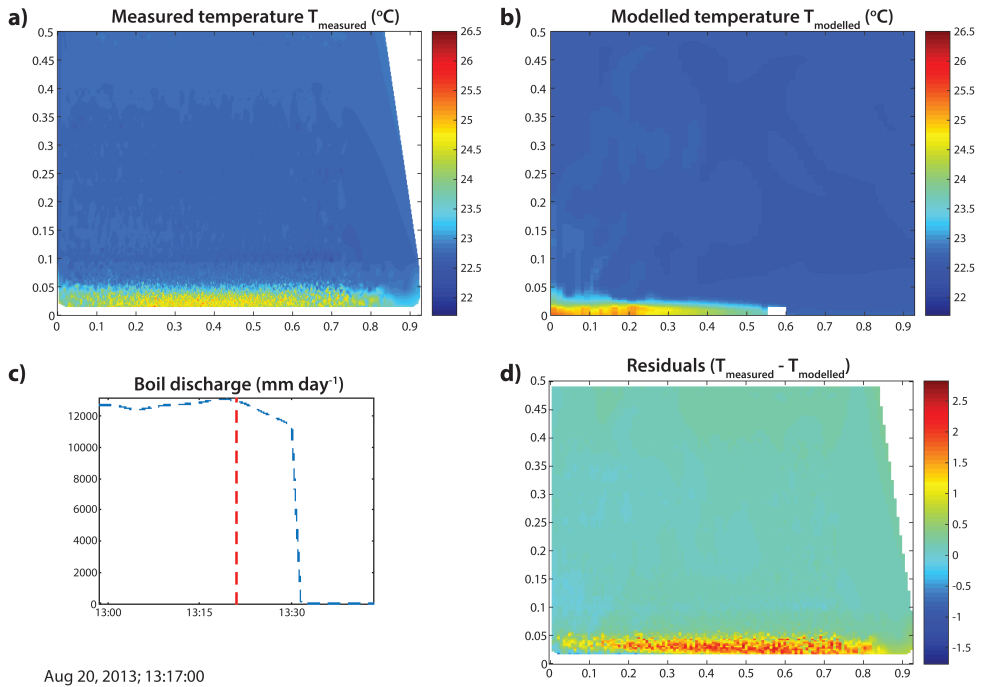
Figure 7.5: Measurement (**a**) and model (**b**) results near the end of the seepage inflow (**c**) in Run 2. The measurements and model results are compared in this chapter by means of their residuals (**d**).

7

interpolation of both data sets to an equidistant depth vector allowed determining the residuals of the measured and modelled temperatures in order to compare them.

The measurement runs with a cold seepage inflow only display temperature disturbances near the bottom. In the model, the inflowing cold, dense water also remained in the bottom part of the domain, leading to residuals of almost zero at levels higher than 0.1 m above the bottom (Fig. 7.6). The results for Run 4 display slightly positive residuals in the top right part of Fig. 7.6a. These deviations are presumably caused by the interpolation of the few data points in this part of the measurement set-up.

Near the bottom, the measurements showed unexpected results with cold seepage water entering around the edges of the boil instead of the centre (Chapter 4). On the contrary, the model results resemble the expected dense layer growth above the seepage inflow, leaving clear residual patterns in the bottom 0.1 m (Fig. 7.6). Above the boil, the modelled water temperature was lower than the measured temperature, resulting in positive temperature residuals. In the measurement set-up, the cold water seeped in around the boil, which locally resulted in negative residuals.

Despite the known defects in the laboratory set-up, these are hard to resemble in our model, since it is unknown how the boil seepage enters the system exactly. For
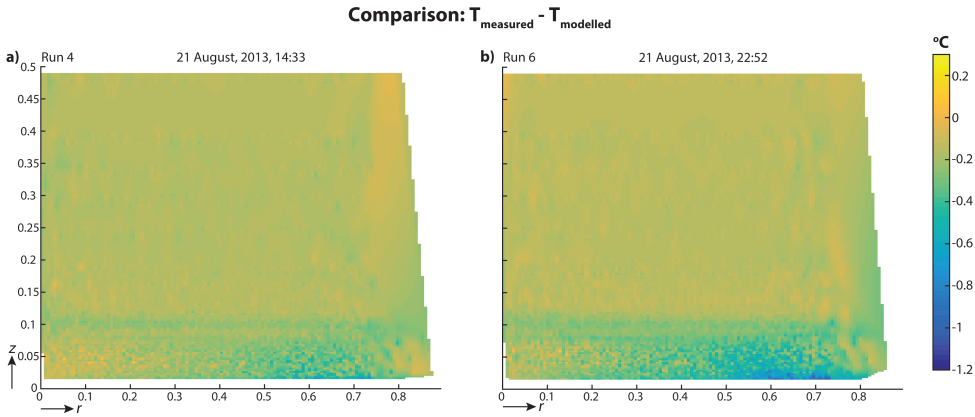
Figure 7.6: Comparison of the residuals for the colder seepage inflows (a few minutes before the end of Runs 4 and 6).

example, the water could flow in horizontally through the openings in the bulging membrane, or even underneath the wooden strips which keep the membrane in place. Besides, the pressure differences may induce locally high velocities through the membrane, which impose an additional challenge to the numerical model. Further, the seepage water did not appear uniformly around the boil, indicating local preferential flows. Model attempts (unpublished) with an inflow at the edges of the boil did not yield better results.

Like Run 4, Run 3 shows some sudden temperature deviations in the top right of the residuals figure (Fig. 7.7c). Again, these could be caused by the interpolation of the few data points in this part of the set-up. Near the central axis, a consistent deviation is visible toward the top, which is caused by a central upward flow of heat in the model. The upward flow is a consequence of the density gradient which is theoretically unstable during part of the run ($R_\rho > 1$; Fig. 7.8). Although the calculated Turner angles in Table 4.1 suggest that Run 2 has a larger risk to become gravitationally unstable than Run 3 ($Tu = -89.3°$ vs. $Tu = -85.8°$), the values in this table were rough calculations for time-averaged inflow temperatures and salinities of the water that entered from the preparation reservoir.

In the lower 0.1 m, clear differences up to 3 °C are visible between the model and measurement results for all the cases with a warmer seepage inflow. Directly above the boil, the measured temperatures are lower than the modelled temperatures, whereas from a few cm above the boil and around the boil, the measured temperatures are higher. Like the cold seepage cases, the higher temperatures around the boil are a consequence of the sideways seepage that is not included in the model.

The lower measured temperatures directly above the boil and the higher temperatures right above this layer are the consequence of a slightly delayed growth of the warm saline layer in the model. This layer appears to diffuse less heat and consequently remain more concentrated in the model. In the measurements, more

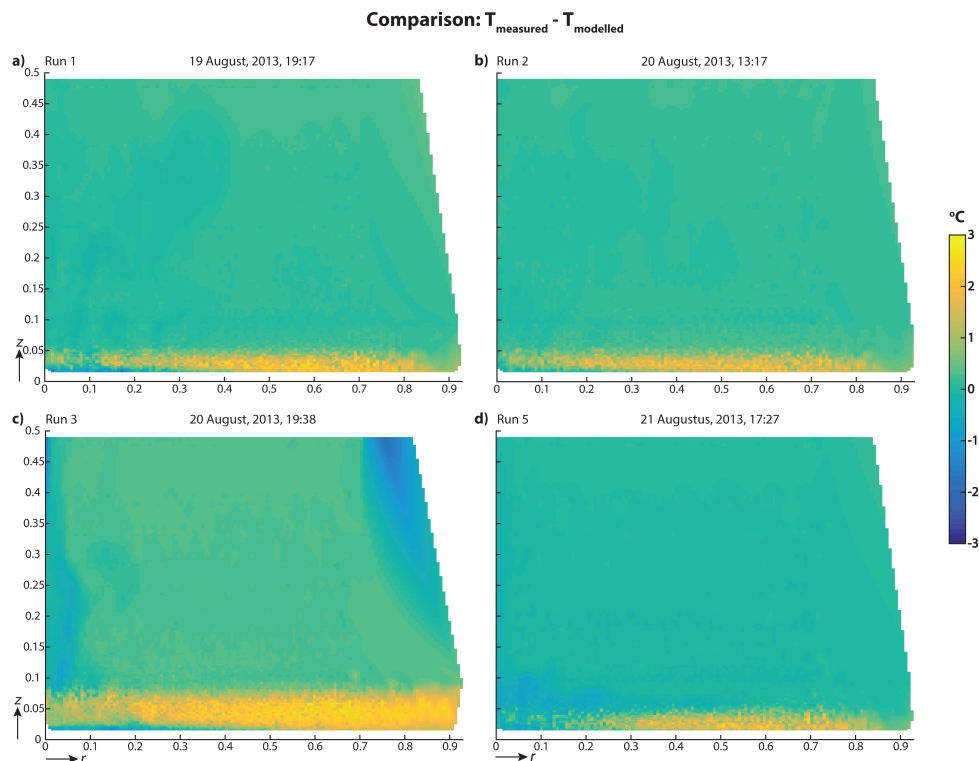**Comparison: T$_{measured}$ - T$_{modelled}$**

Figure 7.7: Comparison of the residuals for the warmer seepage inflows (a few minutes before the end of Runs 1, 2, 3, and 5).
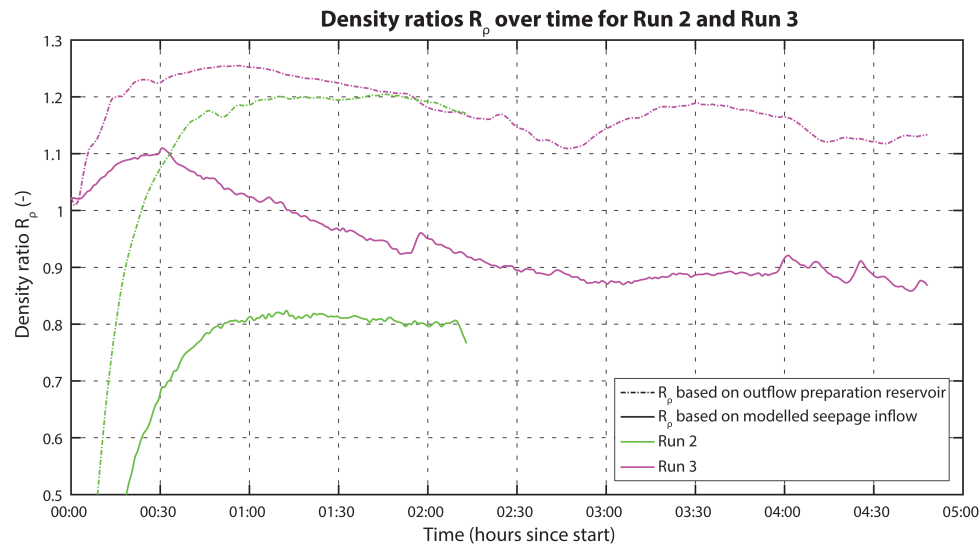

Figure 7.8: Estimated density ratios over time for Runs 2 and 3.

heat diffusion is apparent over the interface, explaining the higher temperatures above the interface. Possibly, the model accounts insufficiently for the effects of double-diffusive convection, which tends to transport more heat over the interface. Alternatively, the way in which the water seeps through the membrane might increase the diffusion near the boil. Here, one could think of direct heat conduction through the membrane or additional mixing caused by higher velocities of the water that seeps through or past the membrane. Our data is insufficient to provide any conclusive statements about the nature of the larger heat diffusion.

Lastly, we need to take into account that the inflow discharges, temperatures, and salinities are modelled from measurements instead of direct measurements. This modelling step introduces an additional source of inaccuracy for the model input. On the other hand, our observations have proven the necessity of such a modelling step for the considered laboratory set-up, as applying the measured input parameters unmodified yields a growth of the modelled saline layer that is too soon and too quick.

7.4 Conclusion

Due to unexpected flows in the studied laboratory set-up, a conclusive model validation from the measurement data is not possible. The intended boil seepage flow was largely affected by the laboratory set-up itself, which inhibited the direct application of the measured variables serving as a model input, and made the exact location and direction of the seepage inflow unknown. The model input variables were estimated from a linear reservoir model, which introduced additional model uncertainty.

Because no information was found on how the water seeped through the boil in the laboratory set-up, the model applied the originally intended vertical seepage flow through the boil opening. This directly affected the model results, as the model predicted the seepage inflow centrally above the boil where the measurements displayed the growth of a seepage layer around the boil. Further, the diffusion of heat from the warm saline boil seepage appeared to be larger in the measurements than in the model. Again, the design of the laboratory set-up could be responsible for the higher diffusion rates, as additional eddies may occur near the locations where the water seeped sideways with high flow velocities.

Although the 3-D dense DTS set-up generally provided very accurate data, the interpolation of the relatively few data points near the top rims of the cube appeared to occasionally provide inaccuracies up to several degrees Celsius. Therefore, care should be taken applying the temperature data from this part of the set-up.

In conclusion, the model was able to grow stable and double-diffusive convective layers as expected from the lower or higher temperature of the saline seepage. The extent to which the model is capable of reproducing double-diffusive convection remains unclear, as the diffusion of heat over the interface is both larger in the measurements with colder and warmer seepage.

Accordingly, the application of the measurement set-up and the model for an inversion of the seepage flux cannot be tested based on this data. However, the inversion of boil seepage from thermohaline surface water systems in general will

7

be challenging. Firstly, the irregular occurrence of plumes and convection cells can currently not be reproduced on larger than molecular scale by any model. Such deviations directly affect the inverted flux, which can be counteracted by averaging the inverted fluxes over a longer time. Secondly, processes of convection and diffusion vary with the density ratios, which are seldomly constant in natural situations. Thirdly, the developing layers of higher-density water can be so thin that other boundary conditions (heat conduction to the stream bed, geometry of the bed, stream flow velocities, etc.) influence the results as well.

7

8

Conclusions

This thesis proposes a new perspective to quantify boil seepage. Where previous studies approached boil seepage measurements from a groundwater perspective or a more generic perspective, this thesis investigates whether individual boils can be measured from a surface water perspective. We hypothesized that detailed modelling of density-driven flows in the surface water allowed the inversion of the boil seepage flux from high-resolution measurements of the temperature profile in the water body. Based on this hypothesis, we formulated our research question. Our four research sub-questions (Section 1.5) constitute a structured approach to answer the main research question. In this chapter, Sections 8.1 until 8.4 answer these sub-questions. Section 8.5 concludes whether we can quantify a boil seepage flux from a model inversion of high-resolution temperature data, and Section 8.6 sets forth the outlook for this approach.

8.1 3-D enhanced-resolution DTS measurements

To infer the boil seepage flux from a high-resolution temperature profile, we first needed to explore the opportunities for high-resolution temperature measurements. Therefore, Research sub-question 1 was introduced to find out how we can build a measurement set-up that efficiently measures detailed water temperature profiles above a boil.

Chapter 3 shows that the signal decay in coil-wrapped fibre-optic cables yields several disadvantages for DTS measurements. Additionally, coil-wrapped DTS is less suitable for acquiring high-resolution measurements in three spatial dimensions, as it only enhances the resolution in one spatial dimension. Arranging a bunch of coils in a grid to reach a high resolution in multiple dimensions is not desirable, as a high number of densely spaced support tubes influences the flow profiles too much. Solar irradiation on the support tubes with a different heat capacity could also indirectly affect the temperature measurements along the full length of each coil (Hilgersom et al., 2016d).

In Chapter 4, we designed a set-up that provides a high resolution in three dimensions. The cable is woven through a PVC cage, reducing the number of cable bends and the direct contact with the PVC auxiliary construction. Another major advantage is the freedom to vary the spatial resolution to one's requirements, by selecting the required spacing between the horizontal nets of cables and selecting PVC tubes of a different diameter as vertical bars. When correcting for the longitudinal thermal expansion of the cable, the location of the temperature samples within the cage can be easily calibrated.

The 3-D dense DTS set-up was applied in laboratory and field conditions. In the laboratory, the set-up measured the temperature above a simulated saline seepage source. The detailed temperature profile revealed the dysfunctionality of the laboratory set-up, where the inflowing water seeped into the surface water via an unexpected flow path. The initial upward plumes in the case of a warm and saline seepage inflow potentially indicated the development of small-scale convection cells. At a later stage, a sharp temperature gradient became clear, which is expected for double-diffusive convection and clearly contrasted the more diffuse interface in the case of a cold and saline inflow. The observed horizontal disconti-

nuities might have resulted from the cable nets themselves.

In the field, the observations for boils with a salinity that contrasted the surface water salinity can be explained by the theory of double-diffusive phenomena. Most interestingly, the DTS set-up revealed the accumulation of sediment around boils and potential salt-fingers above a fresher and colder seepage inflow.

The laboratory and field results support the conclusion that the developed measurement set-up is well able to measure detailed 3-D temperature profiles. Once the location of the cable is calibrated and the correction procedure for the cable's thermal expansion is scripted, the 3-D locations of the sampling points can be efficiently derived from the measurements.

8.2 Double-diffusive transport modelling

For the inversion of a boil seepage flux from the temperature profile, we need a numerical model that properly simulates the transport of heat and salt in environments where double-diffusive phenomena occur. Detailed transport models often require a fine mesh and accordingly long computation times. In our approach to answer Research sub-question 2, we extended an existing free-surface model with a comprehensive salt and heat transport module to simulate detailed density-driven flow processes. Moreover, additional terms allowed a quasi 3-D axisymmetric solution of the governing Navier-Stokes equations.

In Chapter 5, the model applicability was first tested excluding the additional axisymmetric terms. The simulation of salt and heat transport in a laboratory-scale solar pond provided a good test case, because of data availability, the extreme density gradients, and the general believe that a 3-D model is not required to simulate the general structure of double-diffusive convection (Molemaker and Dijkstra, 1997).

The model results compared reasonably to the measured temperature profile in the solar pond. The model exaggerated the heat transport along the strongly sloping bed of the pond, yielding a decrease in heating of the lower convective zone of maximum 10 % during daytime. However, the general processes in the pond were well simulated. The density gradients even induced small seiches in the free-surface model. These seiches were too small to physically observe in the laboratory pond, but their occurrence is not illogical and shows the merit of free-surface models for water bodies with strong density gradients. The modelling of the atmospheric exchange fluxes and extinction of shortwave radiation appeared to perform sufficiently.

Chapter 6 showed qualitatively that the axisymmetric implementation of the model was able to simulate the expected double-diffusive phenomena. Moreover, an analytical benchmark study, which was specifically derived for this axisymmetric model set-up, quantitatively demonstrated the correct horizontal growth of a cold and saline layer from a central seepage inflow under laminar flow conditions.

In conclusion, the extended 2-DV model appeared to perform well as a replacement for a 3-D model, where a dense mesh in the third spatial dimension would be required. We stress that the model does not predict the exact locations of smaller-scale convection cells in double-diffusive systems, because these are induced by

8

small disturbances on the molecular scale. The modelling approach is efficient, as the computation time is approximately equal to that of a 2-DV grid set-up. Although the detailed density-driven processes still require a dense mesh, which inevitably yields relatively large computation times, we have demonstrated that an axisymmetric modelling approach performs well while significantly reducing the computation times.

8.3 Modelling the temperature measurements

Before being able to infer a boil seepage flux from temperature profiles in the surface water, the forward model performance needs to be tested (Research sub-question 3). Chapter 7 compared the measured and modelled temperature profiles in a controlled laboratory environment. The chapter concluded that the agreement between measurements and model was insufficient to confidently employ the model as an inversion tool for boundary fluxes.

A first reason for the dissimilarity between the measured and modelled temperatures was that the laboratory set-up appeared to function differently from what was assumed in the model. Because the exact flow paths of the seepage in the laboratory set-up were unknown, the model did not simulate the seepage inflow properly. Of course, this does not disprove the model capability to simulate temperature distributions for a known seepage inflow. We therefore recommend improved laboratory studies with better predictable boundary conditions.

A more important complication is the random nature in which double-diffusive convection cells appear. Although the model can represent the same signatures of double-diffusive processes as were observed in the measurements, their locations are less predictable. This is a consequence of processes on sub-grid scale: small variations in temperature and salinity can change the flow processes on a larger scale. Another issue is the relatively high influence of boundary conditions when the developing higher-density layer is still thin. These issues influence the model results in comparison with the measurements. We conclude that the measurements and the numerical simulations do not match properly for the current model results, and there are still major concerns if numerical simulations on this scale will yield good results in future applications.

8.4 Modernizing the rising bubble technique

The inversion of a boil seepage flux from an axisymmetric model is only possible when the horizontal flow velocities through the drainage canal are negligible. For this reason, discharge measurements should be performed in these canals during field applications of these seepage measurements. Chapter 2 has shown how digital image processing techniques facilitate the rising bubble technique for discharge measurement in streams of varying nature. It further discussed the potential for automization of the measurement method. In the following, we explore the applicability of the rising bubble technique to determine whether the flow through a polder drainage canal approaches zero (Research sub-question 4).

Chapter 2 concludes that the results of the rising bubble technique with the

introduced photo-integration method look promising for natural streams. Even in turbulent streams, the effect of eddies on the rising bubble paths can largely be mitigated by averaging the results of a higher number of photographs. In drainage canals where boils occur, flow velocities are generally low. The accuracy of the measurement method decreases when the horizontally travelled distance of the air bubbles decreases for low flow velocities. However, when compared to inaccuracies of other discharge measurement methods, the bubble displacement can still be determined with 2 % accuracy from the images in cases where fog, heavy rain or bright sunlight do not abate the visibility of the air bubbles on the water surface. Besides, the accuracy of the discharge measurements becomes less relevant when the method is solely used to determine the significance of the stream discharge for the boil seepage modelling.

Chapter 2 has shown how modern image processing orthorectifies images based on four reference points in order to correctly display the distances within the surface between these points. This reduces the processing time for deriving the bubble displacements from a photograph. Other image processing techniques could automate the tracing of reference points and surfacing air bubbles in the image, even in cases where scattering sunlight complicates the manual tracing of these bubbles. This facilitates automatic discharge measurements, which could be desirable when the method is applied with boil seepage measurements over a longer period. Chapter 2 recommends further research to pattern recognition techniques that support the automization of the rising bubble technique.

Although we did not apply the method in this research, modernizations in the rising bubble technique can facilitate measurements in channels with a low flow velocity. Even under low flow conditions, the method can still indicate whether the stream discharge is negligible. Care should be taken that the air bubbles should not be released in the stratified water body near the boil. When in addition pattern recognition techniques are applied to the photographs, the method has the potential to function automatically. Therefore, we recommend considering the rising bubble technique when applying an axisymmetric model to infer the boil seepage.

8.5 Seepage flux inversion from water temperatures

With these preliminary conclusions, we answer the main research question: how can we measure and model the boil seepage flux from a surface water perspective?

In general, we can conclude that double-diffusive phenomena complicate the inversion of the boil seepage flux from 3-D temperature profiles in the surface water. It is possible to model the occurrence of the phenomena themselves, but the exact locations of convection cells appear unpredictable on the model scale. This is caused by the molecular scale on which the double-diffusive phenomena develop, as well as the coincidental locations where convection cells start to develop: a small perturbation in flow, temperature, or salinity can influence the cell locations on larger scale. Moreover, in the case of a thin bottom layer of seepage water, small deviations of the measured and modelled interface locations have relatively large effects on the inversion of the boundary flux.

In conclusion, discrepancies in the locations of convection cells and the boundary conditions lead to inconsistencies between the model and the actual temperature profiles, making the inversion of a boundary flux less accurate.

With our current knowledge, no claims can be made whether these inaccuracies can be mitigated by averaging the inferred seepage flux over a longer period. The local temperature deviations might highly influence the inversion, leading to large noise in the outcome. We recommend testing this in an improved laboratory set-up. In the case of a positive outcome, the method could be applied for the inversion of the seepage flux from natural boils.

8.6 Outlook

This section presents our view on the future applicability of surface water monitoring and modelling for boil seepage inversion. The currently selected approach has not yet yielded results that make it a reliable method for future use. We recommend further exploration of this approach with controlled laboratory measurements and tests of the model accuracy for these known boundary conditions.

Zooming out from the current approach, we do see potential for the estimation of seepage fluxes from detailed surface water temperature profiles. DTS makes temperature a very useful tracer for this purpose. This thesis has shown how DTS can profile the surface water temperature in high detail. Tracers like salts do currently not provide the option to monitor with such a high spatial and time resolution. Other measurement methods like seepage meters potentially affect the boil seepage paths and fluxes.

The most promising approach might be the application of high-resolution DTS to measure the interface growth for an unconditionally stable situation. This situation, with a colder and saline seepage inflow, occurs for most boils in deep polders, as these boils are usually more saline and during part of the year also colder than the surface water. By starting from a completely mixed situation, the interface growth could be best observed. Chapter 7 has shown our model's capability to simulate such a situation in a forward modelling approach. However, more basic transport models might suffice in this case. For example, Chapter 6 derived an analytical solution for this specific case. We recommend further research to the performance of this approach in a practical set-up.

Acknowledgements

It is always hard to start with a word of thanks, as so many people have somehow been a support over all the years that lead to the completion of this dissertation. I choose to start with those who have been the most visible support: my supervisors and co-authors. I would like to thank them for all their critical comments, which improved the research output and taught me a lot at the same time. Nick, thank you for remaining positive all the time about how we could reach our goals. In the end, the result is now in our hands. And despite the fact that we may not have completely reached the final goal of this research, this thesis includes a lot of valuable results. Marcel, thank you for your willingness to step in as a supervisor at a later stage of the research. I admire your patience in teaching me about numerical modelling techniques and in carefully analysing how we could improve our model.

Next, I would like to thank everyone in the Watermanagement department for being there when I needed advice or just a chat next to the coffee machine. I enjoyed all these moments, not only at the serious occasions, but also the less serious occasions like section activities, the yearly fieldwork course, colloquium drinks, and barbecues. In particular, I thank all my fellow PhD students. I enjoyed the discussions that we had and had a great time during the PhD activities.

A special word of thanks goes out to the PhD students with whom I was lucky to share an office. Ruud, Luca, and Yang: thank you for all these moments when I could rely on you to discuss all the things that were related to our research, and the things that were absolutely not.

Whether one likes it or not, a PhD process also involves a lot of administration. I would like to thank Betty, Hanneke, Luz, and Lydia, not only for being a good support with this respect, but also for the fact that I could always walk into your office for a relaxing chat (and of course some sweets).

This thesis relies on a lot of lab and field measurements, which can never be done alone. First of all, I would like to thank Wim, Thom, Nick, Olivier, Tim, and Rolf for thinking along with me in designing the experiments. Especially Wim taught me a lot about hydrological measurement set-ups. Tim, Wouter, and Marlies were a great support for me in the design and construction of the 3D DTS set-up. I admire their patience, which is indispensable for any DTS set-up, but this one in particular. Last but not least, I would like to thank everyone that joined to the field to make sure the data could actually be acquired: Shervan, Ruud, Stijn, Luca, Dong, Anna, Aagje, Remko, Gert, Koen, Davíd, and Mirjam. Thanks a lot! Anna and Tim, I would also like to mention here the time we spent on converting our findings about coil-wrapped DTS into a paper. It took perhaps a little more time than we hoped for, but it was great fun working together with you on this.

Outside TU Delft, I was lucky that I could discuss the measurements with, and borrow equipment from, several persons at Deltares, which should be mentioned

here: Perry, Gu and Joost, thanks a lot for sharing your knowledge and advising me on my measurement plans. The DTS set-up that I developed imposed a high challenge for the analysis of the results: the people of Silixa gave me some advise on the strange artefacts in the that was definitely helpful! There are also several persons outside TU Delft that greatly supported me in the actual execution of my field experiments: Mr. Avis (Nieuw-Vennep), Mr. Dorrepaal (Noordplas) and Miss Schneider (Kortenhoef), thank you for hosting the field measurements. I also would like to acknowledge Rob Tijsen (Waternet) for making me aware of the fresh boils in Kortenhoef.

In 2013, I was lucky that I could visit the research groups of Scott Tyler (University of Nevada, Reno) and John Selker (Oregon State University, Corvallis). First of all, both are great fieldworkers who taught me a lot! I further would like to acknowledge them for all their advise that contributed to this thesis. John, your lessons on DTS, your large support for the coil-wrapped DTS paper, and your patience in together thinking over my seepage measurement experiments were absolutely indispensable for this thesis. I will never forget the only Thanksgiving I have celebrated up till now: thank you for all your hospitality and kindness. Scott, in the end it seems that we have actually found fair modelling results for this strange side-sloped solar pond. Of course, I should mention Francisco Suárez here: Pancho, it took quite some time and a whole bunch of e-mails up and down to Chile, but it has finally resulted in nice modelling results for the slope in this pond. Thanks a lot for your patience and thinking along with me on how to overcome all the challenges.

Last but not least, a PhD process cannot be finished without getting sufficient support in your private life. I would like to thank my friends for being there when I needed a chat and some distraction: without you, I would have definitely run crazy over my work. I am deeply grateful to my parents, my sister and brother-in-law: your moral support was very valuable over the past years. Finally, I would like to thank Annelies, my love, who shared with me all the stressful and joyful moments that a PhD student comes across during the final years of his PhD research. I know that, at times, I was a little hard to cope with, and I am so grateful for your understanding and your support throughout this process! I hope that we can enjoy life together more relaxed in all the years to come.

Appendix A

Cell depth integration with the Leibniz integral rule

A

When the continuity, momentum and transport equations are integrated over the cell depth, the Leibniz integral rule is applied to the time derivatives and the horizontal spatial derivatives. Here, we show the cell depth integration of $\frac{\partial u}{\partial t}$ and $\frac{\partial uu}{\partial r}$:

$$\int_{z_{k-\frac{1}{2}}}^{z_{k+\frac{1}{2}}} \frac{\partial u}{\partial t} dz = \frac{\partial u_k h_k}{\partial t} - u \frac{\partial z}{\partial t}\bigg|_{z_{k-\frac{1}{2}}}^{z_{k+\frac{1}{2}}} \tag{A.1}$$

$$\int_{z_{k-\frac{1}{2}}}^{z_{k+\frac{1}{2}}} \frac{\partial uu}{\partial r} dz = \frac{\partial u_k u_k h_k}{\partial r} - u\hat{u} \frac{\partial z}{\partial r}\bigg|_{z_{k-\frac{1}{2}}}^{z_{k+\frac{1}{2}}} \tag{A.2}$$

The derivatives $\frac{\partial ur}{\partial r}$, $\frac{\partial w}{\partial t}$, $\frac{\partial uw}{\partial r}$, $\frac{\partial p}{\partial r}$, $\frac{\partial c}{\partial t}$, and $\frac{\partial c}{\partial r}$ in Equations 6.1, 6.2, 6.3, and 6.7 are integrated in a similar fashion.

Appendix B

Full axisymmetric discretization of the non-hydrostatic momentum and transport equations

B

B.1 U-momemtum

$$\frac{u_{i+\frac{1}{2},k}^{n+\theta_u}}{\theta_u \Delta t} + \frac{\overline{\omega_{i+\frac{1}{2},k+\frac{1}{2}}^{n}}^{r}\left(\hat{u}_{i+\frac{1}{2},k+\frac{1}{2}}^{n+\theta_u} - u_{i+\frac{1}{2},k}^{n+\theta_u}\right)}{\overline{h_{i+\frac{1}{2},k}^{n}}^{r}} - \frac{\overline{\omega_{i+\frac{1}{2},k-\frac{1}{2}}^{n}}^{r}\left(\hat{u}_{i+\frac{1}{2},k-\frac{1}{2}}^{n+\theta_u} - u_{i+\frac{1}{2},k}^{n+\theta_u}\right)}{\overline{h_{i+\frac{1}{2},k}^{n}}^{r}} -$$

$$\nu_{v;i+\frac{1}{2},k+\frac{1}{2}}^{n}\frac{u_{i+\frac{1}{2},k+1}^{n+\theta_u} - u_{i+\frac{1}{2},k}^{n+\theta_u}}{\overline{h_{i+\frac{1}{2},k}^{n}}^{r}\,\overline{h_{i+\frac{1}{2},k+\frac{1}{2}}^{n}}^{rz}} + \nu_{v;i+\frac{1}{2},k-\frac{1}{2}}^{n}\frac{u_{i+\frac{1}{2},k}^{n+\theta_u} - u_{i+\frac{1}{2},k-1}^{n+\theta_u}}{\overline{h_{i+\frac{1}{2},k}^{n}}^{r}\,\overline{h_{i+\frac{1}{2},k-\frac{1}{2}}^{n}}^{rz}} = \frac{u_{i+\frac{1}{2},k}^{n}}{\theta_u \Delta t} -$$

$$\frac{\overline{\phi_{i+1,k}^{n}\,\overline{y_{1;i+1}}}^{r}\left(\hat{u}_{i+1,k}^{n} - u_{i+\frac{1}{2},k}^{n}\right) - \overline{\phi_{i,k}^{n}\,\overline{y_{1;i}}}^{r}\left(\hat{u}_{i,k}^{n} - u_{i+\frac{1}{2},k}^{n}\right)}{\overline{h_{i+\frac{1}{2},k}^{n}}^{r}\,\overline{y_{1;i+\frac{1}{2}}}^{r}\Delta r_{i+\frac{1}{2}}} + \boxed{\frac{\alpha}{\overline{y_{1;i+\frac{1}{2}}}^{r}}u_{i+\frac{1}{2},k}^{n}u_{i+\frac{1}{2},k}^{n}} -$$

$$g\frac{\zeta_{i+1}^{n+\theta_\zeta} - \zeta_i^{n+\theta_\zeta}}{\Delta r_{i+\frac{1}{2}}} - \frac{q_{i+1,k}^{n}h_{i+1,k}^{n}y_{1;i+1} - q_{i,k}^{n}h_{i,k}^{n}y_{1;i}}{\overline{h_{i+\frac{1}{2},k}^{n}}^{r}\,\overline{y_{1;i+\frac{1}{2}}}^{r}\Delta r_{i+\frac{1}{2}}} + \overline{q_{i+\frac{1}{2},k+\frac{1}{2}}^{n}}^{rz}\frac{z_{i+1,k+\frac{1}{2}}^{n} - z_{i,k+\frac{1}{2}}^{n}}{\overline{h_{i+\frac{1}{2},k}^{n}}^{r}\Delta r_{i+\frac{1}{2}}} -$$

$$\overline{q_{i+\frac{1}{2},k-\frac{1}{2}}^{n}}^{rz}\frac{z_{i+1,k-\frac{1}{2}}^{n} - z_{i,k-\frac{1}{2}}^{n}}{\overline{h_{i+\frac{1}{2},k}^{n}}^{r}\Delta r_{i+\frac{1}{2}}} + \boxed{\frac{\overline{\alpha q_{i+\frac{1}{2},k}^{n}}^{r}}{\overline{y_{1;i+\frac{1}{2}}}^{r}}} - \frac{g}{\rho_0}\frac{\overline{h_{i+\frac{1}{2},k}^{n}}^{r}}{2}\frac{\rho_{i+1,k}^{n} - \rho_{i,k}^{n}}{\Delta r_{i+\frac{1}{2}}} -$$

$$\frac{g}{\rho_0}\sum_{j=1}^{k-1}\left(\overline{h_{i+\frac{1}{2},j}^{n}}^{r}\frac{\rho_{i+1,j}^{n} - \rho_{i,j}^{n}}{\Delta r_{i+\frac{1}{2}}} + \left(\overline{\rho_{i+\frac{1}{2},j}^{n}}^{r} - \overline{\rho_{i+\frac{1}{2},k}^{n}}^{r}\right)\frac{h_{i+1,j}^{n} - h_{i,j}^{n}}{\Delta r_{i+\frac{1}{2}}}\right) +$$

$$\frac{\nu_{h;i+1,k}^{n}y_{1;i+1}h_{i+1,k}^{n}}{\overline{h_{i+\frac{1}{2},k}^{n}}^{r}\,\overline{y_{1;i+\frac{1}{2}}}^{r}\Delta r_{i+\frac{1}{2}}}\frac{u_{i+\frac{3}{2},k}^{n} - u_{i+\frac{1}{2},k}^{n}}{\Delta r_{i+1}} -$$

$$\frac{\nu_{h;i,k}^{n}y_{1;i}h_{i,k}^{n}}{\overline{h_{i+\frac{1}{2},k}^{n}}^{r}\,\overline{y_{1;i+\frac{1}{2}}}^{r}\Delta r_{i+\frac{1}{2}}}\frac{u_{i+\frac{1}{2},k}^{n} - u_{i-\frac{1}{2},k}^{n}}{\Delta r_i} - \boxed{\frac{\alpha}{\overline{y_{1;i+\frac{1}{2}}}^{r}}u_{i+\frac{1}{2},k}^{n}\frac{\overline{\nu_{h;i+\frac{1}{2},k}^{n}}^{r}}{r_{i+\frac{1}{2}}}}$$

$$\text{(B.1)}$$

B.2 W-momemtum

$$\frac{w_{i,k+\frac{1}{2}}^{n+\theta_w}}{\theta_w \Delta t} + \frac{\overline{\omega_{i,k+1}^n}^z \left(\hat{w}_{i,k+1}^{n+\theta_w} - w_{i,k+\frac{1}{2}}^{n+\theta_w} \right)}{\overline{h_{i,k+\frac{1}{2}}^n}^z} - \frac{\overline{\omega_{i,k}^n}^z \left(\hat{w}_{i,k}^{n+\theta_w} - w_{i,k+\frac{1}{2}}^{n+\theta_w} \right)}{\overline{h_{i,k+\frac{1}{2}}^n}^z}$$

$$-v_{v;i,k+1}^n \frac{w_{i,k+\frac{3}{2}}^{n+\theta_w} - w_{i,k+\frac{1}{2}}^{n+\theta_w}}{\overline{h_{i,k+\frac{1}{2}}^n}^z h_{i,k+1}^n} + v_{v;i,k}^n \frac{w_{i,k+\frac{1}{2}}^{n+\theta_w} - w_{i,k-\frac{1}{2}}^{n+\theta_w}}{\overline{h_{i,k+\frac{1}{2}}^n}^z h_{i,k}^n} = \frac{w_{i,k+\frac{1}{2}}^n}{\theta_w \Delta t}$$

$$-\frac{\overline{\phi_{i+\frac{1}{2},k+\frac{1}{2}}^n}^z \overrightarrow{y_{1;i+\frac{1}{2}}} \left(\hat{w}_{i+\frac{1}{2},k+\frac{1}{2}}^n - w_{i,k+\frac{1}{2}}^n \right) - \overline{\phi_{i-\frac{1}{2},k+\frac{1}{2}}^n}^z \overrightarrow{y_{1;i-\frac{1}{2}}} \left(\hat{w}_{i-\frac{1}{2},k+\frac{1}{2}}^n - w_{i,k+\frac{1}{2}}^n \right)}{\overline{h_{i,k+\frac{1}{2}}^n}^z y_{1;i} \Delta r_i}$$

$$+ \boxed{\frac{\alpha}{y_{1;i}} \frac{\overline{\phi_{i,k+\frac{1}{2}}^n}^{rz}}{\overline{h_{i,k+\frac{1}{2}}^n}^z} w_{i,k+\frac{1}{2}}^n} - \frac{q_{i,k+1}^n}{\overline{h_{i,k+\frac{1}{2}}^n}^z} + \frac{q_{i,k}^n}{\overline{h_{i,k+\frac{1}{2}}^n}^z}$$

$$+ \frac{v_{h;i+\frac{1}{2},k+\frac{1}{2}}^n \overline{y_{1;i+\frac{1}{2}}}^r \overline{h_{i-\frac{1}{2},k+\frac{1}{2}}^n}^{rz}}{\overline{h_{i,k+\frac{1}{2}}^n}^z y_{1;i} \Delta r_i} \frac{w_{i+1,k+\frac{1}{2}}^n - w_{i,k+\frac{1}{2}}^n}{\Delta r_{i+\frac{1}{2}}}$$

$$- \frac{v_{h;i-\frac{1}{2},k+\frac{1}{2}}^n \overline{y_{1;i-\frac{1}{2}}}^r \overline{h_{i-\frac{1}{2},k+\frac{1}{2}}^n}^{rz}}{\overline{h_{i,k+\frac{1}{2}}^n}^z y_{1;i} \Delta r_i} \frac{w_{i,k+\frac{1}{2}}^n - w_{i-1,k+\frac{1}{2}}^n}{\Delta r_{i-\frac{1}{2}}}$$

$$(B.2)$$

B.3 Transport equation

$$\frac{c_{i,k}^{n+1}}{\Delta t} + \frac{\omega_{i,k+\frac{1}{2}}^{n+1}\hat{c}_{i,k+\frac{1}{2}}^{n+1}}{h_{i,k}^{n+1}} - \frac{\omega_{i,k-\frac{1}{2}}^{n+1}\hat{c}_{i,k-\frac{1}{2}}^{n+1}}{h_{i,k}^{n+1}} - \frac{D_{v;i,k+\frac{1}{2}}}{h_{i,k}^{n+1}}\frac{c_{i,k+1}^{n+1}-c_{i,k}^{n+1}}{\overline{h_{i,k+\frac{1}{2}}^{n+1}}^{z}} +$$

$$\frac{D_{v;i,k-\frac{1}{2}}}{h_{i,k}^{n+1}}\frac{c_{i,k}^{n+1}-c_{i,k-1}^{n+1}}{\overline{h_{i,k-\frac{1}{2}}^{n+1}}^{z}} = \frac{c_{i,k}^{n}h_{i,k}^{n}}{\Delta t h_{i,k}^{n+1}} - \frac{\phi_{i+\frac{1}{2},k}^{n}\overrightarrow{y_{1;i+\frac{1}{2}}}\hat{c}_{i+\frac{1}{2},k}^{n}}{y_{1;i}h_{i,k}^{n+1}\Delta r} + \frac{\phi_{i-\frac{1}{2},k}^{n}\overrightarrow{y_{1;i-\frac{1}{2}}}\hat{c}_{i-\frac{1}{2},k}^{n}}{y_{1;i}h_{i,k}^{n+1}\Delta r} +$$

$$\frac{D_{h;i+\frac{1}{2},k}\overline{y_{1;i+\frac{1}{2}}}^{r}\overline{h_{i+\frac{1}{2},k}^{n}}^{r}}{y_{1;i}h_{i,k}^{n+1}\Delta r}\frac{c_{i+1,k}^{n}-c_{i,k}^{n}}{\Delta r} - \frac{D_{h;i-\frac{1}{2},k}\overline{y_{1;i-\frac{1}{2}}}^{r}\overline{h_{i-\frac{1}{2},k}^{n}}^{r}}{y_{1;i}h_{i,k}^{n+1}\Delta r}\frac{c_{i,k}^{n}-c_{i-1,k}^{n}}{\Delta r} -$$

$$\frac{D_{h;i+\frac{1}{2},k}\overline{y_{1;i+\frac{1}{2}}}^{r}\overline{h_{i+\frac{1}{2},k}^{n}}^{r}}{y_{1;i}h_{i,k}^{n+1}\Delta r}\frac{\overline{c_{i+\frac{1}{2},k+1}^{n}}^{r}-\overline{c_{i+\frac{1}{2},k-1}^{n}}^{r}}{\overline{h_{i+\frac{1}{2},k+\frac{1}{2}}^{n}}^{rz}+\overline{h_{i+\frac{1}{2},k-\frac{1}{2}}^{n}}^{rz}}\frac{\overline{z_{i+1,k}^{n}}^{z}-\overline{z_{i,k}^{n}}^{z}}{\Delta r} +$$

$$\frac{D_{h;i-\frac{1}{2},k}\overline{y_{1;i-\frac{1}{2}}}^{r}\overline{h_{i-\frac{1}{2},k}^{n}}^{r}}{y_{1;i}h_{i,k}^{n+1}\Delta r}\frac{\overline{c_{i-\frac{1}{2},k+1}^{n}}^{r}-\overline{c_{i-\frac{1}{2},k-1}^{n}}^{r}}{\overline{h_{i-\frac{1}{2},k+\frac{1}{2}}^{n}}^{rz}+\overline{h_{i-\frac{1}{2},k-\frac{1}{2}}^{n}}^{rz}}\frac{\overline{z_{i,k}^{n}}^{z}-\overline{z_{i-1,k}^{n}}^{z}}{\Delta r} -$$

$$\frac{D_{h;i,k+\frac{1}{2}}}{h_{i,k}^{n+1}}\frac{z_{i+1,k+\frac{1}{2}}^{n}-z_{i-1,k+\frac{1}{2}}^{n}}{2\Delta r}\frac{\overline{c_{i+1,k+\frac{1}{2}}^{n}}^{z}-\overline{c_{i-1,k+\frac{1}{2}}^{n}}^{z}}{2\Delta r} +$$

$$\frac{D_{h;i,k+\frac{1}{2}}}{h_{i,k}^{n+1}}\left(\frac{z_{i+1,k+\frac{1}{2}}^{n}-z_{i-1,k+\frac{1}{2}}^{n}}{2\Delta r}\right)^{2}\frac{c_{i,k+1}^{n}-c_{i,k}^{n}}{\overline{h_{i,k+\frac{1}{2}}^{n}}^{z}} -$$

$$\frac{D_{h;i,k-\frac{1}{2}}}{h_{i,k}^{n+1}}\left(\frac{z_{i+1,k-\frac{1}{2}}^{n}-z_{i-1,k-\frac{1}{2}}^{n}}{2\Delta r}\right)^{2}\frac{c_{i,k}^{n}-c_{i,k-1}^{n}}{\overline{h_{i,k-\frac{1}{2}}^{n}}^{z}}$$

$$(B.3)$$

References

Adams, E. E., Cosler, D. J., and Helfrich, K. R.: Evaporation from heated water bodies: Predicting combined forced plus free convection, Water Resour. Res., 26, 425–435, doi:10.1029/WR026i003p00425, 1990.

Anderson, M. P.: Heat as a Ground Water Tracer, Ground Water, 43, 951–968, doi:10.1111/j.1745-6584.2005.00052.x, 2005.

Angermann, L., Krause, S., and Lewandowski, J.: Application of heat pulse injections for investigating shallow hyporheic flow in a lowland river, Water Resour. Res., 48, W00 P02, doi:10.1029/2012WR012564, 2012.

Arnon, A., Lensky, N. G., and Selker, J. S.: High-resolution temperature sensing in the Dead Sea using fiber optics, Water Resour. Res., 50, 1756–1772, doi:10.1002/2013WR014935, 2014a.

Arnon, A., Selker, J., and Lensky, N.: Correcting artifacts in transition to a wound optic fiber: Example from high-resolution temperature profiling in the Dead Sea, Water Resour. Res., 50, 5329–5333, doi:10.1002/2013WR014910, 2014b.

Aybers, N. and Tapucu, A.: The motion of gas bubbles rising through stagnant liquid, Wärme- und Stoffübertragung, 2, 118–128, doi:10.1007/BF01089056, 1969a.

Aybers, N. and Tapucu, A.: Studies on the drag and shape of gas bubbles rising through a stagnant liquid, Wärme- und Stoffübertragung, 2, 171–177, doi:10.1007/BF00751164, 1969b.

Bakker, M., Caljé, R., Schaars, F., Van der Made, K.-J., and De Haas, S.: An active heat tracer experiment to determine groundwater velocities using fiber optic cables installed with direct push equipment, Water Resour. Res., 51, 2760–2772, doi:10.1002/2014WR016632, 2015.

Batchelor, G.: An introduction to fluid dynamics, Cambridge Univ. Pr., 1967.

Bennett, G., Reilly, T., and Hill, M.: Technical training notes in ground-water hydrology: radial flow to a well, Tech. rep., US Geological Survey, 1990.

Berendsen, H. and Stouthamer, E.: Late Weichselian and Holocene palaeogeography of the Rhine-Meuse delta, the Netherlands, Palaeogeography, Palaeoclimatology, Palaeoecology, 161, 311–335, doi:10.1016/S0031-0182(00)00073-0, 2000.

Bergman, T. L., Incropera, F. P., and Lavine, A. S.: Fundamentals of heat and mass transfer, John Wiley & Sons, 2011.

Berthold, S. and Börner, F.: Detection of free vertical convection and double-diffusion in groundwater monitoring wells with geophysical borehole measurements, Environ. Geol., 54, 1547–1566, doi:10.1007/s00254-007-0936-y, 2008.

Bianchin, M., Smith, L., and Beckie, R.: Quantifying hyporheic exchange in a tidal river using temperature time series, Water Resour. Res., 46, W07 507, 2010.

Bilgen, E. and Richard, M.-A.: Horizontal concrete slabs as passive solar collectors, Sol. Energy, 72, 405–413, doi:10.1016/S0038-092X(02)00014-2, 2002.

Bose, D.: Narinder Singh Kapany - a pioneer in fibre optics, Current Science, 98, 857–858, 2010.

Bouyoucos, G.: Effects of temperature on some of the most important physical process in soils, Mich. Coll. Ag. Tech. Bull., 24, 63, 1915.

Branco, B. and Torgersen, T.: Predicting the onset of thermal stratification in shallow inland waterbodies, Aquatic Sciences, 71, 65–79, doi:10.1007/s00027-009-8063-3, 2009.

Bredehoeft, J. and Papadopulos, I.: Rates of vertical groundwater movement estimated from the earth's thermal profile, Water Resour. Res., 1, 325–328, 1965.

Briggs, M. A., Lautz, L. K., McKenzie, J. M., Gordon, R. P., and Hare, D. K.: Using high-resolution distributed temperature sensing to quantify spatial and temporal variability in vertical hyporheic flux, Water Resour. Res., 48, W02527, doi:10.1029/2011WR011227., 2012.

Brodie, R., Baskaran, S., Ransley, T., and Spring, J.: Seepage meter: Progressing a simple method of directly measuring water flow between surface water and groundwater systems, Australian Journal of Earth Sciences, 56, 3–11, doi:10.1080/08120090802541879, 2009.

Brown, D.: Decentering Distortion of Lenses, Photogramm. Eng., 32, 444–462, 1966.

Brown, D.: Close- range camera calibration, Photogramm. Eng., 37, 855–866, 1971.

Byrnes, R. and Webster, A.: Direct Measurement of Seepage from Earthen Channels, Australian Water Resources Council, Technical Paper No. 64, 1981.

Carpenter, J., Sommer, T., and Wüest, A.: Simulations of a double-diffusive interface in the diffusive convection regime, J. Fluid Mech., 711, 411–436, 2012.

Casulli, V. and Cheng, R. T.: Semi-implicit finite difference methods for three-dimensional shallow water flow, Int. J. Numer. Meth. Fl., 15, 629–648, doi:10.1002/fld.1650150602, 1992.

Casulli, V. and Stelling, G.: Numerical simulation of 3D quasi-hydrostatic, free-surface flows, Journal of Hydraulic Engineering, 124, 678–686, 1998.

Cathcart, T. P. and Wheaton, F. W.: Modeling temperature distribution in freshwater ponds, Aquacultural Engineering, 6, 237–257, doi:10.1016/0144-8609(87)90021-5, 1987.

Ciocca, F., Lunati, I., Van de Giesen, N., and Parlange, M. B.: Heated Optical Fiber for Distributed Soil-Moisture Measurements: A Lysimeter Experiment, Vadose Zone Journal, 11, 9851, doi:10.2136/vzj2011.0199, 2012.

Cirkel, D., Witte, J., and van der Zee, S.: Estimating seepage intensities from groundwater level time series by inverse modelling: A sensitivity analysis on wet meadow scenarios, J. Hydrol., 385, 132–142, 2010.

Conant, B.: Delineating and quantifying ground water discharge zones using streambed temperatures, Ground Water, 42, 243–257, 2004.

Conant, B. et al.: A PCE groundwater plume discharging to a river: influence of the streambed and near-river zone on contaminant distributions, Journal Contam. Hydrol., 73, 249–279, 2004.

Dages, C., Voltz, M., and Ackerer, P.: Parameterization and evaluation of a three-dimensional modelling approach to water table recharge from seepage losses in a ditch, J. Hydrol., 348, 350–362, 2008.

Dakin, J., Pratt, D., Bibby, G., and Ross, J.: Distributed optical fibre Raman temperature sensor using a semiconductor light source and detector, Electronics Letters, 21, 569–570, doi:10.1049/el:19850402, 1985.

De Jong, S., Slingerland, J., and Van de Giesen, N.: Fiber optic distributed temperature sensing for the determination of air temperature, Atmospheric Measurement Techniques, 8, 335–339, 2015.

De Louw, P.: Saline seepage in deltaic areas, Ph.D. thesis, VU University, Amsterdam, 2013.

De Louw, P., Oude Essink, G., Stuyfzand, P., and van der Zee, S.: Upward groundwater flow in boils as the dominant mechanism of salinization in deep polders, The Netherlands, J. Hydrol., 394, 494–506, doi:10.1016/j.jhydrol.2010.10.009, 2010.

De Louw, P., Vandenbohede, A., Werner, A., and Oude Essink, G.: Natural saltwater upconing by preferential groundwater discharge through boils, J. Hydrol., 490, 74–87, doi:10.1016/j.jhydrol.2013.03.025, 2013.

De Louw, P. G. B., Van der Velde, Y., and Van der Zee, S. E. A. T. M.: Quantifying water and salt fluxes in a lowland polder catchment dominated by boil seepage: a probabilistic end-member mixing approach, Hydrol. Earth Syst. Sci., 15, 2101–2117, doi:10.5194/hess-15-2101-2011, 2011.

De Villiers, J., Leuschner, F., and Geldenhuys, R.: Centi-pixel accurate real-time inverse distortion correction, in: Proceedings of SPIE, vol. 7266(11), SPIE, doi:10.1117/12.804771, optomechatronic Technologies 2008, 2008.

Delsman, J. R., Essink, G. H. P. O., Beven, K. J., and Stuyfzand, P. J.: Uncertainty estimation of end-member mixing using generalized likelihood uncertainty estimation (GLUE), applied in a lowland catchment, Water Resources Research, 49, 4792–4806, doi:10.1002/wrcr.20341, 2013.

Devernay, F. and Faugeras, O.: Automatic calibration and removal of distortion from scenes of structured environments, in: Proceedings of SPIE, vol. 2567, p. 62, 1995.

Devernay, F. and Faugeras, O.: Straight lines have to be straight, Machine Vision and Applications, 13, 14–24, 2001.

Dias, J. and Lopes, J.: Implementation and assessment of hydrodynamic, salt and heat transport models: The case of Ria de Aveiro Lagoon (Portugal), Environmental Modelling & Software, 21, 1–15, doi:10.1016/j.envsoft.2004.09.002, 2006.

Dong, C.: Probabilistic scenario-based decision making for water resources planning and management, Ph.D. thesis, TU Delft, Delft University of Technology, 2014.

Eckart, C. H.: The equation of state of water and sea water at low temperatures and pressures, Part 2 of Properties of water, American Journal of Science, 256, 225–240, 1958.

Elder, J.: Steady free convection in a porous medium heated from below, J. Fluid Mech., 27, 29–48, 1967a.

Elder, J.: Transient convection in a porous medium, Journal of Fluid Mechanics, 27, 609–623, 1967b.

Euser, T., Luxemburg, W. M. J., Everson, C. S., Mengistu, M. G., Clulow, A. D., and Bastiaanssen, W. G. M.: A new method to measure Bowen ratios using high-resolution vertical dry and wet bulb temperature profiles, Hydrol. Earth Syst. Sci., 18, 2021–2032, doi:10.5194/hess-18-2021-2014, 2014.

Food & Agriculture Organization (FAO): Seawater intrusion in coastal aquifers: guidelines for study, monitoring and control, FAO Water Reports, vol. 11, 1997.

Foppen, J. W., Orup, C., Adell, R., Poulalion, V., and Uhlenbrook, S.: Using multiple artificial DNA tracers in hydrology, Hydrol. Process., 25, 3101–3106, 2011.

Fringer, O., Armfield, S., and Street, R.: Reducing numerical diffusion in interfacial gravity wave simulations, Int. J. Numer. Methods Fl., 49, 301–329, 2005.

Fryer, J. and Brown, D.: Lens distortion for close-range photogrammetry, Photogrammetric Engineering and Remote Sensing, 52, 51–58, 1986.

Galletti, C., Parente, A., and Tognotti, L.: Numerical and experimental investigation of a mild combustion burner, Combustion and flame, 151, 649–664, 2007.

Giambastiani, B. M., Antonellini, M., Oude Essink, G. H., and Stuurman, R. J.: Saltwater intrusion in the unconfined coastal aquifer of Ravenna (Italy): A numerical model, J. Hydrol., 340, 91–104, doi:10.1016/j.jhydrol.2007.04.001, 2007.

Giestas, M., Joyce, A., and Pina, H.: The influence of non-constant diffusivities on solar ponds stability, Int. J. Heat Mass Tran., 40, 4379–4391, 1997.

Giestas, M., Pina, H. L., Milhazes, J. P., and Tavares, C.: Solar pond modeling with density and viscosity dependent on temperature and salinity, Int. J. Heat Mass Tran., 52, 2849–2857, doi:10.1016/j.ijheatmasstransfer.2009.01.003, 2009.

González, D., Amigo, J., Lorente, S., Bejan, A., and Suárez, F.: Constructal design of salt-gradient solar pond fields, Int. J. Energ. Res., 40, 1428–1446, doi:10.1002/er.3539, 2016.

Grattan, K. and Meggitt, B.: Optical fiber sensor technology: fundamentals, Kluwer Academic Publishers, 2000.

Hajos, S.: Neues Verfahren zur Messung kleiner Wassergeschwindigkeiten, Zentralblatt der Bauverwaltung, 24, 281–283, 1904.

Hansen, W.: Theorie zur Errechnung des Wasserstandes und der Strömungen in Randmeeren nebst Anwendungen, Tellus, 8, 287–300, doi:10.1111/j.2153-3490.1956.tb01227.x, 1956.

Hausner, M., Suárez, F., Glander, K., Giesen, N., Selker, J., and Tyler, S.: Calibrating Single-Ended Fiber-Optic Raman Spectra Distributed Temperature Sensing Data, Sensors, 11, 10 859–10 879, 2011.

Hausner, M. B., Wilson, K. P., Gaines, D. B., and Tyler, S. W.: Interpreting seasonal convective mixing in Devils Hole, Death Valley National Park, from temperature profiles observed by fiber-optic distributed temperature sensing, Water Resour. Res., 48, W05513, 2012.

Henderson-Sellers, B.: Calculating the surface energy balance for lake and reservoir modeling: A review, Reviews of Geophysics, 24, 625–649, doi:10.1029/RG024i003p00625, 1986.

Herschy, R.: Hydrometry; principles and practices, Wiley Interscience, 1978.

Herschy, R.: Streamflow measurement, Taylor & Francis, 1995.

Hilgersom, K., Berghuijs, W. R., Solcerova, A., and Van Emmerik, T.: Thermal energy balance model of a fiber-optic cable; data from a shallow urban pond, Delft, doi:10.4121/uuid:a946eca5-0901-4a09-a95a-0c028a6b1853, 2015.

Hilgersom, K., Suárez, F., Zijlema, M., Hausner, M., Tyler, S., and Van de Giesen, N.: A free-surface solar pond model with a sloping edge: model code and data, doi:10.4121/uuid:87829ef5-be45-40e7-a0a7-b4c514633e26, 2016a.

Hilgersom, K., Van de Giesen, N., De Louw, P., and Zijlema, M.: 3D Dense DTS: temperature data from waterbodies subject to thermohaline stratification - Laboratory measurements and field campaigns in the Noordplas Polder and at Kortenhoef, doi:10.4121/uuid:da1d236b-7d0a-4c67-9136-bf913a7aa1b2, 2016b.

Hilgersom, K., Van de Giesen, N., De Louw, P., and Zijlema, M.: 3D Dense distributed temperature sensing for measuring layered thermohaline systems, Water Resour. Res., 52, doi:10.1002/2016WR019119, 2016c.

Hilgersom, K., Van Emmerik, T., Solcerova, A., Berghuijs, W., Selker, J., and Van de Giesen, N.: Practical considerations for enhanced-resolution coil-wrapped distributed temperature sensing, Geosci. Instrum. Method. Data Syst., 5, 151–162, doi:10.5194/gi-5-151-2016, 2016d.

Hilgersom, K., Zijlema, M., and Van de Giesen, N.: An axisymmetric hydrodynamical model: model code and data, doi:10.4121/uuid:c0dce972-5a04-476f-8f3f-4ac34f40da1b, 2016e.

Hilgersom, K., Zijlema, M., and Van de Giesen, N.: An axisymmetric non-hydrostatic model for double-diffusive water systems, Geosci. Model Dev. Discuss., 2016, 1–21, doi:10.5194/gmd-2016-176, 2016f.

Hilgersom, K. P.: Closing the Water Balance of Lake Lauwersmeer, Master's thesis, Delft University of Technology, 2010.

Hilgersom, K. P. and Luxemburg, W. M. J.: Technical Note: How image processing facilitates the rising bubble technique for discharge measurement, Hydrol. Earth Syst. Sci., 16, 345–356, doi:10.5194/hess-16-345-2012, 2012.

Hirsch, C.: Numerical Computation of Internal and External Flows, Wiley, Chichester, 1988.

Hoes, O., Luxemburg, W., Westhof, M., Van de Giesen, N., and Selker, J.: Identifying seepage in ditches and canals in polders in the Netherlands by distributed temperature sensing, Lowland Techn. Int., 11, 2009.

Holloway, P. E.: A criterion for thermal stratification in a wind-mixed system, Journal of Physical Oceanography, 10, 861–869, 1980.

Holzer, T. and Clark, M.: Sand boils without earthquakes, Geology, 21, 873–876, 1993.

Hooper, R., Christophersen, N., and Peters, N.: Modelling streamwater chemistry as a mixture of soilwater end-members - An application to the Panola Mountain catchment, Georgia, U.S.A., J. Hydrol., 116, 321–343, 1990.

Huppert, H. E. and Turner, J.: Double-diffusive convection, J. Fluid Mech., 106, 299–329, 1981.

Hurtig, E., Grosswig, S., Jobmann, M., Kühn, K., and Marschall, P.: Fibre-optic temperature measurements in shallow boreholes: experimental application for fluid logging, Geothermics, 23, 355–364, 1994.

Hut, R., Tyler, S., and Van Emmerik, T.: Proof of concept: temperature-sensing waders for environmental sciences, Geosci. Instrum. Method. Data Syst., 5, 45–51, doi:10.5194/gi-5-45-2016, 2016.

ICW: Hydrologie en Waterkwaliteit van Midden West-Nederland, in: Regionale Studies ICW 9, Wageningen, 1976.

Jansen, J., Stive, P., Van De Giesen, N., Tyler, S. W., Steele-Dunne, S., and Williamson, L.: Estimating soil heat flux using Distributed Temperature Sensing, IAHS-AISH Publication, 343, 140–144, 2011.

Janssen, L. and Warmoeskerken, M.: Transport phenomena data companion, Delftse Universitaire Pers, 1997.

Jensen, A. M., Neilson, B. T., McKee, M., and Chen, Y.: Thermal remote sensing with an autonomous unmanned aerial remote sensing platform for surface stream temperatures, in: Geoscience and Remote Sensing Symposium (IGARSS), 2012 IEEE International, 5049–5052, IEEE, 2012.

Jevons, W. S.: On the cirrous form of cloud, Philosophical Magazine Series 4, 14, 22–35, doi:10.1080/14786445708642347, 1857.

Jonsson, K., Johansson, H., and Wörman, A.: Hyporheic exchange of reactive and conservative solutes in streams–tracer methodology and model interpretation, J. Hydrol., 278, 153–171, doi:10.1016/S0022-1694(03)00140-9, 2003.

Jubran, B., Al-Abdali, H., Al-Hiddabi, S., Al-Hinai, H., and Zurigat, Y.: Numerical modelling of convective layers in solar ponds, Sol. Energy, 77, 339–345, doi:10.1016/j.solener.2004.04.004, 2004.

Kao, K. and Hockham, G.: Dielectric-fiber surface waveguides for optical frequencies, Proceedings of the IEE, 113, 1158–1163, 1966.

Katz, B. G., Catches, J. S., Bullen, T. D., and Michel, R. L.: Changes in the isotopic and chemical composition of ground water resulting from a recharge pulse from a sinking stream, J. Hydrol., 211, 178–207, doi:10.1016/S0022-1694(98)00236-4, 1998.

Keery, J., Binley, A., Crook, N., and Smith, J.: Temporal and spatial variability of groundwater-surface water fluxes: Development and application of an analytical method using temperature time series, J. Hydrol., 336, 1–16, doi:10.1016/j.jhydrol.2006.12.003, 2007.

Kelley, D. E., Fernando, H. J. S., Gargett, A. E., Tanny, J., and Özsoy, E.: The diffusive regime of double-diffusive convection, Progress In Oceanography, 56, 461–481, doi:10.1016/S0079-6611(03)00026-0, 2003.

Kim, K. S. and Chapra, S. C.: Temperature Model for Highly Transient Shallow Streams, Journal of Hydraulic Engineering, 123, 30–40, doi:10.1061/(ASCE)0733-9429(1997)123:1(30), 1997.

Kimura, S. and Smyth, W.: Direct numerical simulation of salt sheets and turbulence in a double-diffusive shear layer, Geophys. Res. Lett., 34, L21 610, doi:10.1029/2007GL031935, 2007.

Kimura, S., Smyth, W., and Kunze, E.: Turbulence in a sheared, salt-fingering-favorable environment: Anisotropy and effective diffusivities, Journal of Physical Oceanography, 41, 1144–1159, 2011.

Kolb, C.: Geologic control of sand boils along Mississippi River levees, Allen & Unwin, 1976.

Krause, S. and Blume, T.: Impact of seasonal variability and monitoring mode on the adequacy of fiber-optic distributed temperature sensing at aquifer-river interfaces, Water Resour. Res., 49(5), 2408–2423, doi:10.1002/wrcr.20232, 2013.

Kunze, E.: A review of oceanic salt-fingering theory, Progress in Oceanography, 56, 399–417, doi:10.1016/S0079-6611(03)00027-2, 2003.

LaFleur, R.: Geomorphic aspects of groundwater flow, Hydrogeology Journal, 7, 78–93, 1999.

Land, L. and Paull, C.: Thermal gradients as a tool for estimating groundwater advective rates in a coastal estuary: White Oak River, North Carolina, USA, J. Hydrol., 248, 198–215, 2001.

Langevin, C. D.: Modeling Axisymmetric Flow and Transport, Ground Water, 46, 579–590, doi:10.1111/j.1745-6584.2008.00445.x, 2008.

Launder, B. and Spalding, D.: The numerical computation of turbulent flows, Computer Methods in Applied Mechanics and Engineering, 3, 269–289, doi:10.1016/0045-7825(74)90029-2, 1974.

Lee, C.: Self-calibrating technique enables long-distance temperature sensing, Laser Focus World, 43, 101, 2007.

Lee, D.: A device for measuring seepage flux in lakes and estuaries, Limnology and Oceanography, 22, 140–147, 1977.

Lehrer, J.: A theoretical criterion of transition in the free motion of single bubbles and drops, AIChE J., 26, 170–172,doi:10.1002/aic.690260133, 1980.

Li, Y., Craven, J., Schweig, E., and Obermeier, S.: Sand boils induced by the 1993 Mississippi River flood: Could they one day be misinterpreted as earthquake-induced liquefaction?, Geology, 24, 171, 1996.

Liu, H. and Morris, C.: Integrating-float measurements in turbulent flows, Journal of the Hydraulics Division, 96, 565–572, 1970.

Loheide, S. P. and Gorelick, S. M.: Quantifying Stream-Aquifer Interactions through the Analysis of Remotely Sensed Thermographic Profiles and In Situ Temperature Histories, Environmental Science & Technology, 40, 3336–3341, doi:10.1021/es0522074, 2006.

Lowry, C., Walker, J., Hunt, R., and Anderson, M.: Identifying spatial/variability of groundwater discharge in a wetland stream using a distributed temperature sensor, Water Resour. Res., 43, 10408, 2007.

Menguc, M. and Viskanta, R.: Radiative transfer in axisymmetric, finite cylindrical enclosures, Journal of heat transfer, 108, 271–276, 1986.

Molemaker, M. and Dijkstra, H.: The formation and evolution of a diffusive interface, J. Fluid Mech., 331, 199–229, 1997.

Naranjo, R. C. and Turcotte, R.: A new temperature profiling probe for investigating groundwater-surface water interaction, Water Resour. Res., 51, 7790–7797, doi:10.1002/2015WR017574, 2015.

Neale, W., Hessel, D., and Terpstra, T.: Photogrammetric Measurement Error Associated with Lens Distortion, in: Accident Reconstruction, 2011, SAE International, doi:10.4271/2011-01-0286, 2011.

Neilson, B., Hatch, C., Ban, H., and Tyler, S.: Solar radiative heating of fiber-optic cables used to monitor temperatures in water, Water Resour. Res., 46, W08 540, 2010.

Noguchi, T. and Niino, H.: Multi-layered diffusive convection. Part 1. Spontaneous layer formation, J. Fluid Mech., 651, 443–464, 2010a.

Noguchi, T. and Niino, H.: Multi-layered diffusive convection. Part 2. Dynamics of layer evolution, J. Fluid Mech., 651, 465–481, 2010b.

Nowakowski, A. and Skarbek, W.: Lens radial distortion calibration using homography of central points, in: EUROCON, 2007. The International Conference on "Computer as a Tool", 340–343, IEEE, 2007.

O'Donnell Meininger, T. and Selker, J.: Bed conduction impact on fiber optic distributed temperature sensing water temperature measurements, Geosci. Instrum. Method. Data Syst., 4, 19, 2015.

Oude Essink, G. H. P.: Impact of sea level rise on groundwater flow regimes, Ph.D. thesis, Delft University of Technology, 1996.

Oude Essink, G., Van Baaren, E., and De Louw, P.: Effects of climate change on coastal groundwater systems: A modeling study in the Netherlands, Water Resour. Res., 46, 16, doi:10.1029/2009WR008719, 2010.

Ouni, M., Guizani, A., Lu, H., and Belghith, A.: Simulation of the control of a salt gradient solar pond in the south of Tunisia, Sol. Energy, 75, 95–101, 2003.

Pfister, L., McDonnell, J. J., Hissler, C., and Hoffmann, L.: Ground-based thermal imagery as a simple, practical tool for mapping saturated area connectivity and dynamics, Hydrol. Process., 24, 3123–3132, 2010.

Pomper, A. and Wesseling, J.: Chloride content of surface water as a result of geologic processes and groundwater flow in a coastal area in The Netherlands, in: Seminar on Selected Water Problems in Islands and Coastal Areas with Special Regard to Desalinization and Groundwater, Valetta, Malta, 1978.

Rabl, A. and Nielsen, C. E.: Solar ponds for space heating, Sol. Energy, 17, 1–12, doi:10.1016/0038-092X(75)90011-0, 1975.

Radko, T., Bulters, A., Flanagan, J., and Campin, J.-M.: Double-diffusive recipes. Part I: Large-scale dynamics of thermohaline staircases, J. Phys. Oceanogr., 44, 1269–1284, doi:10.1175/JPO-D-13-0155.1, 2014a.

Radko, T., Flanagan, J., Stellmach, S., and Timmermans, M.-L.: Double-diffusive recipes. Part II: Layer-merging events, J. Phys. Oceanogr., 44, 1285–1305, doi:10.1175/JPO-D-13-0156.1, 2014b.

Rayleigh, J.: On convection current in a horizontal layer in fluid, when the higher temperature is on the under side, Philosophical Magazine Series 6, 32, 529–546, 1916.

Rayleigh, L.: Investigation of the Character of the Equilibrium of an Incompressible Heavy Fluid of Variable Density, Proceedings of the London Mathematical Society, 14, 170–177, doi:10.1112/plms/s1-14.1.170, 1883.

Read, T., Bour, O., Bense, V., Le Borgne, T., Goderniaux, P., Klepikova, M., Hochreutener, R., Lavenant, N., and Boschero, V.: Characterizing groundwater flow and heat transport in fractured rock using fiber-optic distributed temperature sensing, Geophysical Research Letters, 40, 2055–2059, doi:10.1002/grl.50397, 2013.

Reilly, T. E. and Harbaugh, A. W.: Simulation of Cylindrical Flow to a Well Using the US Geological Survey Modular Finite-Difference Ground-Water Flow Model, Ground Water, 31, 489–494, 1993.

Renaud, J.-P., Cloke, H., and Weiler, M.: Comment on "An assessment of the tracer-based approach to quantifying groundwater contributions to streamflow" by J. P. Jones et al., Water Resour. Res., 43, 3, doi:10.1029/2006WR005157, 2007.

Rice, K. and Hornberger, G.: Comparison of hydrochemical tracers to estimate source contributions to peak flow in a small, forested, headwater catchment, Water Resour. Res., 34, 1755–1766, 1998.

Rosenberry, D. O., Sheibley, R. W., Cox, S. E., Simonds, F. W., and Naftz, D. L.: Temporal variability of exchange between groundwater and surface water based on high-frequency direct measurements of seepage at the sediment-water interface, Water Resour. Res., 49, 1–12, doi:10.1002/wrcr.20198, 2013.

Rossi, P., Dörfliger, N., Kennedy, K., Müller, I., and Aragno, M.: Bacteriophages as surface and ground water tracers, Hydrol. Earth Syst. Sci., 2, 101–110, 1998.

Ruddick, B.: A practical indicator of the stability of the water column to double-diffusive activity, Deep-Sea Res. Pt. I, 30, 1105–1107, 1983.

Ruddick, B. and Gargett, A. E.: Oceanic double-infusion: introduction, Progress In Oceanography, 56, 381–393, doi:10.1016/S0079-6611(03)00024-7, 2003.

Ruskowitz, J. A., Suárez, F., Tyler, S. W., and Childress, A. E.: Evaporation suppression and solar energy collection in a salt-gradient solar pond, Solar Energy, 99, 36–46, doi:10.1016/j.solener.2013.10.035, 2014.

Sargent, D.: Development of a viable method of stream flow measurement using the integrating float technique, Proceedings of the Institution of Civil Engineers (London), Part 2, 71, 1–15, 1981.

Sargent, D.: Rising air float technique for the measurement of stream discharge, Advances in hydrometry (Proceedings of the Exeter Symposium), IAHS Publ. no. 134 , 153–164, 1982a.

Sargent, D.: The accuracy of streamflow measurements using the rising air float technique., Proceedings Institution of Civil Engineers (London), Part 2, 73, 179–182, 1982b.

Sargent, D. and Davis, T.: Discussion: The development of a viable method of stream flow measurement using the integrating float technique, Proceedings of the Institution of Civil Engineers (London), Part 2, 71, 949–950, 1981.

Sayde, C., Thomas, C. K., Wagner, J., and Selker, J.: High-resolution wind speed measurements using actively heated fiber optics, Geophysical Research Letters, 42, 10 064–10 073, doi:10.1002/2015GL066729, 2015.

Schemel, L.: Simplified conversions between specific conductance and salinity units for use with data from monitoring stations, IEP Newsletter, 14, 17–18, 2001.

Schmid, M., Lorke, A., Wüest, A., Halbwachs, M., and Tanyileke, G.: Development and sensitivity analysis of a model for assessing stratification and safety of Lake Nyos during artificial degassing, Ocean Dynamics, 53, 288–301, 2003.

Schmid, M., Lorke, A., Dinkel, C., Tanyileke, G., and Wüest, A.: Double-diffusive convection in Lake Nyos, Cameroon, Deep-Sea Res. Pt. I, 51, 1097–1111, doi:10.1016/j.dsr.2004.02.010, 2004.

Schubert, F., Peiffer, A., Köhler, B., and Sanderson, T.: The elastodynamic finite integration technique for waves in cylindrical geometries, The Journal of the Acoustical Society of America, 104, 2604–2614, 1998.

Sebok, E., Duque, C., Kazmierczak, J., Engesgaard, P., Nilsson, B., Karan, S., and Frandsen, M.: High-resolution distributed temperature sensing to detect seasonal groundwater discharge into Lake Væng, Denmark, Water Resour. Res., 49, 5355–5368, doi:10.1002/wrcr.20436, 2013.

Sebok, E., Duque, C., Engesgaard, P., and Boegh, E.: Application of Distributed Temperature Sensing for coupled mapping of sedimentation processes and spatio-temporal variability of groundwater discharge in soft-bedded streams, Hydrol. Process., 29, 3408–3422, doi:10.1002/hyp.10455, 2015.

Selker, J., Thévenaz, L., Huwald, H., Mallet, A., Luxemburg, W., Van de Giesen, N., Stejskal, M., Zeman, J., Westhoff, M., and Parlange, M.: Distributed fiber optic temperature sensing for hydrologic systems, Water Resour. Res, 42, W12 202, 2006a.

Selker, J., Van de Giesen, N., Westhoff, M., Luxemburg, W., and Parlange, M.: Fiber optics opens window on stream dynamics, Geophys. Res. Lett, 33, 24 401, 2006b.

Sellmeijer, J. and Koenders, M.: A mathematical model for piping, Applied mathematical modelling, 15, 646–651, 1991.

Shafer, J., Brantley, D., and Waddell, M.: Variable-density flow and transport simulation of wellbore brine displacement, Ground Water, 48, 122–130, doi:10.1111/j.1745-6584.2009.00594.x, 2010.

Sharqawy, M. H., Lienhard, J. H., and Zubair, S. M.: Thermophysical properties of seawater: a review of existing correlations and data, Desalination and Water Treatment, 16, 354–380, 2010.

Shaw, E.: Hydrology in practice, Routledge, 1994.

Shima, E., Matsuda, T., Takeda, H., and Sawada, K.: Hydrodynamic calculations of axisymmetric accretion flow, Monthly Notices of the Royal Astronomical Society, 217, 367–386, doi:10.1093/mnras/217.2.367, 1985.

Silliman, S. E. and Booth, D. F.: Analysis of time-series measurements of sediment temperature for identification of gaining vs. losing portions of Juday Creek, Indiana, J. Hydrol., 146, 131–148, doi:10.1016/0022-1694(93)90273-C, 1993.

Slichter, C.: Field measurements of the rate of movement of underground waters, U.S. Geol. Survey Water-supply paper, 140, 1905.

Smolen, J. and van der Spek, A.: Distributed Temperature Sensing, 2003.

Sommer, T., Carpenter, J. R., and Wüest, A.: Double-diffusive interfaces in Lake Kivu reproduced by direct numerical simulations, Geophys. Res. Lett., 41, 5114–5121, doi:10.1002/2014GL060716, 2014.

Souto-Maior, J.: Applications of thermal remote sensing to detailed ground water studies, Proceedings of the Symposium on Remote sensing and water resources management (June 11-14, 1973; Ontario; Canada), 284–298, 1973.

Stallman, R.: Computation of ground-water velocity from temperature data, USGS Water Supply Paper 1544-H, 36–46, 1963.

Steele-Dunne, S., Rutten, M., Krzeminska, D., Hausner, M., Tyler, S., Selker, J., Bogaard, T., and Van de Giesen, N.: Feasibility of soil moisture estimation using passive distributed temperature sensing, Water Resour. Res., 46, 12, 2010.

Stein, G.: Lens distortion calibration using point correspondences, Proceedings of the IEEE Computer Society Conference on Computer Vision and Pattern Recognition (17–19 June 1997; Conference Code: 46787), 602–608, 1997.

Stern, M. E.: The "Salt-Fountain" and Thermohaline Convection, Tellus, 12, 172–175, doi:10.1111/j.2153-3490.1960.tb01295.x, 1960.

Stern, M. E.: Lateral mixing of water masses, Deep-Sea Res., 14, 747–753, doi:10.1016/S0011-7471(67)80011-1, 1967.

Stern, M. E. and Turner, J. S.: Salt fingers and convecting layers, Deep-Sea Res., 16, 497–511, doi:10.1016/0011-7471(69)90038-2, 1969.

Stommel, H. and Fedorov, K.: Small scale structure in temperature and salinity near Timor and Mindanao, Tellus A, 19, 1967.

Stommel, H., Arons, A., and Blanchard, D.: An oceanographical curiosity: the perpetual salt fountain, Deep-Sea Res., 3, 152–153, 1956.

Stonestrom, D. and Constantz, J.: Heat as a tool for studying the movement of ground water near streams, US Geological Survey Denver, CO, 2003.

Su, L., Li, N., Zhang, X., Sun, Y., and Qian, J.: Heat transfer and cooling characteristics of concrete ceiling radiant cooling panel, Applied Thermal Engineering, 84, 170–179, doi:10.1016/j.applthermaleng.2015.03.045, 2015.

Suh, K. and Lee, C.: Auto-correction method for differential attenuation in a fiber-optic distributed-temperature sensor, Optics letters, 33, 1845–1847, 2008.

Suh, K., Lee, C., Sanders, M., and Kalar, K.: Active plug & play distributed Raman temperature sensing, Proceedings of the Conference of 19th International Conference on Optical Fibre Sensors, SPIE vol. 7004 (15–18 April 2008; Perth, WA; Conference Code: 72327), doi:10.1117/12.791156, 2008.

Suárez, F., Childress, A., and Tyler, S.: Temperature evolution of an experimental salt-gradient solar pond, Journal of Water and Climate Change, 1, 246–250, 2010a.

Suárez, F., Tyler, S., and Childress, A.: A fully coupled, transient double-diffusive convective model for salt-gradient solar ponds, Int. J. Heat Mass Tran., 53, 1718–1730, doi:10.1016/j.ijheatmasstransfer.2010.01.017, 2010b.

Suárez, F., Aravena, J., Hausner, M., Childress, A., and Tyler, S.: Assessment of a vertical high-resolution distributed-temperature-sensing system in a shallow thermohaline environment, Hydrol. Earth Syst. Sci., 15, 1081–1093, doi:10.5194/hess-15-1081-2011, 2011.

Suárez, F., Ruskowitz, J. A., Childress, A. E., and Tyler, S. W.: Understanding the expected performance of large-scale solar ponds from laboratory-scale observations and numerical modeling, Applied Energy, 117, 1–10, doi:10.1016/j.apenergy.2013.12.005, 2014.

Swaminathan, R. and Nayar, S.: Nonmetric calibration of wide-angle lenses and polycameras, IEEE Transactions on Pattern Analysis and Machine Intelligence, 22, 1172–1178, doi:10.1109/34.879797, 2000.

SWASH source code (Version 1.20), accessed on: 30 May 2016, http://swash.sourceforge.net/, 2010.

Tait, R. and Howe, M.: Some observations of thermo-haline stratification in the deep ocean, Deep-Sea Res., 15, 275–280, doi:10.1016/0011-7471(68)90005-3, 1968.

Theis, C.: The relation between the lowering of the piezometric surface and the rate and duration of discharge of a well using groundwater storage, Trans. Amer. Geophys. Union, 16, 519–524, 1935.

Thomann, R. V. and Mueller, J. A.: Principles of surface water quality modeling and control, Harper & Row, Publishers, 1987.

Thomas, C. K., Kennedy, A. M., Selker, J. S., Moretti, A., Schroth, M. H., Smoot, A. R., Tufillaro, N. B., and Zeeman, M. J.: High-resolution fibre-optic temperature sensing: A new tool to study the two-dimensional structure of atmospheric surface-layer flow, Boundary-layer meteorology, 142, 177–192, 2012.

Toop, C., Webster, P., and Hawnt, R.: Improved guidelines for the use of the rising air float technique for river gauging, Journal of the Chartered Institution of Water and Environmental Management, 11, 61–66, 1997.

Traxler, A., Stellmach, S., Garaud, P., Radko, T., and Brummeln, N.: Dynamics of fingering convection. Part 1 Small-scale fluxes and large-scale instabilities, J. Fluid Mech., 677, 530–553, doi:10.1017/jfm.2011.98, 2011.

Tsai, R. Y.: Versatile Camera Calibration Technique for High-Accuracy 3D Machine Vision Metrology Using Off-the-Shelf TV Cameras and Lenses, IEEE journal of robotics and automation, RA-3, 323–344, 1987.

Tsilingiris, P. T.: An accurate upper estimate for the transmission of solar radiation in salt gradient ponds, Sol. Energy, 40, 41–48, 1988.

Turner, J.: The coupled turbulent transports of salt and and heat across a sharp density interface, Int. J. Heat Mass Tran., 8, 759–760, IN3–IN4, 761–767, doi:10.1016/0017-9310(65)90022-0, 1965.

Turner, J.: Salt fingers across a density interface, Deep-Sea Res., 14, 599–608, IN21, 609–611, doi:10.1016/0011-7471(67)90066-6, 1967.

Turner, J. S.: The behaviour of a stable salinity gradient heated from below, J. Fluid Mech., 33, 183–200, doi:10.1017/S0022112068002442, 1968.

Turner, J. S.: Buoyancy effects in fluids, Cambridge University Press, 1973.

Tyler, S., Selker, J., Hausner, M., Hatch, C., Torgersen, T., Thodal, C., and Schladow, S.: Environmental temperature sensing using Raman spectra DTS fiber-optic methods, Water Resour. Res, 45, W00 D23, 2009.

Unesco: Tenth report of the joint panel on oceanographic tables and standards, UNESCO Tech. Paper in Marine Science, 36, 25, 1981.

Van de Giesen, N., Steele-Dunne, S., Jansen, J., Hoes, O., Hausner, M., Tyler, S., and Selker, J.: Double-Ended Calibration of Fiber-Optic Raman Spectra Distributed Temperature Sensing Data, Sensors, 12, 5471–5485, 2012.

Van de Ven, G.: Man-made lowlands: history of water management and land re-clmation in the Netherlands, Uitgeverij Matrijs, 1993.

Van der Most, H.: Towards Sustainable Development of Deltas, Estuaries and Coastal Zones: Description of Eight Selected Deltas; Trends and Responses, Deltares, 2009.

Van Emmerik, T., Rimmer, A., Lechinsky, Y., Wenker, K., Nussboim, S., and Van de Giesen, N.: Measuring heat balance residual at lake surface using Distributed Temperature Sensing, Limnol. Oceanogr.: Methods, 11, 79–90, 2013.

Van Rees Vellinga, E., Toussaint, C., and Wit, K.: Water quality and hydrology in a coastal region of the Netherlands, J. Hydrol., 50, 105–127, 1981.

Vandenbohede, A., De Louw, P., and Doornenbal, P.: Characterizing preferential groundwater discharge through boils using temperature, J. Hydrol., 510, 372–384, doi:10.1016/j.jhydrol.2014.01.006, 2014.

Vega, L. A.: Ocean Thermal Energy Conversion Primer, Marine Technology Society Journal, 36, 25–35, doi:10.4031/002533202787908626, 2002.

Vercauteren, N., Huwald, H., Bou-Zeid, E., Selker, J. S., Lemmin, U., Parlange, M. B., and Lunati, I.: Evolution of superficial lake water temperature profile under diurnal radiative forcing, Water Resour. Res., 47, doi:10.1029/2011WR010529, 2011.

Viol, V. and Semenov, V.: Experiments in measuring discharges in canals by the photo-integration method, Soviet Hydrol. Selected Pap, 2, 198–199, 1964.

Vogt, T., Schneider, P., Hahn-Woernle, L., and Cirpka, O.: Estimation of seepage rates in a losing stream by means of fiber-optic high-resolution vertical temperature profiling, J. Hydrol., 380, 11, 2010.

Vogt, T., Schirmer, M., and Cirpka, O. A.: Investigating riparian groundwater flow close to a losing river using diurnal temperature oscillations at high vertical resolution, Hydrol. Earth Syst. Sci., 16, 473–487, doi:10.5194/hess-16-473-2012, 2012.

Walton, N.: Electrical conductivity and total dissolved solids - What is their precise relationship?, Desalination, 72, 275–292, 1989.

Washburn, E. W. and West, C. J.: International Critical Tables of Numerical Data, Physics, Chemistry and Technology: Vol. 1-7, McGraw-Hill, 1933.

Weinberger, H.: The physics of the solar pond, Sol. Energy, 8, 45–56, doi:10.1016/0038-092X(64)90046-5, 1964.

Wesselingh, J.: The velocity of particles, drops and bubbles, Chemical Engineering and Processing: Process Intensification, 21, 9–14, doi:10.1016/0255-2701(87)80002-8, 1987.

Westhoff, M., Savenije, H., Luxemburg, W., Stelling, G., Van de Giesen, N., Selker, J., Pfister, L., and Uhlenbrook, S.: A distributed stream temperature model using high resolution temperature observations, Hydrol. Earth Syst. Sci., 11, 1469–1480, 2007.

Westhoff, M., Bogaard, T., and Savenije, H.: Quantifying the effect of in-stream rock clasts on the retardation of heat along a stream, Adv. Water Resour., 33, 1417–1425, doi:10.1016/j.advwatres.2010.02.006, 2010.

Westhoff, M., Gooseff, M., Bogaard, T., and Savenije, H.: Quantifying hyporheic exchange at high spatial resolution using natural temperature variations along a first-order stream, Water Resour. Res., 47, 2011.

Wolberg, G.: Digital image warping, IEEE Computer Society Press Monograph, IEEE Computer Society Press, Los Alamitos, CA, 1990.

Wright, D. G.: An Equation of State for Use in Ocean Models: Eckart's Formula Revisited, J. Atmos. Oceanic Technol., 14, 735–740, doi:10.1175/1520-0426(1997)014<0735:AEOSFU>2.0.CO;2, 1997.

Yannopoulos, P., Demetracopoulos, A., and Hadjitheodorou, C.: Quick method for open-channel discharge measurements using air bubbles, Journal of Hydraulic Engineering, 134, 843–846, doi:10.1061/(ASCE)0733-9429(2008)134:6(843), 2008.

Yoshida, J. and Nagashima, H.: Numerical experiments on salt-finger convection, Progress In Oceanography, 56, 435–459, doi:10.1016/S0079-6611(03)00032-6, 2003.

Zijlema, M. and Stelling, G.: Efficient computation of surf zone waves using the nonlinear shallow water equations with non-hydrostatic pressure, Coastal Engineering, 55, 780–790, 2008.

Zijlema, M. and Stelling, G. S.: Further experiences with computing non-hydrostatic free-surface flows involving water waves, Int. J. Numer. Meth. Fl., 48, 169–197, doi:10.1002/fld.821, 2005.

Zijlema, M., Stelling, G., and Smit, P.: SWASH: An operational public domain code for simulating wave fields and rapidly varied flows in coastal waters, Coastal Engineering, 58, 992–1012, doi:10.1016/j.coastaleng.2011.05.015, 2011.

Zwolsman, J. and Van Bokhoven, A.: Impact of summer droughts on water quality of the Rhine River - a preview of climate change?, Water Science and Technology, 56, 45–55, doi:10.2166/wst.2007.535, 2007.

Curriculum Vitæ

Personal data

Family name: Hilgersom
First names: Koen Peter
Date of birth: 6 January 1985
Place of birth: Alkmaar, the Netherlands
Nationality: Dutch

Education

2010–2016   PhD Civil Engineering
Delft University of Technology, Delft

Thesis: Measuring & modelling salt and heat transport in low-land drainage canals
Promotor: Prof. dr. ir. N.C. van de Giesen
Copromotor: Dr. ir. M. Zijlema

2007–2010   MSc Civil Engineering (Master track Watermanagement)
Delft University of Technology, Delft

Track: Water management, specialization Hydrology
Activities: Internship at HKV Consultants, Lelystad, the Netherlands
Board member at student society 'Dispuut Watermanagement' (2008–2009)
Organisation of the symposium *'Water Trade, a Virtual Reality?!'* (2008)
Preparation of the research proposal for the project *'A flexible approach to catchment modelling and flood protection'* (AFR-FNR, reference number 1383201)
Thesis: Closing the water balance for lake Lauwersmeer

2003–2007   BSc Civil Engineering
Delft University of Technology, Delft

Thesis: Salt dilution gauging ('De zoutverdunningsmethode')

1997–2003   Secondary School (VWO)
Christelijk Gymnasium, Utrecht

Track: Nature & Technology

Experience

2015	Researcher
	Water Resources Section
	Delft University of Technology, Delft, the Netherlands

            Activities: Project exploration and preparation for Horizon2020 project *WaterInnEU*
Data collection, analysis, and formatting
Database construction

2010–2016	PhD researcher
	Water Resources Section
	Delft University of Technology, Delft, the Netherlands

            Activities: Development and field testing of a novel three-dimensional distributed temperature sensing approach
Derivation and implementation of numerical solutions for an axisymmetrical non-hydrostatic transport model
Modernization of the rising bubble technique for river discharge measurement with image processing techniques
Supervisor during hydrological fieldwork courses
Supervisor of 8 BSc theses
Reviewer for the journals *HESS* and *WRR*
Content management and reconstruction of the department website

2013	Visiting scientist (1.5 month)
	Department of Biological & Ecological Engineering
	Oregon State University (OSU), Corvallis (OR), USA

2013	Visiting scientist (1.5 month)
	Department of Geological Sciences & Engineering
	University of Nevada Reno (UNR), Reno (NV), USA

List of Publications

1. **K.P. Hilgersom** and W.M.J. Luxemburg, *Technical note: How image processing facilitates the rising bubble technique for discharge measurement*, Hydrol. Earth Syst. Sci. **16(2)**, 345–356, doi:10.5194/hess-16-345-2012, 2012.

2. **K.P. Hilgersom**, T.H.M. van Emmerik, A. Solcerova, W.R. Berghuijs, J.S. Selker, and N.C. van de Giesen, *Practical considerations for enhanced-resolution coil-wrapped distributed temperature sensing*, Geosci. Instrum. Method. Data Syst. **5(1)**, 151–162, doi:10.5194/gi-5-151-2016, 2016.

3. **K.P. Hilgersom**, N.C. van de Giesen, P.G.B. de Louw, and M. Zijlema, *Three-dimensional dense distributed temperature sensing for measuring layered thermohaline systems*, Water Resour. Res. **52(8)**, 6656–6670, doi:10.1002/2016WR019119, 2016.

4. **K.P. Hilgersom**, M. Zijlema, and N.C. van de Giesen, *An axisymmetric non-hydrostatic model for double-diffusive water systems*, Geosci. Model Dev. Discuss., doi:10.5194/gmd-2016-176, 2016 *(under review)*.

5. **K.P. Hilgersom**, F. Suárez, M. Zijlema, M.B. Hausner, S.W. Tyler, and N.C. van de Giesen, *Heat and salt transport near the sloping edge of a solar pond: a two-dimensional numerical study*, Int. J. Heat Mass Tran., 2016 *(under review)*.

Published data sets

1. **K.P. Hilgersom**, W.R. Berghuijs, A. Solcerova, and T.H.M. van Emmerik, *Thermal energy balance model of a fiber-optic cable; data from a shallow urban pond, Delft*, doi:10.4121/uuid:a946eca5-0901-4a09-a95a-0c028a6b1853, TU Delft, 2015.

2. **K.P. Hilgersom**, N.C. van de Giesen, P.G.B de Louw, and M. Zijlema, *3D Dense DTS: temperature data from waterbodies subject to thermohaline stratification - Laboratory measurements and field campaigns in the Noordplas Polder and at Kortenhoef*, doi:10.4121/uuid:da1d236b-7d0a-4c67-9136-bf913a7aa1b2, TU Delft, 2016.

3. **K.P. Hilgersom**, M. Zijlema, and N.C. van de Giesen, *An axisymmetric hydrodynamical model: model code and data*, doi:10.4121/uuid:c0dce972-5a04-476f-8f3f-4ac34f40da1b, TU Delft, 2016.

4. **K.P. Hilgersom**, F. Suárez, M. Zijlema, M.B. Hausner, S.W. Tyler, and N.C. van de Giesen, *A free-surface solar pond model with a sloping edge: model code and data*, doi:10.4121/uuid:87829ef5-be45-40e7-a0a7-b4c514633e26, TU Delft, 2016.

River deltas have always been an attractive area to live due to the abundance of food and water and the opportunities for economic activities. On the other hand, direct consumption, crop growth, industry, and energy production put a high demand on the fresh water resources. These resources are further threatened by saline groundwater seepage. In the future, sea-level rise and land subsidence are expected to increase salt intrusion.

Local groundwater seepage sources ("boils") are often responsible for a significant part of the salinization in deep polders. Here, boils often discharge into the polder drainage canals. Conventionally, such forms of groundwater - surface water interaction are measured by placing probes in the soil. This research aims to quantify the boil seepage flux from a surface water perspective.

Using fiber-optic distributed temperature sensing, high-resolution three-dimensional temperature profiles are collected of the surface water above boils. We intend to infer the boil seepage flux from these temperature profiles by means of a salt and heat transport model. It is concluded that this model inversion procedure is still too challenging in water bodies where sharp salt and heat gradients control the flow processes.